International Journal of Solids and Structures 134 (2018) 43–69

Contents lists available at ScienceDirect

International Journal of Solids and Structures

journal homepage: www.elsevier.com/locate/ijsolstr

A reduced micromorphic single crystal plasticity model at finite deformations. Application to strain localization and void growth in ductile metals

Chao Ling[a,b], Samuel Forest[b,*], Jacques Besson[b], Benoît Tanguy[a], Felix Latourte[c]

[a] DEN–Service d'Etudes des Matériaux Irradiés, CEA, Université Paris–Saclay, F-91191 Gif-sur-Yvette cedex, France
[b] MINES ParisTech, PSL Research University, MAT – Centre des matériaux, CNRS UMR 7633, BP 87 91003 Evry, France
[c] EDF R&D, MMC, Site des Renardières, F-77818 Moret-sur-Loing cedex, France

ARTICLE INFO

Article history:
Received 11 June 2017
Revised 8 October 2017
Available online 18 October 2017

Keywords:
Micromorphic model
Strain gradient plasticity
Ductile single crystal
Strain localization
Slip band
Kink band
Regularization
Void growth
Void coalescence
Size effect

ABSTRACT

A micromorphic single crystal plasticity model is formulated at finite deformations as an extension of Mandel's classical theory based on a multiplicative decomposition of the deformation gradient. It involves a single *microslip* degree of freedom in addition to the usual displacement components. Two main variants of the constitutive equations are proposed. The first one relies on a Lagrangian microslip gradient and leads to a Laplace term in the isotropic hardening law. In contrast, the second formulation, based on a generalized strain measure defined with respect to the intermediate configuration, is shown to induce both isotropic and kinematic enhanced hardening. The first formulation is implemented in a 3D finite element code. The model is applied first to strain localization phenomena in a single crystal in tension undergoing single slip. The regularization power of the model is illustrated by mesh-independent simulations of the competition between kink and slip bands. The model is then used to investigate void growth and coalescence in FCC single crystals. Cylindrical and spherical voids are considered successively. The simulations show, for the first time in the case of spherical voids embedded in a single crystal matrix, that smaller voids grow slower than bigger ones, and that the onset of void coalescence is delayed for smaller voids. These results are related to the fact that the field of plastic slip is found to be more diffuse around smaller voids.

1. Introduction

The intrinsically heterogeneous nature of plastic slip in metals results in a non-homogeneous deformation of single crystals. With increasing straining, the deformation of single crystals is usually accompanied with diffused necking or/and localized shearing (Peirce et al., 1982a), which has been observed in experimental studies such as in (Simoto et al., 1965; Chang and Asaro, 1981). Localized shear banding in single crystals has been analyzed by means of bifurcation analysis of the classical crystal plasticity constitutive equations (see, e.g., Asaro and Rice, 1977; Forest and Cailletaud, 1995; Forest, 1998) and finite element simulations (see, e.g., Peirce et al., 1982a; Forest, 1998). However, the post-localization behavior and the size–dependence of localization modes require enhanced crystal plasticity models accounting for a more accurate description of dislocation distribution and motion. A complete description relies on an infinite set of correlation functions according to Kröner (1969). A first enhancement is the introduction of Kröner's dislocation density tensor into the constitutive framework in addition to the usual scalar dislocation density variables. There exists a direct connection between the dislocation density tensor and the concept of geometrically necessary dislocations introduced by Ashby (1971). In addition, the finite element simulation of shear bands with classical single crystal plasticity theory leads to a spurious mesh-dependence (Forest and Cailletaud, 1995). Hence, enhanced theories are needed for better simulating strain localization phenomena in single crystals. For example, Forest (1998) showed that Cosserat single crystal plasticity models accounting for lattice curvature effects can separate slip and kink banding modes which are identically predicted by the classical theory, see (Forest et al., 1997; 2000; Mayeur et al., 2011; Mayeur and McDowell, 2011; 2015) for the presentation of Cosserat, or equivalently, micropolar crystal plasticity theory. Slip bands correspond to slip localization along a crystallographic slip plane whereas kink bands are othogonal to the slip direction. Moreover, the kink bands pre-

* Corresponding author.
E-mail addresses: samuel.forest@ensmp.fr, samuel.forest@mat.ensmp.fr (S. Forest).

https://doi.org/10.1016/j.ijsolstr.2017.10.013
0020-7683/

dicted by the Cosserat theory are of finite width but the slip band is not affected compared with the classical theory.

On the other hand, the presence of geometrically necessary dislocations induced by strong strain gradients gives rise to size effects in the form of higher yield stress and hardening in bending, torsion or confined plasticity experiments as discussed and modeled by Fleck and Hutchinson (1997). This is the realm of strain gradient crystal plasticity initiated by Aifantis (1987), revisited and further developed by Gurtin (2000; 2002); Bardella (2007); Mesarovic et al. (2010); Wulfinghoff et al. (2015). Some theories directly involve the dislocation density tensor which characterizes the incompatibility of plastic deformation (e.g., Gurtin, 2002; Cordero et al., 2010). More refined theories introduce individual densities of geometrically necessary dislocations (Evers et al., 2004; Bayley et al., 2006; Ertürk et al., 2009; Bardella et al., 2013). Micromorphic crystal plasticity in the form of the *microcurl* model proposed by Cordero et al. (2010) represents an extension of Cosserat crystal plasticity and contains strain gradient crystal plasticity as a limit case. It can be seen as a relaxed strain gradient crystal plasticity model or as a more general constitutive model, as demonstrated for precipitate and grain size effects in (Cordero et al., 2010; 2012).

Finite deformation formulations of gradient and micromorphic crystal plasticity are available in (Borg et al., 2008; Gurtin, 2008; 2010; Aslan et al., 2011). They are necessary for the study of size effects in the fracture of crystalline solids. Size effects on the void growth of single crystals were predicted in a pionneering work by Shu (1998) and more recently in a series of papers (Niordson, 2008; Borg and Kysar, 2007; Borg et al., 2008; Hussein et al., 2008; Niordson and Kysar, 2014). As a result, voids of varying size can play distinct roles during ductile fracture process and affect the final fracture toughness.

The numerical implementation of such generalized crystal plasticity in finite element codes is not an easy task for several reasons. The available finite element formulations are generally restricted to small strain formulation or finite strain formulation with planar double slip, such as the works of (Wulfinghoff and Böhlke, 2012; Gurtin et al., 2007; Evers et al., 2004; Ekh et al., 2007). In addition, Miehe (2014) recently showed an efficient implementation of gradient single crystal plasticity at finite strains based on variational principles. The computational cost of the model highly depends on the complexity of the model. Models based on individual GND densities require at least as many additional nodal degrees of freedom as slip systems, which becomes untractable for crystallographic systems involving 24 to 48 such slip systems. In contrast, the complexity of theories based on the total dislocation density tensor is associated to a fixed number of additional degrees of freedom, up to 9 in Eringen's micromorphic original theory. The micromorphic approach is often used to implement strain gradient plasticity models after introducing proper penalty terms or Lagrange multipliers (Forest, 2009).

What is currently missing is a generalized crystal plasticity model, sufficiently simple and computationnally efficient to be applicable to 3D fracture mechanics problems in single crystals. Simplified generalized plasticity models were recently proposed, based on the micromorphic approach presented in (Forest, 2009) at small strains and (Forest, 2016) at finite deformations, that rely on the introduction of one single additional degree of freedom. Aslan and Forest (2009); Aslan et al. (2011) introduced a *microdamage* variable cumulating the damage on all the slip planes. Wulfinghoff and Böhlke (2012; 2013); Wulfinghoff et al. (2013) proposed a simplified micromorphic crystal plasticity model involving a single *microslip* variable and its gradient into the constitutive equations, instead of the full dislocation density tensor. They showed that several main features of size–dependent plasticity were accounted for in spite of the reduced description of higher order kinematics. The *microslip* variable is constitutively related to the accumulated slip on all slip systems. Its gradient is introduced in the free energy density function.

The objectives of the present work are therefore to formulate, implement and apply a reduced finite strain size–dependent crystal plasticity model in order to simulate localization and damage processes in single crystals. In contrast to most existing formulations it must be amenable to 3D computations required for the simulations of spherical pores in single crystal matrix, single crystal fracture specimens (CT, SENT samples etc.) but also cracks in polycrystalline aggregates. The model presented in this work essentially is the extension to finite deformations of Wulfinghof and Böhlke's micromorphic single crystal plasticity (Wulfinghoff and Böhlke, 2012). It includes several variants of the constitutive equations depending on whether the constitutive microslip gradient variables are introduced in the Lagrangian, Eulerian or intermediate configurations as defined in Mandel's multiplicative theory of finite deformation crystal plasticity.

Two applications are presented in this work dealing with kink/slip banding and cavity growth leading to ductile damage in single crystals. Mesh–independent finite element simulations of the competition between slip and kink banding in a tensile specimen are provided for the first time. The predictions of the model regarding void growth and coalescence are compared, in the 2D case, to recent results from the literature based on more complex strain gradient plasticity theories. Novel results are finally provided in the 3D case for the growth of a spherical cavity in a periodic unit cell.

The outline of the paper is as follows. The thermodynamically consistent constitutive equations of the proposed reduced micromorphic crystal plasticity model, and their variants, are derived in sections 2 and 3. Section 4 is dedicated to a brief description of the numerical implementation in the finite element code `Zset` (Besson and Foerch, 1997; Z-set package, 2013). The approach is then successively applied to strain localization phenomena in a single crystal (Section 5) and to growth and coalescence of cylindrical and spherical voids in a single crystal matrix (Section 6).

According to the notations used throughout this work, first, second and fourth rank tensors are written $\underline{\boldsymbol{a}}$, $\underline{\underline{\mathbf{a}}}$ and $\underline{\underline{\underline{\underline{\boldsymbol{a}}}}}$, respectively. Gradient and divergence operators w.r.t. Lagrangian (resp. Eulerian) coordinates are called Grad (resp. grad) and Div (resp. div). Note that the components of the gradient of a second order tensor $\underline{\underline{\mathbf{A}}}$ are taken as $A_{ij,k}$ in a Cartesian orthonormal coordinate system. Its divergence is the trace of the gradient with respect to the last two indices. The scalar product of two vectors is $\underline{\boldsymbol{a}} \cdot \underline{\boldsymbol{b}} = a_i b_i$. The double contraction of two generally non symmetric second order tensors is $\underline{\underline{\mathbf{A}}} : \underline{\underline{\mathbf{B}}} = A_{ij}B_{ij}$. The inverse of the transpose of $\underline{\underline{\mathbf{A}}}$ is $\underline{\underline{\mathbf{A}}}^{-T}$.

2. Reduced micromorphic single crystal plasticity model at finite deformation

Compared to Eringen's original finite deformation micromorphic theory based on the introduction of a generally non–symmetric second order tensor of microdeformation (Eringen, 1999), the reduced micromorphic model presented below relies on a single additional degree of freedom of the material point.

2.1. Kinematics of a micromorphic single crystal

The crystalline body occupies the region $\mathbf{B_0}$ in a fixed reference configuration. Each point $\underline{\boldsymbol{X}}$ belonging to $\mathbf{B_0}$ is referred to as a material point. Following the micromorphic approach (Forest, 2009; Aslan et al., 2011), two types of degrees of freedom (DOF) are attributed to each material point, namely the displacement vector,

$\underline{\boldsymbol{u}}(\underline{\boldsymbol{X}}, t)$, and an additional strain–like DOF, $\gamma_\chi(\underline{\boldsymbol{X}}, t)$. The set of DOFs is:

$$\text{DOF} = \{\underline{\boldsymbol{u}}, \gamma_\chi\}. \tag{1}$$

In the present work, the additional DOF, γ_χ, is a scalar variable called *microslip*.

At time t, the deformed body occupies the region $\mathbf{B}$ in space, called the current configuration. The Lagrangian gradients of the degrees of freedom are

$$\underline{\underline{\boldsymbol{H}}}(\underline{\boldsymbol{x}}, t) = \frac{\partial \underline{\boldsymbol{u}}}{\partial \underline{\boldsymbol{X}}} = \text{Grad}\,\underline{\boldsymbol{u}}, \quad \underline{\boldsymbol{K}}(\underline{\boldsymbol{x}}, t) = \frac{\partial \gamma_\chi}{\partial \underline{\boldsymbol{X}}} = \text{Grad}\,\gamma_\chi, \tag{2}$$

where $\underline{\underline{\boldsymbol{H}}}$ is the displacement gradient which is related to the deformation gradient $\underline{\underline{\boldsymbol{F}}}$ by $\underline{\underline{\boldsymbol{F}}} = \underline{\underline{\boldsymbol{1}}} + \underline{\underline{\boldsymbol{H}}}$, and $\underline{\boldsymbol{K}}$ is referred to as the Lagrangian microslip gradient vector. Besides, the Eulerian gradient of γ_χ will also be used in the following:

$$\underline{\boldsymbol{k}} = \frac{\partial \gamma_\chi}{\partial \underline{\boldsymbol{x}}} = \text{grad}\,\gamma_\chi = \underline{\boldsymbol{K}} \cdot \underline{\underline{\boldsymbol{F}}}^{-1} = \underline{\underline{\boldsymbol{F}}}^{-T} \cdot \underline{\boldsymbol{K}} \tag{3}$$

where $\underline{\boldsymbol{x}}$ is the current position of material point $\underline{\boldsymbol{X}}$ at time t.

Taking the time derivative of the field of DOFs provides the generalized velocities $\{\dot{\underline{\boldsymbol{u}}}, \dot{\gamma}_\chi\}$:

$$\dot{\underline{\boldsymbol{u}}} = \frac{\partial \underline{\boldsymbol{u}}(\underline{\boldsymbol{X}}, t)}{\partial t}, \quad \dot{\gamma}_\chi = \frac{\partial \gamma_\chi(\underline{\boldsymbol{X}}, t)}{\partial t} \tag{4}$$

The Eulerian gradients of the generalized velocities are computed as

$$\text{grad}\,\dot{\underline{\boldsymbol{u}}} = (\text{Grad}\,\dot{\underline{\boldsymbol{u}}}) \cdot \underline{\underline{\boldsymbol{F}}}^{-1} = \dot{\overline{\text{Grad}\,\underline{\boldsymbol{u}}}} \cdot \underline{\underline{\boldsymbol{F}}}^{-1} = \dot{\underline{\underline{\boldsymbol{F}}}} \cdot \underline{\underline{\boldsymbol{F}}}^{-1}, \tag{5}$$

$$\text{grad}\,\dot{\gamma}_\chi = \left(\text{Grad}\,\dot{\gamma}_\chi\right) \cdot \underline{\underline{\boldsymbol{F}}}^{-1} = \dot{\overline{\text{Grad}\,\gamma_\chi}} \cdot \underline{\underline{\boldsymbol{F}}}^{-1} = \dot{\underline{\boldsymbol{K}}} \cdot \underline{\underline{\boldsymbol{F}}}^{-1}, \tag{6}$$

Note that Eq. (5) represents the classical velocity gradient $\underline{\underline{\boldsymbol{L}}} = \dot{\underline{\underline{\boldsymbol{F}}}} \cdot \underline{\underline{\boldsymbol{F}}}^{-1}$.

2.2. Principle of virtual power and generalized balance of momentum

The method of virtual power is used to formulate the balance equations in the static case, following the approach of Germain (1973) for general micromorphic media. The virtual motion of a subdomain D of the body $\mathbf{B}$ is specified by a given generalized virtual velocity $\mathcal{V} = \{\dot{\underline{\boldsymbol{u}}}, \dot{\gamma}_\chi\}$. The principle of virtual power asserts that, given any subdomain D, the virtual power of internal forces P^i is equal to the virtual power of external forces P^e for any virtual motion $\mathcal{V}$.

The volume density, p^i, of virtual power of internal forces is a linear form with respect to the generalized velocity and its gradient. For objectivity reasons, it does not depend on the velocity $\dot{\underline{\boldsymbol{u}}}$. As a result, it comprises three parts, which are associated respectively to the velocity gradient, the microslip rate and its gradient:

$$P^i = \int_D p^i \, dV = \int_D \left(\underline{\underline{\sigma}} : \text{grad}\,\dot{\underline{\boldsymbol{u}}} + s\dot{\gamma}_\chi + \underline{\boldsymbol{m}} \cdot \text{grad}\,\dot{\gamma}_\chi\right) dV, \quad \forall D \subset \mathbf{B}, \tag{7}$$

where $\underline{\underline{\sigma}}$ is the Cauchy stress and s, $\underline{\boldsymbol{m}}$ are generalized stresses.

In the absence of body forces for the sake of brevity, the virtual power of external forces is assumed to arise from a surface traction $\underline{\boldsymbol{t}}$ related to the macroscopic motion and a generalized surface traction m related to the microslip:

$$P^e = \int_{\partial D} p^e \, dS = \int_{\partial D} \left(\underline{\boldsymbol{t}} \cdot \dot{\underline{\boldsymbol{u}}} + m\dot{\gamma}_\chi\right) dS, \quad \forall D \subset \mathbf{B}. \tag{8}$$

The principle of virtual power with Eq. (7) and Eq. (8) can be rephrased as

$$\int_D \left(\underline{\underline{\sigma}} : \text{grad}\,\dot{\underline{\boldsymbol{u}}} + s\dot{\gamma}_\chi + \underline{\boldsymbol{m}} \cdot \text{grad}\,\dot{\gamma}_\chi\right) dV = \int_{\partial D} \left(\underline{\boldsymbol{t}} \cdot \dot{\underline{\boldsymbol{u}}} + m\dot{\gamma}_\chi\right) dS, \quad \forall \dot{\underline{\boldsymbol{u}}}, \forall \dot{\gamma}_\chi, \forall D. \tag{9}$$

The exploitation of this principle provides two field balance equations and the Neumann boundary conditions:

$$\text{div}\,\underline{\underline{\sigma}} = 0 \quad \text{and} \quad \text{div}\,\underline{\boldsymbol{m}} - s = 0, \quad \forall \underline{\boldsymbol{x}} \in D, \tag{10}$$

$$\underline{\boldsymbol{t}} = \underline{\underline{\sigma}} \cdot \underline{\boldsymbol{n}}, \quad \text{and} \quad m = \underline{\boldsymbol{m}} \cdot \underline{\boldsymbol{n}}, \quad \forall \underline{\boldsymbol{x}} \in \partial D, \tag{11}$$

where $\underline{\boldsymbol{n}}$ is the normal to the surface element dS of the boundary ∂D in the current configuration.

The balance laws can then be expressed with respect to the reference configuration in the form

$$\text{Div}\,\underline{\underline{\boldsymbol{S}}} = 0 \quad \text{and} \quad \text{Div}\,\underline{\boldsymbol{M}} - S = 0, \quad \forall \underline{\boldsymbol{X}} \in \mathbf{B_0}, \tag{12}$$

where $\underline{\underline{\boldsymbol{S}}}$ is the usual Boussinesq stress tensor, and $\underline{\boldsymbol{M}}$ and S are defined by

$$\underline{\underline{\boldsymbol{S}}} = J\underline{\underline{\sigma}} \cdot \underline{\underline{\boldsymbol{F}}}^{-T}, \qquad S = Js, \qquad \underline{\boldsymbol{M}} = J\underline{\underline{\boldsymbol{F}}}^{-1} \cdot \underline{\boldsymbol{m}}, \tag{13}$$

and $J = \det(\underline{\underline{\boldsymbol{F}}})$. The Neumann boundary conditions then become

$$\underline{\boldsymbol{T}} = \underline{\underline{\boldsymbol{S}}}.\underline{\boldsymbol{n}}_0, \quad \text{and} \quad M = \underline{\boldsymbol{M}} \cdot \underline{\boldsymbol{n}}_0, \quad \forall \underline{\boldsymbol{X}} \in \partial D_0 \tag{14}$$

where $\underline{\boldsymbol{T}}$ is the surface traction measured with respect to ∂D_0, M is the generalized surface traction and $\underline{\boldsymbol{n}}_0$ is the normal to the surface element of the subdomain $D_0 \subset \mathbf{B_0}$.

2.3. Exploitation of the entropy imbalance and proposed constitutive equations

The elastic–plastic kinematics is described by the multiplicative decomposition of the deformation gradient $\underline{\underline{\boldsymbol{F}}}$:

$$\underline{\underline{\boldsymbol{F}}} = \underline{\underline{\boldsymbol{E}}} \cdot \underline{\underline{\boldsymbol{P}}}, \tag{15}$$

where $\underline{\underline{\boldsymbol{E}}}$ denotes the elastic part and $\underline{\underline{\boldsymbol{P}}}$ the plastic part of the deformation gradient $\underline{\underline{\boldsymbol{F}}}$. The reference and current local configurations in the tangent spaces at $\underline{\boldsymbol{X}}$ and $\underline{\boldsymbol{x}}$ respectively, are called C_0 and C. A local intermediate configuration $C_\sharp$ is then defined at each material point and at each time t, according to (Mandel, 1973). The volume mass density with respect to all three local configurations are called ρ_0, $\rho_\sharp$ and ρ with the relations:

$$J = \det(\underline{\underline{\boldsymbol{F}}}) = \frac{\rho_0}{\rho}, \quad J_e = \det(\underline{\underline{\boldsymbol{E}}}) = \frac{\rho_\sharp}{\rho}, \quad J_\sharp = \det(\underline{\underline{\boldsymbol{P}}}) = \frac{\rho_0}{\rho_\sharp}. \tag{16}$$

It is assumed that plastic deformation takes place through the slip of dislocations on prescribed lattice slip planes with normal $\underline{\boldsymbol{n}}^r$ along prescribed lattice slip direction $\underline{\boldsymbol{\ell}}^r$, and that the evolution of $\underline{\underline{\boldsymbol{P}}}$ is governed by the plastic slip γ^r on slip systems r via the relation

$$\dot{\underline{\underline{\boldsymbol{P}}}} \cdot \underline{\underline{\boldsymbol{P}}}^{-1} = \sum_{r=1}^{N} \dot{\gamma}^r \underline{\underline{\boldsymbol{N}}}^r \tag{17}$$

with the Schmid tensor $\underline{\underline{\boldsymbol{N}}}^r = \underline{\boldsymbol{\ell}}^r \otimes \underline{\boldsymbol{n}}^r$ and the total number of slip systems, N. The uniqueness of the decomposition (15) is obtained by choosing the isoclinic local configuration $C_\sharp$ where the crystal lattice has the same orientation as in C_0 (Mandel, 1973).

Plastic incompressibility is assumed in the following: $\det(\underline{\underline{\boldsymbol{P}}}) = J_\sharp = 1$, $\text{trace}\,\underline{\underline{\boldsymbol{N}}}^r = 0$ as usual in standard crystal plasticity. A cumulative total slip variable γ_{cum} is introduced as

$$\gamma_{cum} = \int_0^t \sum_{r=1}^{N} |\dot{\gamma}^r| \, dt. \tag{18}$$

γ_{cum} is related to the microslip variable γ_χ via a variable $e(\underline{\boldsymbol{X}}, t)$ called relative plastic slip and given by

$$e(\underline{\boldsymbol{X}}, t) = \gamma_{cum}(\underline{\boldsymbol{X}}, t) - \gamma_\chi(\underline{\boldsymbol{X}}, t). \tag{19}$$

The relative plastic slip variable e measures the deviation of γ_χ from γ_{cum} and will be associated with an energy cost in the free energy potential in the following.

Considering Eq. (15), the velocity gradient $\underset{\sim}{\mathbf{L}}$ can be expressed as

$$\underset{\sim}{\mathbf{L}} = \dot{\underset{\sim}{\mathbf{F}}}\underset{\sim}{\mathbf{F}}^{-1} = \underset{\sim}{\mathbf{L}}^e + \underset{\sim}{\mathbf{E}}\cdot\underset{\sim}{\mathbf{L}}^p\cdot\underset{\sim}{\mathbf{E}}^{-1} \quad \text{with} \quad \underset{\sim}{\mathbf{L}}^e = \dot{\underset{\sim}{\mathbf{E}}}\cdot\underset{\sim}{\mathbf{E}}^{-1} \quad \text{and} \quad \underset{\sim}{\mathbf{L}}^p = \dot{\underset{\sim}{\mathbf{P}}}\cdot\underset{\sim}{\mathbf{P}}^{-1}. \tag{20}$$

Using Eqs. (20) and (19), the internal power density p^i in Eq. (7) can be further developed as

$$p^i = J_e^{-1}\underset{\sim}{\mathbf{\Pi}}^e : \dot{\underset{\sim}{\mathbf{E}}}^e_{GL} + J_e^{-1}\underset{\sim}{\mathbf{\Pi}}^M : (\dot{\underset{\sim}{\mathbf{P}}}\cdot\underset{\sim}{\mathbf{P}}^{-1}) + s(\dot{\gamma}_{cum} - \dot{e}) + \underline{\boldsymbol{m}}.\mathrm{grad}\,\dot{\gamma}_\chi \tag{21}$$

with

$$\underset{\sim}{\mathbf{\Pi}}^e = J_e\underset{\sim}{\mathbf{E}}^{-1}\cdot\underset{\sim}{\sigma}.\underset{\sim}{\mathbf{E}}^{-T},\quad \underset{\sim}{\mathbf{\Pi}}^M = J_e\underset{\sim}{\mathbf{E}}^T\cdot\underset{\sim}{\sigma}.\underset{\sim}{\mathbf{E}}^{-T} = \underset{\sim}{\mathbf{E}}^T\cdot\underset{\sim}{\mathbf{E}}.\underset{\sim}{\mathbf{\Pi}}^e,$$
$$\underset{\sim}{\mathbf{E}}^e_{GL} = \frac{1}{2}\left(\underset{\sim}{\mathbf{E}}^T\cdot\underset{\sim}{\mathbf{E}} - \underset{\sim}{\mathbf{1}}\right) \tag{22}$$

where $\underset{\sim}{\mathbf{E}}^e_{GL}$ denotes the Green-Lagrange elastic strain tensor, $\underset{\sim}{\mathbf{\Pi}}^e$ is the Piola stress tensor w.r.t. $C_\sharp$ and $\underset{\sim}{\mathbf{\Pi}}^M$ the Mandel stress tensor. The last term in Eq. (21) can also be expressed in terms of Lagrangian variables, after considering Eqs. (6) and (13):

$$\underline{\boldsymbol{m}}\cdot\mathrm{grad}\,\dot{\gamma}_\chi = J^{-1}\underline{\boldsymbol{M}}\cdot\mathrm{Grad}\,\dot{\gamma}_\chi = J^{-1}\underline{\boldsymbol{M}}\cdot\dot{\underline{\boldsymbol{K}}} \tag{23}$$

where the generalized stress tensors $\underline{\boldsymbol{m}}$ and $\underline{\boldsymbol{M}}$ are still related by Eq. (13). As a result, Eqs. (21) and (23) yield

$$p^i = J_e^{-1}\underset{\sim}{\mathbf{\Pi}}^e : \dot{\underset{\sim}{\mathbf{E}}}^e_{GL} + J_e^{-1}\underset{\sim}{\mathbf{\Pi}}^M : (\dot{\underset{\sim}{\mathbf{P}}}\cdot\underset{\sim}{\mathbf{P}}^{-1}) + s(\dot{\gamma}_{cum} - \dot{e}) + J^{-1}\underline{\boldsymbol{M}}\cdot\dot{\underline{\boldsymbol{K}}}. \tag{24}$$

In the present model, the vector microslip gradient variable $\underline{\boldsymbol{K}}$ and the relative plastic slip e are assumed to be state variables in addition to the usual elastic strain $\underset{\sim}{\mathbf{E}}_{GL}$. The free energy density ψ is hence a function of the Lagrangian variables $\underset{\sim}{\mathbf{E}}_{GL}$, $\underline{\boldsymbol{K}}$ and e:

$$\psi = \psi\left(\underset{\sim}{\mathbf{E}}^e_{GL}, e, \underline{\boldsymbol{K}}\right). \tag{25}$$

Additional internal variables accounting for size–independent hardening will be added later on but they are omitted here for the sake of brevity. It follows that

$$\rho\dot{\psi} = \rho\frac{\partial\psi}{\partial\underset{\sim}{\mathbf{E}}^e_{GL}} : \dot{\underset{\sim}{\mathbf{E}}}^e_{GL} + \rho\frac{\partial\psi}{\partial e}\dot{e} + \rho\frac{\psi}{\underline{\boldsymbol{K}}}\cdot\dot{\underline{\boldsymbol{K}}}. \tag{26}$$

The second principle of thermodynamics is now invoked in the following isothermal local form

$$p^i - \rho\dot{\psi} \geqslant 0. \tag{27}$$

The combination of Eqs. (26), (24) and (27) leads to the Clausius–Duhem inequality:

$$\rho\left(\frac{\underset{\sim}{\mathbf{\Pi}}^e}{\rho_\sharp} - \frac{\partial\psi}{\partial\underset{\sim}{\mathbf{E}}^e_{GL}}\right) : \dot{\underset{\sim}{\mathbf{E}}}^e_{GL} + J_e^{-1}\underset{\sim}{\mathbf{\Pi}}^M : \left(\dot{\underset{\sim}{\mathbf{P}}}\underset{\sim}{\mathbf{P}}^{-1}\right)$$
$$-\left(s + \rho\frac{\partial\psi}{\partial e}\right)\dot{e} + \rho\left(\frac{\underline{\boldsymbol{M}}}{\rho_0} - \frac{\partial\psi}{\partial\underline{\boldsymbol{K}}}\right)\cdot\dot{\underline{\boldsymbol{K}}} + s\dot{\gamma}_{cum} \geqslant 0. \tag{28}$$

The left–hand side is considered as a linear form with respect to the variables $\dot{\underset{\sim}{\mathbf{E}}}^e_{GL}$, $\dot{e}$ and $\dot{\underline{\boldsymbol{K}}}$. The conjugate forces must then vanish to fulfill the positivity of dissipation. This provides the following state laws:

$$\underset{\sim}{\mathbf{\Pi}}^e = \rho_\sharp\frac{\partial\psi}{\partial\underset{\sim}{\mathbf{E}}^e_{GL}},\quad s = -\rho\frac{\partial\psi}{\partial e},\quad \underline{\boldsymbol{M}} = \rho_0\frac{\partial\psi}{\partial\underline{\boldsymbol{K}}}. \tag{29}$$

The two last state laws assume that the relations between the generalized stresses and the microslip and microslip gradient are purely energetic and that no dissipative part is considered for them. This assumption is part of the objective of the work, namely to propose the most simple constitutive choices for the higher order contributions. From Eq. (28), the residual dissipation is obtained as

$$d^{res} = J_e^{-1}\underset{\sim}{\mathbf{\Pi}}^M : \left(\dot{\underset{\sim}{\mathbf{P}}}\underset{\sim}{\mathbf{P}}^{-1}\right) + s\dot{\gamma}_{cum} \geqslant 0. \tag{30}$$

Given Eq. (17), the plastic power can be decomposed into the contributions of individual slip systems:

$$\underset{\sim}{\mathbf{\Pi}}^M : \left(\dot{\underset{\sim}{\mathbf{P}}}\underset{\sim}{\mathbf{P}}^{-1}\right) = \underset{\sim}{\mathbf{\Pi}}^M : \left(\sum_{r=1}^N \dot{\gamma}^r\underset{\sim}{\mathbf{N}}^r\right) = \sum_{r=1}^N\left(\underset{\sim}{\mathbf{\Pi}}^M : \underset{\sim}{\mathbf{N}}^r\right)\dot{\gamma}^r = \sum_{r=1}^N \tau^r\dot{\gamma}^r, \tag{31}$$

with the resolved shear stress $\tau^r = \underset{\sim}{\mathbf{\Pi}}^M : \underset{\sim}{\mathbf{N}}^r$ in $C_\sharp$. Thus, the residual dissipation inequality writes

$$d^{res} = J_e^{-1}\sum_{r=1}^N \tau^r\dot{\gamma}^r + s\dot{\gamma}_{cum} = J_e^{-1}\sum_{r=1}^N \tau^r\dot{\gamma}^r + s\sum_{r=1}^N|\dot{\gamma}^r| \geqslant 0 \tag{32}$$

where the definition of γ_{cum} given by Eq. (18) has been taken into account. Noticing that $\mathrm{sign}(\tau^r) = \mathrm{sign}(\gamma^r)$ and $\tau^r\dot{\gamma}^r = |\tau^r||\dot{\gamma}^r|$, Eq. (32) can be further written as

$$d^{res} = J_e^{-1}\sum_{r=1}^N|\tau^r|\ |\dot{\gamma}^r| + s\sum_{r=1}^r|\dot{\gamma}^r| = J_e^{-1}\sum_{r=1}^N\left(|\tau^r| + J_e s\right)|\dot{\gamma}^r| \geqslant 0. \tag{33}$$

The previous form of the dissipation rate gives an incentive to introduce the following yield function:

$$f^r = |\tau^r| + J_e s - \tau_c^r = |\tau^r| - (\tau_c^r - J_e s),\ \forall r = 1, 2, \ldots, N, \tag{34}$$

where τ_c^r is the critical resolved shear stress (CRSS) for the slip system r. This corresponds to the usual Schmid law complemented by the enhancement of hardening based on the generalized stress s. The generalized stress s is therefore regarded as a source of isotropic hardening for each slip system. Finally, a rate-dependent flow rule is chosen for the plastic slip γ^r, expressed as

$$\dot{\gamma}^r = \dot{\gamma}_0\left\langle\frac{|\tau^r| - \langle\tau_c^r - J_e s\rangle}{\sigma_0}\right\rangle^n \mathrm{sign}(\tau^r) \tag{35}$$

where $\langle\bullet\rangle = \mathrm{Max}(\bullet, 0)$ and $\sigma_0, \dot{\gamma}_0, n$ are viscosity parameters. It may happen that $\tau_c^r - J_e s < 0$. That is why the definition of the threshold is $\langle\tau_c^r - J_e s\rangle$.

2.4. Alternative formulation of constitutive equations

In the previous sections, the constitutive equations were proposed using the state variable $\underline{\boldsymbol{K}}$, i.e. the Lagrangian microslip gradient, as an argument of the free energy density function. It would be equivalent to consider the Eulerian variable $\underline{\boldsymbol{k}}$, provided that the proper transport rules by $\underset{\sim}{\mathbf{F}}$ are used in the derivation. The drawback of the previous formulation is that the arguments of the free energy functions mix Lagrangian (or Eulerian) with variables defined on the intermediate configuration $C_\sharp$ like $\underset{\sim}{\mathbf{E}}^e_{GL}$. It is therefore proposed here to push forward $\underline{\boldsymbol{K}}$ into $C_\sharp$, or equivalently pull back $\underline{\boldsymbol{k}}$ into $C_\sharp$, and define $\underline{\boldsymbol{K}}^\sharp$ as:

$$\underline{\boldsymbol{K}}^\sharp = \underset{\sim}{\mathbf{P}}^{-T}\cdot\underline{\boldsymbol{K}} = \underset{\sim}{\mathbf{E}}^T\cdot\underline{\boldsymbol{k}}. \tag{36}$$

The generalized stress $\underline{\boldsymbol{M}}^\sharp$, work-conjugate to $\underline{\boldsymbol{K}}^\sharp$ in the intermediate configuration $C_\sharp$ can be found according to the requirement that the work generated by $\underline{\boldsymbol{M}}$ over the vector microslip variable $\underline{\boldsymbol{K}}$ on a volume element dV_0 in C_0 is equal to that by $\underline{\boldsymbol{M}}^\sharp$ over $\underline{\boldsymbol{K}}^\sharp$ on the volume element $dV_\sharp$ in $C_\sharp$. Thus, $\underline{\boldsymbol{M}}.\underline{\boldsymbol{K}}$ follows

$$\underline{\boldsymbol{M}}.\underline{\boldsymbol{K}}\,dV_0 = J_\sharp^{-1}\underline{\boldsymbol{M}}.\underline{\boldsymbol{K}}\,dV_\sharp = J_\sharp^{-1}\underline{\boldsymbol{M}}.\underset{\sim}{\mathbf{P}}^T\cdot\underset{\sim}{\mathbf{P}}^{-T}\cdot\underline{\boldsymbol{K}}\,dV_\sharp$$
$$= J_\sharp^{-1}\underline{\boldsymbol{M}}.\underset{\sim}{\mathbf{P}}^T\cdot\underline{\boldsymbol{K}}^\sharp\,dV_\sharp = \underline{\boldsymbol{M}}^\sharp.\underline{\boldsymbol{K}}^\sharp\,dV_\sharp, \tag{37}$$

where

$$\underline{\boldsymbol{M}}^{\sharp} = J_{\sharp}^{-1}\underline{\boldsymbol{M}}.\underline{\mathbf{P}}^{T} = J_{\sharp}^{-1}\underline{\mathbf{P}}.\underline{\boldsymbol{M}} = J_e\underline{\mathbf{F}}^{e-1}\cdot\underline{\boldsymbol{m}} \tag{38}$$

which is obtained after substitution of Eq. (13). Accordingly, an alternative constitutive formulation can be proposed for which the free energy potential depends on strain measures defined on the same intermediate configuration, i.e., $\psi = \psi\left(\underline{\mathbf{E}}^{e}_{GL}, e, \underline{\boldsymbol{K}}^{\sharp}\right)$. Substitution of Eqs. (36) and (38) into the power density of internal forces, Eq. (24), leads to

$$\begin{aligned} p^i &= J_e^{-1}\underline{\boldsymbol{\Pi}}^{e} : \dot{\underline{\mathbf{E}}}^{e}_{GL} + J_e^{-1}\underline{\boldsymbol{\Pi}}^{M} : (\dot{\underline{\mathbf{P}}}\cdot\underline{\mathbf{P}}^{-1}) \\ &\quad + s(\dot{\gamma}_{cum} - \dot{e}) + J_e^{-1}\underline{\mathbf{P}}^{-1}\cdot\underline{\boldsymbol{M}}^{\sharp}.(\dot{\underline{\mathbf{P}}}^{T}\cdot\underline{\boldsymbol{K}}^{\sharp} + \underline{\mathbf{P}}^{T}\cdot\dot{\underline{\boldsymbol{K}}}^{\sharp}) \\ &= J_e^{-1}\underline{\boldsymbol{\Pi}}^{e} : \dot{\underline{\mathbf{E}}}^{e}_{GL} + J_e^{-1}\underline{\boldsymbol{\Pi}}^{M} : (\dot{\underline{\mathbf{P}}}\cdot\underline{\mathbf{P}}^{-1}) \\ &\quad + s(\dot{\gamma}_{cum} - \dot{e}) + J_e^{-1}(\underline{\boldsymbol{K}}^{\sharp}\otimes\underline{\boldsymbol{M}}^{\sharp}) : (\dot{\underline{\mathbf{P}}}\cdot\underline{\mathbf{P}}^{-1}) + J_e^{-1}\underline{\boldsymbol{M}}^{\sharp}\cdot\dot{\underline{\boldsymbol{K}}}^{\sharp}. \end{aligned} \tag{39}$$

This expression can be substituted into the entropy inequality, Eq. (27), taking into account the new argument of the Helmholtz free energy function:

$$\begin{aligned} p^i - \rho\dot{\psi} &= \rho\left(\frac{\underline{\boldsymbol{\Pi}}^{e}}{\rho_{\sharp}} - \frac{\partial\psi}{\partial\underline{\mathbf{E}}^{e}_{GL}}\right) : \dot{\underline{\mathbf{E}}}^{e}_{GL} - \left(s + \rho\frac{\partial\psi}{\partial e}\right)\dot{e} \\ &\quad + \rho\left(\frac{\underline{\boldsymbol{M}}^{\sharp}}{\rho_{\sharp}} - \frac{\partial\psi}{\partial\underline{\boldsymbol{K}}^{\sharp}}\right).\dot{\underline{\boldsymbol{K}}}^{\sharp} \\ &\quad + J_e^{-1}(\underline{\boldsymbol{\Pi}}^{M} + \underline{\boldsymbol{K}}^{\sharp}\otimes\underline{\boldsymbol{M}}^{\sharp}) : (\dot{\underline{\mathbf{P}}}\cdot\underline{\mathbf{P}}^{-1}) + s\dot{\gamma}_{cum} \geqslant 0. \end{aligned} \tag{40}$$

A hyperelastic relationship is chosen between the generalized stress and microslip gradient w.r.t. the intermediate configuration:

$$\underline{\boldsymbol{M}}^{\sharp} = \rho_{\sharp}\frac{\partial\psi}{\partial\underline{\boldsymbol{K}}^{\sharp}} \tag{41}$$

so that the residual dissipation inequality becomes

$$\begin{aligned} d^{res} &= J_e^{-1}\left(\underline{\boldsymbol{\Pi}}^{M} + \underline{\boldsymbol{K}}^{\sharp}\otimes\underline{\boldsymbol{M}}^{\sharp}\right) : \left(\dot{\underline{\mathbf{P}}}\underline{\mathbf{P}}^{-1}\right) + s\dot{\gamma}_{cum} \\ &= J_e^{-1}\left(\underline{\boldsymbol{\Pi}}^{M} + \underline{\boldsymbol{K}}^{\sharp}\otimes\underline{\boldsymbol{M}}^{\sharp}\right) : \left(\sum_{r=1}^{N}\dot{\gamma}^{r}\underline{\mathbf{N}}^{r}\right) + s\sum_{r=1}^{N}|\dot{\gamma}^{r}| \geqslant 0. \end{aligned} \tag{42}$$

This expression of the dissipation rate can be rewritten in the form:

$$\begin{aligned} d^{res} &= J_e^{-1}\sum_{r=1}^{N}\left\{\left[\tau^{r} + (\underline{\boldsymbol{K}}^{\sharp}\cdot\underline{\boldsymbol{\ell}}^{r})(\underline{\boldsymbol{M}}^{\sharp}\cdot\underline{\boldsymbol{n}}^{r})\right]\dot{\gamma}^{r} + J_e s|\dot{\gamma}^{r}|\right\} \\ &= J_e^{-1}\sum_{r=1}^{N}\left(|\tau^{\sharp r}| + J_e s\right)|\dot{\gamma}^{r}| \geqslant 0, \end{aligned} \tag{43}$$

where a generalized resolved shear stress arises that can be defined as

$$\tau^{\sharp r} = \tau^{r} - x^{r} \qquad \text{with} \quad x^{r} = -(\underline{\boldsymbol{K}}^{\sharp}\cdot\underline{\boldsymbol{\ell}}^{r})(\underline{\boldsymbol{M}}^{\sharp}\cdot\underline{\boldsymbol{n}}^{r}). \tag{44}$$

The residual dissipation Eq. (43) therefore takes the same form as Eq. (33), except that τ^{r} is replaced by $\tau^{\sharp r}$. Moreover, the variable x^{r} plays the role of a back-stress for each slip system, induced by the higher order stress and microslip gradient. The following alternative yield function is thus proposed in the form:

$$\begin{aligned} &f^{r} = |\tau^{\sharp r}| - (\tau_c^{r} - J_e s) = |\tau^{r} + (\underline{\boldsymbol{K}}^{\sharp}.\underline{\boldsymbol{\ell}}^{r})(\underline{\boldsymbol{M}}^{\sharp}.\underline{\boldsymbol{n}}^{r})| - (\tau_c^{r} - J_e s), \\ &\forall r = 1, 2, \ldots, N. \end{aligned} \tag{45}$$

Compared with the previous formulation of the theory, gradient terms come into play not only through isotropic hardening but also in the form of kinematic hardening, as a result of the introduction of the microslip gradient measure w.r.t. the intermediate configuration. Finally, the rate-dependent flow rule for each system becomes:

$$\dot{\gamma}^{r} = \dot{\gamma}_0\left\langle\frac{|\tau^{\sharp r}| - \langle\tau_c^{r} - J_e s\rangle}{\sigma_0}\right\rangle^{n}\operatorname{sign}\left(\tau^{\sharp r}\right). \tag{46}$$

2.5. Hardening laws

The hardening laws describe the evolution of the critical resolved shear stress τ_c^{r} depending on appropriate internal variables. In the present work, the hardening laws are based on the evolution of usual scalar dislocation densities. Following Kubin et al. (2008), τ_c^{r} of the slip system r can be expressed as:

$$\tau_c^{r} = \tau_0 + \mu\sqrt{\sum_{u=1}^{N}a^{ru}\varrho^{u}}, \tag{47}$$

where τ_0 is the thermal component of the CRSS due to lattice friction, ϱ^{r} denotes adimensional dislocation density (ϱ^{r}/b^2 is the usual scalar dislocation density, i.e. the length of dislocation lines per unit volume, and b is the norm of Burgers vector of the dislocation $\underline{\boldsymbol{b}}$), μ is the shear modulus, and a^{ru} is the interaction matrix describing long-range interactions between dislocations.

The evolution equation for the adimensional dislocation density ϱ^{r}

$$\dot{\varrho}^{r} = |\dot{\gamma}^{r}|\left(\frac{\sqrt{\sum_{u=1}^{N}b^{ru}\varrho^{u}}}{\kappa} - G_c\varrho^{r}\right) \tag{48}$$

accounts for multiplication and annihilation of dislocations. The parameter κ is proportional to the number of obstacles crossed by a dislocation before being immobilized, G_c is the critical distance controlling the annihilation of dislocations with opposite signs, and the matrix b^{ru} describes the interactions between dislocations. The structure of the matrices a^{ru} and b^{ru} is given in Appendix A for FCC crystals.

3. Constitutive choices for the free energy potential and associated regularization operators

Among many possible constitutive choices for the form of the free energy density, quadratic functions are selected in the present work, quadratic with respect to the three available microslip gradient measures: $\underline{\boldsymbol{K}}$, $\underline{\boldsymbol{K}}^{\sharp}$ and $\underline{\boldsymbol{k}}$. The Lagrangian and Eulerian variables are first discussed followed by the alternative choice $\underline{\boldsymbol{K}}^{\sharp}$. In all cases, the partial differential equation governing the microslip variable is then derived.

3.1. Formulation with a free energy potential depending on $\underline{\mathbf{K}}$ or $\underline{\mathbf{k}}$

The choice of quadratic potentials leads to linear relationships between suitable higher order stress and strain variables. The reason for such a simple choice is to provide linear regularization operators, at least w.r.t. to some variable. Full linearity is lost at large deformations in any case and the properties of corresponding regularization operators must be studied, see (Forest, 2016). Such relations are first derived for Lagrangian and Eulerian higher order stress variables.

Model based on the state law $\underline{\boldsymbol{M}} = \underline{\mathbf{A}}\cdot\underline{\boldsymbol{K}}$. A first quadratic potential is considered in the form:

$$\rho_0\psi(\underline{\mathbf{E}}^{e}_{GL}, e, \underline{\boldsymbol{K}}) = \frac{1}{2}J_{\sharp}\underline{\mathbf{E}}^{e}_{GL} : \underline{\underline{\boldsymbol{\Lambda}}} : \underline{\mathbf{E}}^{e}_{GL} + \frac{1}{2}H_{\chi}e^2 + \frac{1}{2}\underline{\boldsymbol{K}}\cdot\underline{\mathbf{A}}\cdot\underline{\boldsymbol{K}}, \tag{49}$$

where $\underline{\underline{\boldsymbol{\Lambda}}}$ is the fourth rank tensor of elastic moduli, H_{χ} a penalty modulus and $\underline{\mathbf{A}}$ a second rank tensor of high order moduli. With this potential, the constitutive relations Eq. (29) yield

$$\underline{\boldsymbol{\Pi}}^{e} = \underline{\underline{\boldsymbol{\Lambda}}} : \underline{\mathbf{E}}^{e}_{GL}, \quad s = -J^{-1}H_{\chi}e, \quad \underline{\boldsymbol{M}} = \underline{\mathbf{A}}\cdot\underline{\boldsymbol{K}}. \tag{50}$$

Noticing that $S = Js$, one can rewrite the second constitutive law as

$$S = -H_{\chi}e. \tag{51}$$

A consequence of the choice Eq. (50) is that the relation between Eulerian higher order stress and microslip gradient is nonlinear, after substitution of Eqs. (3) and (13):

$$\underline{\boldsymbol{m}} = J^{-1}\underline{\underline{\mathbf{F}}}\cdot\underline{\underline{\mathbf{A}}}\cdot\underline{\underline{\mathbf{F}}}^{T}\cdot\underline{\boldsymbol{k}}. \tag{52}$$

Noticing that $\rho_\sharp = \rho_0$, i.e. $J_\sharp = 1$, $S = Js$, and the balance law Eq. (12), the yield function Eq. (34) can be written as

$$\begin{aligned} f^r &= |\tau^r| - (\tau_c^r - J_e s) = |\tau^r| - (\tau_c^r - Js) = |\tau^r| - (\tau_c^r - S) \\ &= |\tau^r| - (\tau_c^r - \mathrm{Div}\,\underline{\boldsymbol{M}}). \end{aligned} \tag{53}$$

In the present work, the model will be applied to crystals with cubic symmetry. It follows that the second order tensor $\underline{\underline{\mathbf{A}}}$ must be spherical, i.e., $\underline{\underline{\mathbf{A}}} = A\underline{\underline{\mathbf{1}}}$. The constitutive relations Eqs. (50) and (52) thus become

$$\underline{\boldsymbol{M}} = A\underline{\boldsymbol{K}}, \quad \text{i.e.} \quad \underline{\boldsymbol{m}} = J^{-1}A\underline{\underline{\mathbf{B}}}\cdot\underline{\boldsymbol{k}} \tag{54}$$

where $\underline{\underline{\mathbf{B}}} = \underline{\underline{\mathbf{F}}}.\underline{\underline{\mathbf{F}}}^{T}$ is the left Cauchy–Green tensor. This constitutive law can be substituted into the yield function to get

$$f^r = |\tau^r| - \left(\tau_c^r - A\mathrm{Div}\left(\mathrm{Grad}\,\gamma_\chi\right)\right) = |\tau^r| - \left(\tau_c^r - A\,\triangle_X\gamma_\chi\right), \tag{55}$$

where $\triangle_X$ is the Laplace operator w.r.t. to Lagrangian coordinates. As can be seen in this expression, the term $\mathrm{Grad}\,\gamma_\chi$ comes into play as a source of isotropic hardening proportional to the Laplacian of microslip in the spirit of the Aifantis model (Aifantis, 1987). Moreover, the regularization equation connecting γ_χ and γ_{cum} is obtained by combining Eqs. (19), (12), (54) and (51)

$$\gamma_\chi - \frac{A}{H_\chi}\,\triangle_X\gamma_\chi = \gamma_{cum}, \tag{56}$$

where γ_{cum} acts as a source term, see (Peerlings et al., 1996). Here, the regularization equation with a Lagrangian Laplace operator $\triangle_X$ is thus obtained in the reference configuration.

Model based on the state law $\underline{\boldsymbol{m}} = \underline{\underline{\mathbf{A}}}.\underline{\boldsymbol{k}}$. In order to obtain a Eulerian Laplace operator in the regularization equation, a second potential $\psi(\underline{\underline{\mathbf{E}}}_{GL}, e, \underline{\boldsymbol{k}})$ is considered in the form:

$$\begin{aligned} \rho\psi = \frac{1}{2}J_e^{-1}\underline{\underline{\mathbf{E}}}_{GL}^{e} : \underline{\underline{\underline{\underline{\mathbf{\Lambda}}}}} : \underline{\underline{\mathbf{E}}}_{GL}^{e} + \frac{1}{2}H_\chi e^2 + \frac{1}{2}\underline{\boldsymbol{k}}\cdot\underline{\underline{\mathbf{A}}}\cdot\underline{\boldsymbol{k}} = \frac{1}{2}J_e^{-1}\underline{\underline{\mathbf{E}}}_{GL}^{e} : \underline{\underline{\underline{\underline{\mathbf{\Lambda}}}}} : \underline{\underline{\mathbf{E}}}_{GL}^{e} \\ + \frac{1}{2}H_\chi e^2 + \frac{1}{2}\underline{\boldsymbol{K}}\cdot\underline{\underline{\mathbf{F}}}^{-1}\cdot\underline{\underline{\mathbf{A}}}\cdot\underline{\underline{\mathbf{F}}}^{-T}\cdot\underline{\boldsymbol{K}}. \end{aligned} \tag{57}$$

The higher order state laws Eq. (29) now become

$$s = -H_\chi e, \quad \underline{\boldsymbol{M}} = J\underline{\underline{\mathbf{F}}}^{-1}\underline{\underline{\mathbf{A}}}\cdot\underline{\underline{\mathbf{F}}}^{-T}\cdot\underline{\boldsymbol{K}}, \quad \text{i.e.} \quad \underline{\boldsymbol{m}} = \underline{\underline{\mathbf{A}}}\cdot\underline{\boldsymbol{k}} \tag{58}$$

For crystals with cubic symmetry, i.e., $\underline{\underline{\mathbf{A}}} = A\underline{\underline{\mathbf{1}}}$, the constitutive relations Eq. (58) reduces to

$$\underline{\boldsymbol{M}} = JA\underline{\underline{\mathbf{C}}}^{-1}\cdot\underline{\boldsymbol{K}}, \quad \text{i.e.} \quad \underline{\boldsymbol{m}} = A\underline{\boldsymbol{k}}, \tag{59}$$

where $\underline{\underline{\mathbf{C}}} = \underline{\underline{\mathbf{F}}}^{T}\cdot\underline{\underline{\mathbf{F}}}$ is the right Cauchy–Green tensor. Following the same derivation procedure as in the previous section, the yield function Eq. (34) and the regularization equation write

$$f^r = |\tau^r| - \left(\tau_c^r - J_e A\ \mathrm{div}(\mathrm{grad}\,\gamma_\chi)\right) = |\tau^r| - \left(\tau_c^r - J_e A\,\triangle_x\gamma_\chi\right), \tag{60}$$

$$\gamma_\chi - \frac{A}{H_\chi}\,\triangle_x\gamma_\chi = \gamma_{cum}, \tag{61}$$

where the Eulerian Laplace operator $\triangle_x$ appears.

3.2. Formulation with a free energy potential depending on $\underline{\boldsymbol{K}}^\sharp$

In the following, the formulation presented in Section 2.4 is developed further. The choice of a free energy potential giving a linear relation between $\underline{\boldsymbol{K}}^\sharp$ and $\underline{\boldsymbol{M}}^\sharp$ is discussed, i.e. a

Model based on the state law $\underline{\boldsymbol{K}}^\sharp = \underline{\underline{\mathbf{A}}}\cdot\underline{\boldsymbol{M}}^\sharp$. An alternative quadratic free energy potential is proposed in the form:

$$\rho_\sharp\psi = \frac{1}{2}\underline{\underline{\mathbf{E}}}_{GL}^{e} : \underline{\underline{\underline{\underline{\mathbf{\Lambda}}}}} : \underline{\underline{\mathbf{E}}}_{GL}^{e} + \frac{1}{2}H_\chi e^2 + \frac{1}{2}\underline{\boldsymbol{K}}^\sharp.\underline{\underline{\mathbf{A}}}\cdot\underline{\boldsymbol{K}}^\sharp. \tag{62}$$

This represents the most consistent formulation in the sense that all the arguments are defined in the same local configuration. Substituting this potential into Eq. $(29)_2$ and Eq. (41), and assuming plastic incompressibility (i.e. $\rho_\sharp = \rho_0$), gives:

$$s = -J_e^{-1}H_\chi e, \quad \underline{\boldsymbol{M}}^\sharp = \underline{\underline{\mathbf{A}}}\cdot\underline{\boldsymbol{K}}^\sharp, \tag{63}$$

The Lagrangian form of the latter relation is nonlinear:

$$\underline{\boldsymbol{M}} = J_\sharp\underline{\underline{\mathbf{P}}}^{-1}\cdot\underline{\underline{\mathbf{A}}}\underline{\underline{\mathbf{P}}}^{-T}\cdot\underline{\boldsymbol{K}} \tag{64}$$

In the case of $\underline{\underline{\mathbf{A}}} = A\underline{\underline{\mathbf{1}}}$, the constitutive equations Eqs. (63) and (64) become

$$\underline{\boldsymbol{M}}^\sharp = A\underline{\boldsymbol{K}}^\sharp, \quad \underline{\boldsymbol{M}} = J_\sharp A\underline{\underline{\mathbf{C}}}^{p-1}\cdot\underline{\boldsymbol{K}}, \tag{65}$$

with $\underline{\underline{\mathbf{C}}}^p = \underline{\underline{\mathbf{P}}}^{T}\cdot\underline{\underline{\mathbf{P}}}$. Considering Eqs. (12) and (65), one can further write the yield function as

$$f^r = |\tau^{\sharp r}| - \left(\tau_c^r - J_\sharp^{-1}A\ \mathrm{Div}\,(J_\sharp\underline{\underline{\mathbf{C}}}^{p-1}\cdot\underline{\boldsymbol{K}})\right), \tag{66}$$

with

$$\begin{aligned} \tau^{\sharp r} &= \tau^r - x^r \quad \text{and} \quad x^r = -(\underline{\boldsymbol{K}}^\sharp\cdot\underline{\boldsymbol{\ell}}^r)(\underline{\boldsymbol{M}}^\sharp\cdot\underline{\boldsymbol{n}}^r) \\ &= -(\underline{\underline{\mathbf{P}}}^{-T}\cdot\underline{\boldsymbol{K}}\cdot\underline{\boldsymbol{\ell}}^r)(A\underline{\underline{\mathbf{P}}}^{-T}\cdot\underline{\boldsymbol{K}}\cdot\underline{\boldsymbol{n}}^r). \end{aligned} \tag{67}$$

The regularization operator is obtained after combining Eqs. (12) and (65):

$$\gamma_\chi - \frac{A}{H_\chi}J_\sharp^{-1}\mathrm{Div}\,(J_\sharp\underline{\underline{\mathbf{C}}}^{p-1}\cdot\mathrm{Grad}\,\gamma_\chi) = \gamma_{cum}. \tag{68}$$

It can be seen that the equation does not involve explicitly a Laplace operator in contrast to the previous formulations.

The regularisation operator can be rewritten with respect to Eulerian coordinates. For that purpose, the constitutive law Eqs. (13) and (38) must be transformed into a relation between Eulerian variables. With Eqs. (13) and (38), the expression of $\underline{\boldsymbol{m}}$ follows:

$$\underline{\boldsymbol{m}} = J^{-1}\underline{\underline{\mathbf{F}}}\cdot\underline{\boldsymbol{M}} = J_e^{-1}\underline{\underline{\mathbf{F}}}\cdot\underline{\boldsymbol{M}}^\sharp. \tag{69}$$

Combining Eqs. (3) and (36) gives $\underline{\boldsymbol{K}}^\sharp = \underline{\underline{\mathbf{F}}}^{T}\cdot\underline{\boldsymbol{k}}$ and, finally, the state law Eq. (63) yields

$$\underline{\boldsymbol{m}} = J_e^{-1}\underline{\underline{\mathbf{F}}}\cdot\underline{\underline{\mathbf{A}}}\cdot\underline{\underline{\mathbf{F}}}^{T}\cdot\underline{\boldsymbol{k}}. \tag{70}$$

For crystals with the cubic symmetry, the previous equation becomes

$$\underline{\boldsymbol{m}} = J_e^{-1}A\underline{\underline{\mathbf{B}}}^{e}\cdot\underline{\boldsymbol{k}}, \tag{71}$$

with $\underline{\underline{\mathbf{B}}}^{e} = \underline{\underline{\mathbf{F}}}.\underline{\underline{\mathbf{F}}}^{T}$. The yield function Eq. (45) and the regularization equation then write:

$$f^r = |\tau^{\sharp r}| - \left(\tau_c^r - J_e\mathrm{div}\left(J_e^{-1}A\underline{\underline{\mathbf{B}}}^{e}.\mathrm{grad}\,\gamma_\chi\right)\right) \leqslant 0, \tag{72}$$

$$\gamma_\chi - \frac{A}{H_\chi}\mathrm{div}\,(J_e^{-1}\underline{\underline{\mathbf{B}}}^{e}.\mathrm{grad}\,\gamma_\chi) = \gamma_{cum}. \tag{73}$$

This differential operator cannot be reduced to a Eulerian Laplace operator. It thus demonstrates that the second formulation based on $\underline{\boldsymbol{K}}^\sharp$ with the potential Eq. (62) does not lead to Lagrangian nor Eulerian Laplace operators in the regularization equation.

It is however possible to work with Lagrange or Euler Laplace operators in the regularization, still keeping the consitutive variable $\underline{\boldsymbol{K}}^\sharp$ and the associated kinematic hardening variables x^r. For that purpose, nonlinear relations linking $\underline{\boldsymbol{M}}^\sharp$ and $\underline{\boldsymbol{K}}^\sharp$ must be adopted. For example, the choice

$$\underline{\boldsymbol{M}}^\sharp = J_\sharp^{-1}\underline{\underline{\mathbf{P}}}\cdot\underline{\underline{\mathbf{A}}}\cdot\underline{\underline{\mathbf{P}}}^{T}\cdot\underline{\boldsymbol{K}}^\sharp \tag{74}$$

Table 1
Choices of the free energy for the two formulations. $\underline{\mathbf{A}} = A\underline{\mathbf{1}}$ is considered and $\rho\psi^e = \frac{1}{2}J_e^{-1}\underset{\sim}{\mathbf{E}}^e_{GL} : \underset{\approx}{\mathbf{\Lambda}} : \underset{\sim}{\mathbf{E}}^e_{GL}$.

	Formulation 1		Formulation 2
Yield function	$f^r = \lvert\tau^r\rvert - (\tau_c^r - J_e s)$		$f^r = \lvert\tau^s - x^r\rvert - (\tau_c^r - J_e s)$
Free energy potential	$\rho\psi^e + \frac{1}{2}J^{-1}H_\chi e^2 + \frac{1}{2}J^{-1}A\underline{\boldsymbol{K}}\cdot\underline{\boldsymbol{K}}$	$\rho\psi^e + \frac{1}{2}H_\chi e^2 + \frac{1}{2}A\underline{\boldsymbol{k}}\cdot\underline{\boldsymbol{k}}$	$\rho\psi^e + \frac{1}{2}J_e^{-1}H_\chi e^2 + \frac{1}{2}J_e^{-1}A\underline{\boldsymbol{K}}^\sharp\cdot\underline{\boldsymbol{K}}^\sharp$
Generalized stress s	$J^{-1}A\,\triangle_X\gamma_\chi$	$A\triangle_X\gamma_\chi$	$J^{-1}A\ \mathrm{Div}\,(J_\sharp\underset{\sim}{\mathbf{C}}^{p-1}\cdot\underline{\boldsymbol{K}})$ or $\mathrm{div}(J_e^{-1}A\underset{\sim}{\mathbf{B}}^e.\mathrm{grad}\,\gamma_\chi)$
Regularisation equation	$\gamma_\chi - \frac{A}{H_\chi}\triangle_X\gamma_\chi = \gamma_{cum}$	$\gamma_\chi - \frac{A}{H_\chi}\triangle_X\gamma_\chi = \gamma_{cum}$	$\gamma_\chi - \frac{A}{H_\chi}J_\sharp^{-1}\mathrm{Div}\,(J_\sharp\underset{\sim}{\mathbf{C}}^{p-1}\cdot\mathrm{Grad}\,\gamma_\chi) = \gamma_{cum}$ or $\gamma_\chi - \frac{A}{H_\chi}\mathrm{div}\,(J_e^{-1}\underset{\sim}{\mathbf{B}}^e.\mathrm{grad}\,\gamma_\chi) = \gamma_{cum}$

is equivalent to the linear relation $\underline{\boldsymbol{M}} = \underline{\mathbf{A}}\cdot\underline{\boldsymbol{K}}$. For crystals with cubic symmetry, this choice leads to the following expressions of the yield function, kinematic hardening and regularization equations:

$$f^r = \lvert\tau^{\sharp r}\rvert - \left(\tau_c^r - A\,\triangle_X\gamma_\chi\right) = \lvert\tau^r - x^r\rvert - \left(\tau_c^r - A\,\triangle_X\gamma_\chi\right) \leqslant 0, \tag{75}$$

$$x^r = -(\underline{\boldsymbol{K}}^\sharp\cdot\underline{\boldsymbol{\ell}}^r)(\underline{\boldsymbol{M}}^\sharp\cdot\underline{\boldsymbol{n}}^r) = -(\underset{\sim}{\mathbf{P}}^{-T}\cdot\underline{\boldsymbol{K}}\cdot\underline{\boldsymbol{\ell}}^r)(A\underset{\sim}{\mathbf{B}}^p\cdot\underset{\sim}{\mathbf{P}}^{-T}\cdot\underline{\boldsymbol{K}}\cdot\underline{\boldsymbol{n}}^r), \tag{76}$$

$$\gamma_\chi - \frac{A}{H_\chi}\triangle_X\gamma_\chi = \gamma_{cum}, \tag{77}$$

which involves the Lagrangian Laplace operator as expected. Note that this regularization function is the same as Eq. (56), except that it is defined with the generalized resolved shear stress $\tau^{\sharp r}$ instead of τ^r.

In order to obtain the Eulerian Laplace operator in the regularisation equation, the following nonlinear constitutive law is adopted:

$$\underline{\boldsymbol{M}}^\sharp = \underset{\sim}{\mathbf{E}}^{-1}\cdot\underline{\mathbf{A}}\cdot\underset{\sim}{\mathbf{E}}^{-T}\cdot\underline{\boldsymbol{K}}^\sharp \tag{78}$$

which is equivalent to the linear relation $\underline{\boldsymbol{m}} = \underline{\mathbf{A}}\cdot\underline{\boldsymbol{k}}$. For crystals with the cubic symmetry, this choice leads to the following expressions of the yield function, kinematic hardening and regularization equations:

$$f^r = \lvert\tau^{\sharp r}\rvert - \left(\tau_c^r - J_e A\,\triangle_x\gamma_\chi\right) = \lvert\tau^r - x^r\rvert - \left(\tau_c^r - J_e A\,\triangle_x\gamma_\chi\right) \leqslant 0, \tag{79}$$

$$x^r = -(\underline{\boldsymbol{K}}^\sharp.\underline{\boldsymbol{\ell}}^r)(\underline{\boldsymbol{M}}^\sharp.\underline{\boldsymbol{n}}^r) = -(\underset{\sim}{\mathbf{P}}^{-T}\cdot\underline{\boldsymbol{K}}.\underline{\boldsymbol{\ell}}^r)(A\underset{\sim}{\mathbf{C}}^{e-1}\cdot\underset{\sim}{\mathbf{P}}^{-T}\cdot\underline{\boldsymbol{K}}.\underline{\boldsymbol{n}}^r), \tag{80}$$

$$\gamma_\chi - \frac{A}{H_\chi}\triangle_x\gamma_\chi = \gamma_{cum}. \tag{81}$$

3.3. Summary

The choices for the free energy potential in the two proposed formulations are summarized in Table 1. The impact of these choices on the generalized stresses and regularisation equation is shown. For the sake of brevity, only the quadratic free energy depending on the variables defined w.r.t. the intermediate configuration is presented for the second formulation.

4. Numerical implementation

The implementation of the constitutive and balance laws of the *microslip* model is briefly described in this section. More detailed information can be found in Appendix A to Appendix D. The formulation of the model presented in Section 2.3 is chosen for the numerical implementation, with the free energy potential given by Eq. (49).

4.1. Integration of constitutive equations

The problem of the numerical integration of constitutive equations can be stated as follows: for given initial values of the stress variables $\underset{\sim}{\mathbf{S}}$, S and $\underline{\boldsymbol{M}}$ and associated internal variables v_{int} to be integrated, for given increments of the strain variables from $\underset{\sim}{\mathbf{F}}$, γ_χ, $\underline{\boldsymbol{K}}$ to $\underset{\sim}{\mathbf{F}}+\Delta\underset{\sim}{\mathbf{F}}$, $\gamma_\chi+\Delta\gamma_\chi$, $\underline{\boldsymbol{K}}+\Delta\underline{\boldsymbol{K}}$, what are the final values of the stress variables and internal variables v_{int}? The strain variables are referred to as the input variables (v_{IN}) and the stress variables as the output variables (v_{OUT}), the problem is briefly depicted in Fig. 1. For the sake of brevity, the increments of the variables are written in the rate form.

The increments $\dot{S}$ and $\dot{\underline{\mathbf{M}}}$ are directly derived from Eqs. (51) and (50), while the calculation of $\dot{\underset{\sim}{\mathbf{S}}}$ requires some further calculation. Combining Eqs. (22), (50) and (13) leads to

$$\underset{\sim}{\mathbf{S}} = J\varrho.\underset{\sim}{\mathbf{F}}^{-T} = \frac{1}{2}\frac{J}{J_e}\underset{\sim}{\mathbf{E}}\cdot\left(\underset{\approx}{\mathbf{\Lambda}} : (\underset{\sim}{\mathbf{E}}^T\cdot\underset{\sim}{\mathbf{E}} - \underline{\mathbf{1}})\right)\cdot\underset{\sim}{\mathbf{E}}^T\cdot\underset{\sim}{\mathbf{F}}^{-T}, \tag{82}$$

which shows that $\underset{\sim}{\mathbf{S}}$ depends on $\underset{\sim}{\mathbf{E}}$ and $\underset{\sim}{\mathbf{F}}$. The evolution equation governing $\underset{\sim}{\mathbf{E}}$ is deduced from Eq. (20). According to the constitutive Eqs. (17), (35) and (18), the differential equations that must be integrated are

$$\begin{cases} \dot{\underset{\sim}{\mathbf{E}}} = \dot{\underset{\sim}{\mathbf{F}}}\cdot\underset{\sim}{\mathbf{F}}^{-1}\cdot\underset{\sim}{\mathbf{E}} - \underset{\sim}{\mathbf{E}}.\left(\sum_{r=1}^{N}\dot{\gamma}^r\underline{\mathbf{N}}^r\right) & (83)\\ \dot{\gamma}^r = \dot{\gamma}_0\left\langle\frac{\lvert\tau^r\rvert - \left\langle\tau_c^r - S\right\rangle}{\sigma_0}\right\rangle^n \mathrm{sign}(\tau^r) & (84)\\ \dot{\varrho}^r = \lvert\dot{\gamma}^r\rvert\left(\frac{\sqrt{\sum_{u=1}^{N} b^{ru}\varrho^u}}{\kappa} - G_c\varrho^r\right) & (85)\\ \dot{\gamma}_{cum} = \sum_{r=1}^{N}\lvert\dot{\gamma}^r\rvert, & (86) \end{cases}$$

Note that it may happen that $\tau_c^r - S < 0$. In that case this value is replaced by 0 in the computation. Thus, the internal variables are $v_{\mathrm{int}} = \{\underset{\sim}{\mathbf{E}}, \gamma^r, \varrho^r, \gamma_{cum}\}$. The numerical integration of the differential equations is performed with the Newton-Raphson method which consists in solving the residual equations

$$\{R\} = \{\Delta v_{\mathrm{int}}\} - \Delta t\{\dot{v}_{\mathrm{int}}\}(t+\theta\Delta t) = \{0\}. \tag{87}$$

For the considered differential equations, the residual equations follow

$$\begin{cases} R_{\underset{\sim}{E}} = \Delta\underset{\sim}{\mathbf{E}} - \Delta\underset{\sim}{\mathbf{F}}.\underset{\sim}{\mathbf{F}}^{-1}\cdot\underset{\sim}{\mathbf{E}} + \underset{\sim}{\mathbf{E}}.\left(\sum_{r=1}^{N}\Delta\gamma^r\underline{\mathbf{N}}^r\right) & (88)\\ R_{\gamma^r} = \Delta\gamma^r - \dot{\gamma}_0\left\langle\frac{\lvert\tau^r\rvert - \left\langle\tau_c^r - S\right\rangle}{\sigma_0}\right\rangle^n \mathrm{sign}(\tau^r)\Delta t, & (89)\\ R_{\varrho^r} = \Delta\varrho^r - \lvert\Delta\gamma^r\rvert\left(\frac{\sqrt{\sum_{u=1}^{N} b^{ru}\varrho^u}}{\kappa} - G_c\varrho^r\right) & (90)\\ R_{\gamma_{cum}} = \Delta\gamma_{cum} - \sum_{r=1}^{N}\lvert\Delta\gamma^r\rvert & (91) \end{cases}$$

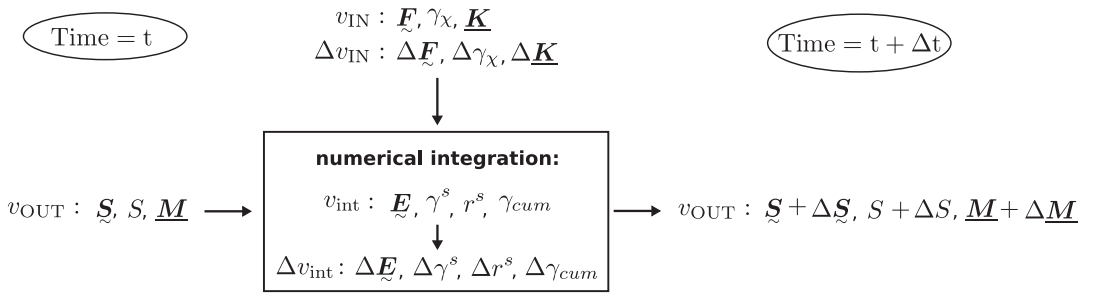

Fig. 1. Problem setup of the numerical integration of the constitutive equations.

Within the Newton-Raphson algorithm, the Jacobian matrix $[\mathcal{J}]$ needs to be evaluated and writes

$$[\mathcal{J}] = \frac{\partial\{R\}}{\partial\{\Delta v_{\mathrm{int}}\}}. \tag{92}$$

The Jacobian matrix for the previous residual equation system can be expressed as a partitioned matrix

$$\begin{pmatrix} \frac{\partial R_{\underset{\sim}{\boldsymbol{E}}}}{\partial\Delta_{\underset{\sim}{\boldsymbol{E}}}} & \frac{\partial R_{\underset{\sim}{\boldsymbol{E}}}}{\partial\Delta\gamma^p} & \frac{\partial R_{\underset{\sim}{\boldsymbol{E}}}}{\partial\Delta r^q} & \frac{\partial R_{\underset{\sim}{\boldsymbol{E}}}}{\partial\Delta\gamma_{cum}} \\ \frac{\partial R_{\gamma^r}}{\partial\Delta_{\underset{\sim}{\boldsymbol{E}}}} & \frac{\partial R_{\gamma^r}}{\partial\Delta\gamma^p} & \frac{\partial R_{\gamma^r}}{\partial\Delta r^q} & \frac{\partial R_{\gamma^r}}{\partial\Delta\gamma_{cum}} \\ \frac{\partial R_{\varrho^r}}{\partial\Delta_{\underset{\sim}{\boldsymbol{E}}}} & \frac{\partial R_{\varrho^r}}{\partial\Delta\gamma^p} & \frac{\partial R_{\varrho^r}}{\partial\Delta r^q} & \frac{\partial R_{\varrho^r}}{\partial\Delta\gamma_{cum}} \\ \frac{\partial R_{\gamma_{cum}}}{\partial\Delta_{\underset{\sim}{\boldsymbol{E}}}} & \frac{\partial R_{\gamma_{cum}}}{\partial\Delta\gamma^p} & \frac{\partial R_{\gamma_{cum}}}{\partial\Delta r^q} & \frac{\partial R_{\gamma_{cum}}}{\partial\Delta\gamma_{cum}} \end{pmatrix}. \tag{93}$$

Analytical expressions for each block are given in Appendix B.

In addition, the integration of Eq. (35) displays specific difficulties, because of the penalty parameter H_χ in Eq. (51) which should take a large enough value. To improve the convergence, the algorithm proposed by Wulfinghoff and Böhlke (2013) within Newton's method is used in this work.

4.2. Finite element formulation

The model is implemented in the finite element (FE) code `Zset` using a total Lagrangian finite element formulation in 3D following (Besson and Foerch, 1997; package, 2013). To this end, the principle of virtual power, given by Eq. (9) is expressed w.r.t. the initial configuration C_0:

$$\int_{D_0} \underset{\sim}{\boldsymbol{S}} : \dot{\underset{\sim}{\boldsymbol{F}}} + S\dot{\gamma}_\chi + \underline{\boldsymbol{M}}\,.\,\underline{\dot{\boldsymbol{K}}}\; dV_0 = \int_{\partial D_0} \left(\underline{\boldsymbol{T}}\cdot\underline{\dot{\boldsymbol{u}}} + M\dot{\gamma}_\chi\right) dS_0. \tag{94}$$

The FE problem will be solved by a monolithic iterative method.

Tensors and vectors are written in index notation, except otherwise stated. Besides the displacements u_i, the microslip γ_χ is regarded as an additional nodal degree of freedom. Assuming that the considered crystalline body occupying the domain D_0 in C_0 is discretized by n finite elements, the principle of virtual power (Eq. (94)) is discretized as

$$\sum_{e=1}^{n}\int_{D_0^e}\left(S_{ij}\dot{F}_{ij} + S\dot{\gamma}_\chi + M_i\dot{K}_i\right) dV_0 = \sum_{e=1}^{n_{surf}}\int_{\partial D_0^e}\left(T_i\dot{u}_i + M\dot{\gamma}_\chi\right) dS_0. \tag{95}$$

Here, the subdomain D_0^e corresponds to the space occupied by the individual element e. The summation is done for the repeated subscripts. The boundary ∂D_0 is discretized into n_{surf} surface elements ∂D_0^e for the application of surface tractions. In general, it is assumed that, within each individual element, u_i is interpolated from the displacement values of p nodes and γ_χ from the values of q nodes:

$$u_i = \sum_{a=1}^{p} {}^{u}N^a\tilde{u}_i^a, \qquad \gamma_\chi = \sum_{b=1}^{q} {}^{\chi}N^b\tilde{\gamma}_\chi^b, \tag{96}$$

in each element, where ${}^{u}N^a$ and ${}^{\chi}N^b$ are shape functions respectively for u_i and γ_χ, and $\tilde{u}_i^a$ and $\tilde{\gamma}_\chi^b$ respectively denote the nodal values of u_i at node a and those of γ_χ at node b. Unlike the subscripts, the summation operators are written explicitly for the superscripts denoting the node numbers. The deformation gradient F_{ij} and the Lagrangian gradient of microslip K_i are given by

$$F_{ij} = \sum_{a=1}^{p} {}^{u}B_j^a\tilde{u}_i^a, \qquad K_i = \sum_{b=1}^{q} {}^{\chi}B_i^b\tilde{\gamma}_\chi^b \tag{97}$$

with ${}^{u}B_j^a = \dfrac{\partial {}^{u}N^a}{\partial X_j}$ and ${}^{\chi}B_i^b = \dfrac{\partial {}^{\chi}N^b}{\partial X_i}$. Using these relations in Eq. (95) leads to

$$\begin{aligned}&\sum_{e=1}^{n}\int_{D_0^e}\left[S_{ij}\sum_{a=1}^{p}\left({}^{u}B_j^a\hat{\tilde{u}}_i^a\right) + \sum_{b=1}^{q}\left(S\,{}^{\chi}N^b\hat{\tilde{\gamma}}_\chi^b + M_i\,{}^{\chi}B_i^b\hat{\tilde{\gamma}}_\chi^b\right)\right] dV_0 \\ &= \sum_{e=1}^{n_{surf}}\int_{\partial D_0^e}\left(T_i\sum_{a=1}^{p}{}^{u}N^a\hat{\tilde{u}}_i^a + M\sum_{b=1}^{q}{}^{\chi}N^b\hat{\tilde{\gamma}}_\chi^b\right) dS_0\end{aligned} \tag{98}$$

$$\begin{aligned}&\Longrightarrow \sum_{e=1}^{n}\sum_{a=1}^{p}\left[\int_{D_0^e}\left(S_{ij}\,{}^{u}B_j^a\right) dV_0\right]\hat{\tilde{u}}_i^a + \sum_{e=1}^{n}\sum_{b=1}^{q}\left[\int_{D_0^e}\left(S\,{}^{\chi}N^b + M_i\,{}^{\chi}B_i^b\right) dV_0\right]\hat{\tilde{\gamma}}_\chi^b \\ &= \sum_{e=1}^{n_{surf}}\sum_{a=1}^{p}\left[\int_{\partial D_0^e}\left(T_i\,{}^{u}N^a\right) dS_0\right]\hat{\tilde{u}}_i^a + \sum_{e=1}^{n_{surf}}\sum_{b=1}^{q}\left[\int_{\partial D_0^e}\left(M\,{}^{\chi}N^b\right) dS_0\right]\hat{\tilde{\gamma}}_\chi^b.\end{aligned} \tag{99}$$

According to Eq. (99), an internal reaction is associated with each degree of freedom: $R^a_{\mathrm{int}(u_i,e)}$ is the internal reaction related to u_i at node a of element e and $R^b_{\mathrm{int}(\gamma_\chi,e)}$ is the internal reaction related to γ_χ at node b of element e

$$R^a_{\mathrm{int}(u_i,e)} = \int_{D_0^e}\left(S_{ij}\,{}^{u}B_j^a\right) dV_0, \qquad R^b_{\mathrm{int}(\gamma_\chi,e)} = \int_{D_0^e}\left(S\,{}^{\chi}N^b + M_i\,{}^{\chi}B_i^b\right) dV_0. \tag{100}$$

Analogously, an external reaction is associated with each degree of freedom:

$$R^a_{\mathrm{int}(u_i,e)} = \int_{D_0^e}\left(T_i\,{}^{u}N^a\right) dS_0, \qquad R^b_{\mathrm{ext}(\gamma_\chi,e)} = \int_{\partial D_0^e}\left(M\,{}^{\chi}N^b\right) dS_0. \tag{101}$$

With these expressions, (99) writes

$$\begin{aligned}&\sum_{e=1}^{n}\sum_{a=1}^{p}R^a_{\mathrm{int}(u_i,e)}\hat{\tilde{u}}_i^a + \sum_{e=1}^{n}\sum_{b=1}^{q}R^b_{\mathrm{int}(\gamma_\chi,e)}\hat{\tilde{\gamma}}_\chi^b = \sum_{e=1}^{n_{surf}}\sum_{a=1}^{p}R^a_{\mathrm{int}(u_i,e)}\hat{\tilde{u}}_i^a \\ &+ \sum_{e=1}^{n_{surf}}\sum_{b=1}^{q}R^b_{\mathrm{ext}(\gamma_\chi,e)}\hat{\tilde{\gamma}}_\chi^b.\end{aligned} \tag{102}$$

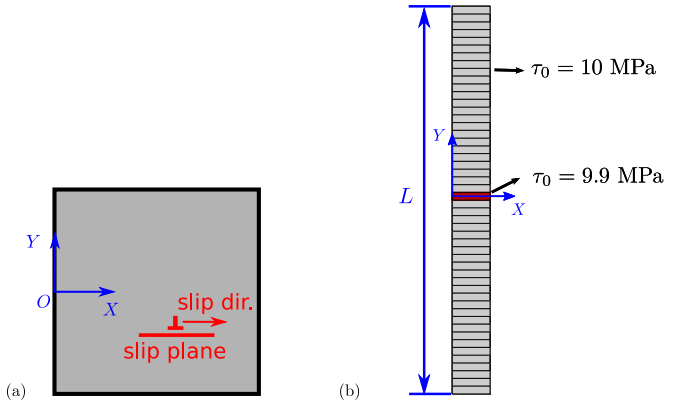

Fig. 2. 2D single crystal with a single slip system: (a) Geometry and associated 2D coordinate system, (b) FE mesh of a strip with a central defect.

This equation is solved using Newton's method. The details of the numerical implementation model are given in Appendix C and Appendix D.

In the following simulations, quadratic (resp. linear) interpolation functions are used for the displacement (resp. microslip) degrees of freedom.

5. Application to strain localization in single crystals

Strong strain gradients arise in particular in the presence of localization phenomena. Such a situation involving strain softening is investigated in this section using the proposed micromorphic model. First, an analytical solution for slip band formation under simple shear loading is worked out in order to validate the FE implementation. Then, the finite element method is applied to slip/kink banding in a single crystal plate subjected to simple tension.

5.1. Simple glide test with slip band localization

Analytical solution

Slip band formation is investigated within the framework of finite strains in 2D. The analysis is inspired by the work of Gurtin (2000); Forest et al. (2005). The single crystal is endowed with one single slip system as shown in Fig. 2(a). The slip direction $\underline{\boldsymbol{\ell}}$ and the normal to the slip plane $\underline{\boldsymbol{n}}$ are

$$\underline{\boldsymbol{\ell}} = (1,\ 0), \quad \underline{\boldsymbol{n}} = (0,\ 1). \tag{103}$$

The single crystal is subjected to the kinematics of simple glide in the form:

$$\underline{\boldsymbol{x}} = \underline{\boldsymbol{X}} + u(Y)\underline{\boldsymbol{\ell}} \tag{104}$$

where the displacement $u(Y)$ of the material point in the direction of slip is taken as a function of coordinate Y, see Fig. 2(a). Thus, the deformation gradient $\underset{\sim}{\mathbf{F}}$ takes the form

$$\underset{\sim}{\mathbf{F}} = \underset{\sim}{\mathbf{1}} + \kappa \underline{\boldsymbol{\ell}} \otimes \underline{\boldsymbol{n}}, \tag{105}$$

where $\kappa = \dfrac{\partial u}{\partial Y}$. The plastic deformation rate is

$$\dot{\underset{\sim}{\mathbf{P}}} \cdot \underset{\sim}{\mathbf{P}}^{-1} = \underset{\sim}{\mathbf{1}} + \dot{\gamma} \underline{\boldsymbol{\ell}} \otimes \underline{\boldsymbol{n}}, \tag{106}$$

with $\gamma = \gamma(Y)$. In the absence of lattice rotation with respect to the coordinate frame, this equation can be integrated into: $\underset{\sim}{\mathbf{P}} = \underset{\sim}{\mathbf{1}} + \gamma \underline{\boldsymbol{\ell}} \otimes \underline{\boldsymbol{n}}$. Since $\underset{\sim}{\mathbf{F}} = \underset{\sim}{\mathbf{E}}.\underset{\sim}{\mathbf{P}}$, one obtains

$$\underset{\sim}{\mathbf{E}} = \underset{\sim}{\mathbf{1}} + \kappa^e \underline{\boldsymbol{\ell}} \otimes \underline{\boldsymbol{n}} \tag{107}$$

with $\kappa^e(Y) = \kappa(Y) - \gamma(Y)$. Assuming small elastic strains, i.e., $\kappa^e \ll 1$, leads to

$$\underset{\sim}{\mathbf{C}}^e = \underset{\sim}{\mathbf{E}}^T \cdot \underset{\sim}{\mathbf{E}} \approx \underset{\sim}{\mathbf{1}} + \kappa^e(\underline{\boldsymbol{\ell}} \otimes \underline{\boldsymbol{n}} + \underline{\boldsymbol{n}} \otimes \underline{\boldsymbol{\ell}}). \tag{108}$$

with the following consequences for the Green-Lagrange elastic tensor, $\underset{\sim}{\mathbf{E}}^e_{GL}$, the Mandel stress, $\underset{\sim}{\boldsymbol{\Pi}}^M$, and the resolved shear stress τ:

$$\underset{\sim}{\mathbf{E}}^e_{GL} \approx \frac{1}{2}\kappa^e(\underline{\boldsymbol{\ell}} \otimes \underline{\boldsymbol{n}} + \underline{\boldsymbol{n}} \otimes \underline{\boldsymbol{\ell}}), \quad \underset{\sim}{\boldsymbol{\Pi}}^M = \underset{\sim}{\mathbf{C}}^e.\underset{\sim}{\boldsymbol{\Pi}}^e \approx \underset{\sim}{\boldsymbol{\Pi}}^e,$$
$$\tau \approx \underset{\sim}{\boldsymbol{\Pi}}^e : (\underline{\boldsymbol{\ell}} \otimes \underline{\boldsymbol{n}}). \tag{109}$$

The Piola stress expressed in the intermediate configuration and the Boussinesq stress are then computed as

$$\underset{\sim}{\boldsymbol{\Pi}}^e = \tau(\underline{\boldsymbol{\ell}} \otimes \underline{\boldsymbol{n}} + \underline{\boldsymbol{n}} \otimes \underline{\boldsymbol{\ell}}), \quad \underset{\sim}{\mathbf{S}} = J\underset{\sim}{\mathbf{C}}.\underset{\sim}{\mathbf{F}}^{-T} = \underset{\sim}{\mathbf{E}}.\underset{\sim}{\boldsymbol{\Pi}}^e.\underset{\sim}{\mathbf{P}}^{-T} \approx \underset{\sim}{\boldsymbol{\Pi}}^e.\underset{\sim}{\mathbf{P}}^{-T}$$
$$= \underset{\sim}{\boldsymbol{\Pi}}^e - \tau\gamma \underline{\boldsymbol{\ell}} \otimes \underline{\boldsymbol{\ell}}, \tag{110}$$

with $\tau = \mu\kappa^e$, and μ is the shear modulus in the case of isotropic elasticity. The equilibrium condition, $\mathrm{Div}\,\underset{\sim}{\mathbf{S}} = 0$ (see Eq. (12)) in the absence of body forces, implies that

$$\frac{\partial \tau}{\partial Y} = 0, \tag{111}$$

so that the resolved shear stress is uniform: $\tau = \overline{\tau}$. The following linear softening law is considered:

$$\tau_c = \tau_0 + H\gamma, \quad \text{with} \quad H < 0. \tag{112}$$

The derivation is carried out first for the formulation presented in Section 2.3. The free energy potential given by Eq. (49) is chosen so that the following constitutive equations hold:

$$\underline{\boldsymbol{K}} = A\underline{\boldsymbol{M}}, \quad S = -H_\chi e. \tag{113}$$

The yield condition (Eq. 34) writes

$$f = |\tau| - (\tau_c - S) = |\tau| - \left[\tau_0 + H\gamma - H_\chi(\gamma_\chi - \gamma)\right] = 0, \tag{114}$$

from which the amount of slip γ can be derived as

$$\gamma = \frac{|\tau| - \tau_0 + H_\chi\gamma_\chi}{H + H_\chi}. \tag{115}$$

The divergence of the generalized stress vector is then computed after taking Eq. (113) into account:

$$\mathrm{Div}\,\underline{\boldsymbol{M}} = A\mathrm{Div}\,\underline{\boldsymbol{K}} = A\mathrm{Div}\left(\frac{\partial \gamma_\chi}{\partial X}\underline{\boldsymbol{\ell}} + \frac{\partial \gamma_\chi}{\partial Y}\underline{\boldsymbol{n}}\right) = A\frac{\partial^2 \gamma_\chi}{\partial Y^2}. \tag{116}$$

Combining the balance equation Eq. (12) with the previous equation and Eq. (113) leads to

$$A\frac{\partial^2 \gamma_\chi}{\partial Y^2} = H_\chi(\gamma_\chi - \gamma). \tag{117}$$

Substituting Eq. (115) into the previous equation, the differential equation governing the microslip is obtained:

$$A\frac{\partial^2 \gamma_\chi}{\partial Y^2} - \frac{HH_\chi}{H + H_\chi}\gamma_\chi + \frac{H_\chi}{H + H_\chi}(|\tau| - \tau_0) = 0. \tag{118}$$

A trivial uniform solution of Eq. (118) is: $\gamma_\chi = (|\overline{\tau}| - \tau_0)/H$, which results in a spatially uniform shear strain. As H is negative, a general sinusoidal solution Eq. (118) exists in the form:

$$\gamma_\chi = C_1 \sin\left(\frac{2\pi}{\lambda_c}Y\right) + C_2 \cos\left(\frac{2\pi}{\lambda_c}Y\right) + \frac{|\overline{\tau}| - \tau_0}{H}, \tag{119}$$

with the integration constants C_1 and C_2, and the wave length

$$\lambda_c = 2\pi\left(\frac{A(H_\chi + H)}{H_\chi|H|}\right)^{1/2}. \tag{120}$$

This formula requires that $H + H_\chi > 0$. Note that λ_c comes into play as a material length scale. Within one period, γ_χ increases to its maximum value and then decreases, which represents slip band localisation. Since a large value is usually taken for the penalty parameter H_χ so that $H_\chi \gg |H|$, $\lambda_c \sim \sqrt{A/|H|}$. Thus, increasing the value of A results in a wider shear band. Other solutions can be proposed with isolated or periodically distributed slip bands separated by zones of elastic unloading.

Analysis with the alternative formulation

The analytical solution is now derived for the second formulation of the theory presented in Section 2.4, including microslip gradient induced kinematic hardening. The free energy potential given by Eq. (49) is considered leading to the constitutive equations Eq. (113). The yield function (Eq. 45) writes

$$f = |\tau + (\underline{\boldsymbol{K}}^{\sharp} \cdot \underline{\ell})(\underline{\boldsymbol{M}}^{\sharp} \cdot \underline{\boldsymbol{n}})| - \left[\tau_0 + H\gamma - H_\chi(\gamma_\chi - \gamma)\right]. \tag{121}$$

with

$$\underline{\boldsymbol{K}}^{\sharp} = \frac{\partial \gamma_\chi}{\partial X}\underline{\ell} + \left(\frac{\partial \gamma_\chi}{\partial Y} - \gamma\frac{\partial \gamma_\chi}{\partial X}\right)\underline{\boldsymbol{n}},$$
$$\underline{\boldsymbol{M}}^{\sharp} = A\left[\left(\frac{\partial \gamma_\chi}{\partial X} + \gamma\frac{\partial \gamma_\chi}{\partial Y}\right)\underline{\ell} + \frac{\partial \gamma_\chi}{\partial Y}\underline{\boldsymbol{n}}\right]. \tag{122}$$

The kinematic hardening variable is computed as

$$x^r = -(\underline{\boldsymbol{K}}^{\sharp} \cdot \underline{\ell})(\underline{\boldsymbol{M}}^{\sharp} \cdot \underline{\boldsymbol{n}}) = -A\frac{\partial \gamma_\chi}{\partial X}\frac{\partial \gamma_\chi}{\partial Y}. \tag{123}$$

It can exist only in the presence of a gradient of slip in both directions X and Y. Since $\gamma_\chi = \gamma_\chi(Y)$ is assumed in the present example, $\frac{\partial \gamma_\chi}{\partial X} = 0$ so that kinematic hardening, x^r, vanishes. Thus, the yield function takes the same form as Eq. (114).

As the balance laws Eq. (12) hold for the two formulations, the same differential equation governing γ_χ as Eq. (118) is obtained. It means that the two formulations lead to the same solution for the special case considered in this section. However, it is important to notice that the term $A\frac{\partial \gamma_\chi}{\partial X}\frac{\partial \gamma_\chi}{\partial Y}$ in Eq. (121) will come into play for the case with $\frac{\partial \gamma_\chi}{\partial X} \neq 0$ in shear bands, e.g. when pile-ups are considered.

FE solution

For the finite element (FE) analysis, a single row of elements with side length $L = 1$ mm is considered and shown in Fig. 2(b). Periodic boundary conditions are applied for the displacement field $\underline{\boldsymbol{u}}$ such that

$$\underline{\boldsymbol{u}} = \overline{\mathbf{F}} \cdot \underline{\boldsymbol{X}} + \underline{\boldsymbol{v}} \tag{124}$$

where $\overline{\mathbf{F}}$ denotes the overall deformation gradient and $\underline{\boldsymbol{v}}$ a periodic fluctuation vector. The periodicity conditions are also prescribed to the γ_χ field, i.e., γ_χ takes the same value at homologous points on the opposite sides of the strip, and generalized tractions are opposite. Simple glide is imposed by prescribing the overall deformation gradient component $\overline{F}_{12}$ and vanishing remaining components.

As for the material parameters, the softening parameter is fixed to be $H = -10^3$ MPa, the shear modulus $\mu = 105$ GPa, and $\tau_0 = 10$ MPa. The viscosity parameters are chosen as $K = 0.1$ MPa and $n = 15$ so that the rate–sensitivity is negligible for the considered strain rates. Note that, in order to trigger the localization, the value of τ_0 in Eq. (112) is set to $\tau_0 = 9.9$ MPa in a central element, as indicated in Fig. 2(b).

The effect of the penalty parameter H_χ is first studied. To this end, the higher order modulus is fixed to be $A = 5$ N, and the value of H_χ is changed from 10^3 to 10^6 MPa. The overall stress-strain response and the distribution of γ_χ along axis Y at the shear strain $\overline{F}_{12} = 0.0005$ are shown in Fig. 3. As can be seen, the overall stress–strain curves and the distribution of γ_χ converge to the same results with increasing H_χ. However, when H_χ is too small, i.e., $H_\chi = 10^3$ MPa, a completely different solution of γ_χ is found. These results confirm the penalty role of the parameter H_χ and shows the necessity of choosing a large value for H_χ if the objective is to obtain the strain gradient limit model. However, a too large value of H_χ will cause numerical problems due to ill–conditioned matrices.

The effect of A is then investigated by fixing $H_\chi = 10^5$ MPa and varying A from 0.1 to 5 N. The stress-strain curves and γ_χ as a function of Y at the overall shear strain $\overline{F}_{12} = 0.0005$ are presented in Fig. 4. The results show the regularization of the shear band, i.e., its finite width. The width of the band increases with increasing value of A, which is in good agreement with the analytical solution (cf. the material length scale λ_c of Eq. (120)). It can also be observed in Fig. 4a that the hardening due to slip gradient is larger with a large value of A, which counteracts the softening due to the term $H\gamma$ with $H < 0$ in Eq. (114).

In order to obtain the analytical solution for this problem, the integration constants in Eq. (119) must be identified from suitable boundary conditions. The solution corresponds to a slip band surrounded by elastic zones within which $\gamma_\chi = 0$. At the interface between the elastic and the plastic region, continuity requirements are imposed for the microslip variable and the generalized traction. These conditions amount to $\gamma_\chi = 0$ and $\frac{\partial \gamma_\chi}{\partial Y} = 0$ at the boundaries of the sinus branch. The analytical solution obtained for $A = 5$ N and $H_\chi = 10^5$ MPa is compared with the numerical result in Fig. 5 at the shear strain $\overline{F}_{12} = 0.002$. It shows a perfect agreement between the FE and the analytical solutions.

5.2. Strain localization under uniaxial tension

Strain localization in single crystals has been observed in many studies (see, e.g., Chang and Asaro, 1981). It was analyzed in the seminal work of Asaro and Rice (1977) by considering crystals undergoing single slip. The problem was then investigated by Peirce et al. (1982b) using FE simulations for double slip. In this section, strain localization in tension is simulated for single crystals endowed with a single slip system, using FE simulations with the micromorphic model. The formation of slip and kink bands is expected in the simulations according to Asaro and Rice's bifurcation analysis. Their formation has been investigated in different works (see Forest (1998) for analysis and simulations, and Kysar and Briant (2002); Flouriot et al. (2003); Sabnis et al. (2012) for experimental observations of slip and kink bands at the crack tip or at notches). Mesh dependence of the simulations of slip and kink bands is studied in the following.

Problem setup

Simulations are performed with the single crystal plate shown in Fig. 6. The plate is meshed by brick elements with reduced integration (20 nodes for the displacement DOFs and 8 nodes for the microslip DOF) and one element is used in the thickness direction. The width of the plate is the same for all meshes and equal to 1 mm. An in-plane single slip system is defined, which means that the slip direction and the normal to the slip plane are both contained in the plane of the plate. This results in plane plastic strain conditions. The slip direction makes an angle of 56.3° with respect to the vertical direction. The following clamping boundary conditions are enforced:

$$U_X(Y = 0) = 0, \quad U_Y(Y = 0) = 0, \quad U_X(Y = L_0) = 0,$$
$$U_Y(Y = L_0) = U(t). \tag{125}$$

The four lateral faces of the plate are traction free leading to plane stress conditions. Additional conditions are enforced to fix the rigid body motion.

The simulations are performed with both the conventional and micromorphic models. Isotropic elasticity is considered. A linear hardening law is introduced with τ_c given by:

$$\tau_c = \tau_0 + H\gamma \tag{126}$$

with $H > 0$, in contrast to the previous section. For the simulations, a weak hardening is considered with $H = 1MPa$. For the micromor-

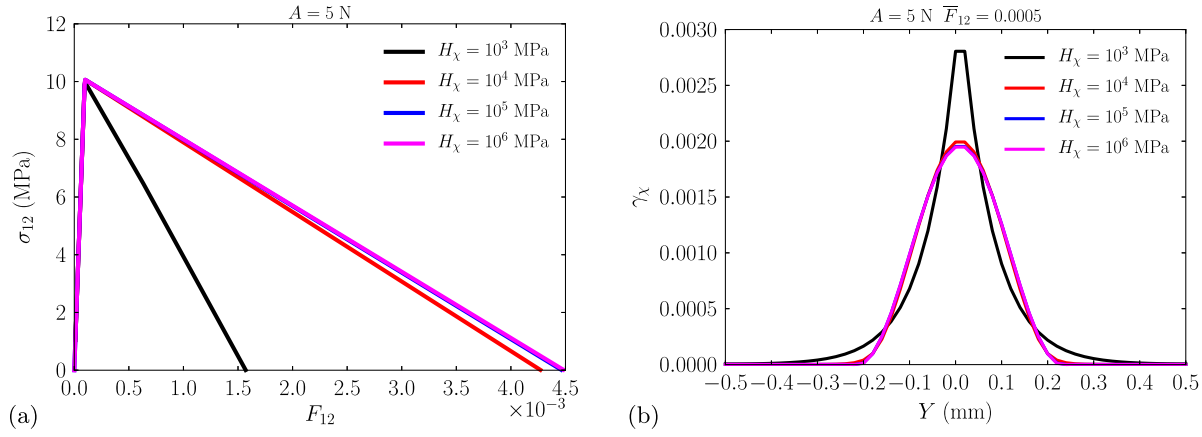

Fig. 3. Influence of H_χ on (a) overall stress-strain curve and (b) distribution of γ_χ along Y direction at $\overline{F}_{12} = 0.0005$. $A = 5$ N.

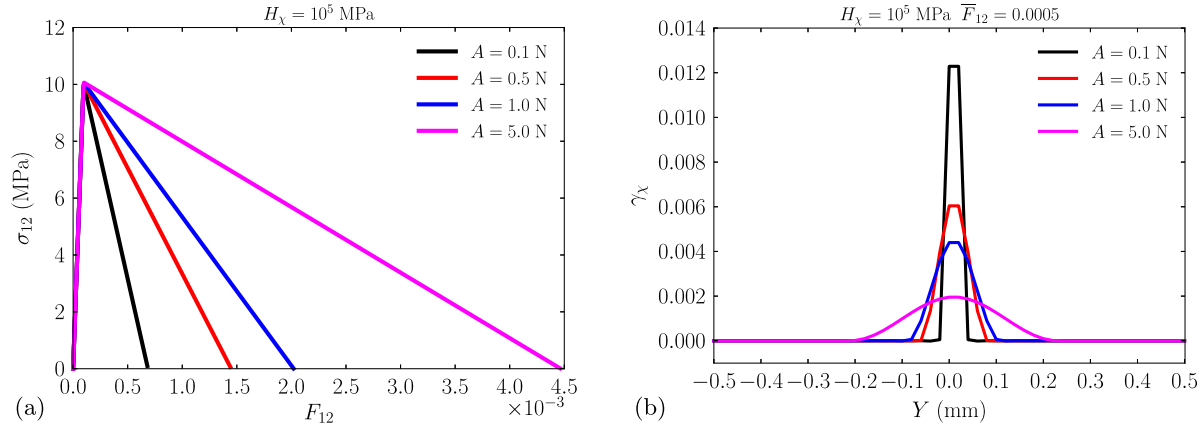

Fig. 4. Influence of A on (a) overall stress-strain curve and (b) distribution of γ_χ along Y direction at $\overline{F}_{12} = 0.0005$.

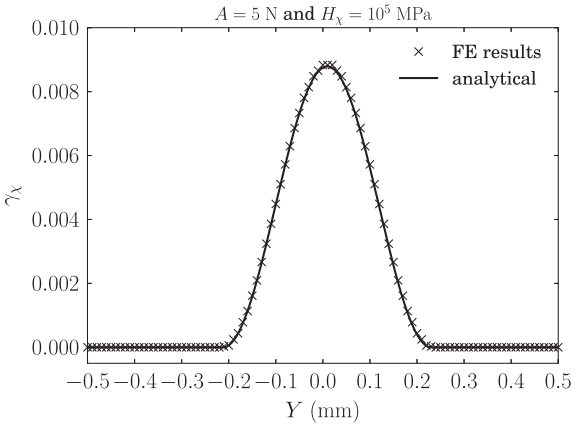

Fig. 5. Comparison analytical and numerical results: Distribution of γ_χ along Y direction at $\overline{F}_{12} = 0.002$.

phic model, $H_\chi = 5 \times 10^4$MPa and $A = 0.1N$ are adopted. Strain localization will occur in the plate under tension due to geometrical softening induced by cross–section reduction and lattice rotation.

Results

Different FE discretizations are considered with n elements for the width and $6n$ for the height, i.e., $6n^2$ elements. Four meshes with respectively $n = 8, 16, 24, 32,$ are considered (see Fig. 6 for a mesh with $n = 8$).

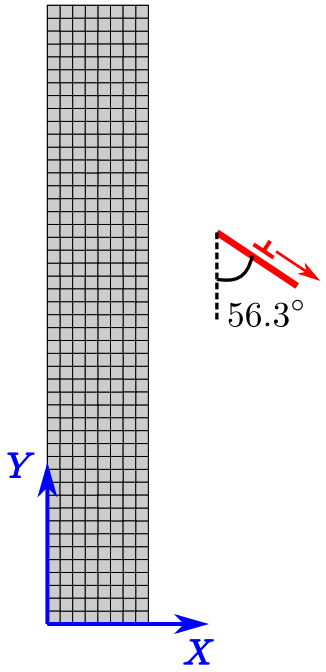

Fig. 6. A typical FE mesh for simulations of strain localization in uniaxial tension. The total number of cubic elements used is $n \times 6n$ with n for the width and $6n$ for the height ($n = 8$ in the figure). An in-plane single slip system is also shown, whose slip direction makes an angle of 56.3° with respect to the vertical direction.

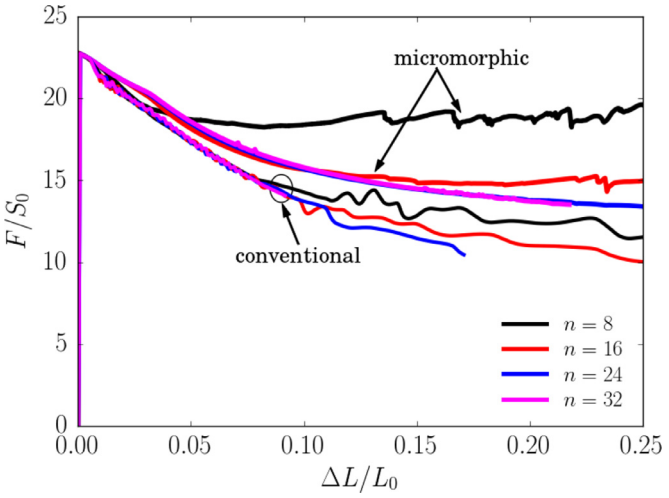

Fig. 7. Stress–strain curves obtained by the conventional and micromorphic crystal plasticity with various FE meshes. The four upper (resp. lower) curves correspond to the micromorphic (resp. conventional) model responses.

The evolution of the loading force F normalized by initial section area S_0 is plotted in Fig. 7 as a function of the elongation $\Delta L = U(t)$ (in the direction Y axis) normalized by the initial height L_0 of the mesh. For the simulations with the conventional model, it is found that the loading curves display oscillations. A mesh dependence of the curves is also observed. As the FE mesh is refined to $n = 32$, the simulation diverges at $\Delta L/L_0 = 0.1$ as a result of strong strain localization.

For the simulations with the micromorphic model, a softening regime is also observed. However, the stress level is higher than that obtained by the conventional model. This results from the strain gradient hardening included in the micromorphic model. Mesh convergence is observed for the micromorphic model as soon as a sufficiently high number of elements is used. Moreover, the curves obtained by the micromorphic model with $n = 24$ and $n = 32$ are smoother than those obtained by the conventional model. They do not display spurious oscillations.

The evolution of the plastic slip γ field with $\Delta L/L_0$ is shown in Fig. 8 for the conventional model and in Fig. 9 for the micromorphic model. Complex localization modes are observed in the simulations. Both models predict the formation of two kink bands at the beginning of the loading, that are indeed perpendicular to the slip direction shown by Fig. 6. As straining increases, strain localizes in the kink band located in the lower part of the crystal. Finally, intense slip bands form crossing the initial kink bands, leading to final necking of the plate.

Some differences can be noted between both simulations. Compared with the conventional model results, the distance between the two kink bands predicted by the micromorphic model is smaller. Besides, the band width (band size along Y direction) predicted by the micromorphic model is larger than for the conventional model, i.e., the plastic slip field is more diffuse in the simulation with the micromorphic model. The band width predicted by the micromorphic model can be compared to the characteristic length of the model appearing in Eq. (118). In the case of a positive hardening parameter H, solutions are exponential functions with the characteristic length:

$$\lambda_c = \sqrt{\frac{A(H_\chi + H)}{H_\chi H}}, \quad \text{and} \quad \lambda_c^\infty = \sqrt{\frac{A}{H}}, \tag{127}$$

where λ_c^∞ is the limit of λ_c for large values of H_χ. However, this is only an estimate since the analytical solution of slip banding in tension and necking at large deformations is not available. In the present case, $\lambda_c^\infty = 0.32$ mm, i.e. one third of the plate width. This represents indeed a good estimate of the kink band width in Fig. 9 for $\Delta L/L_0 = 0.017$, and an underestimate of the competing slip banding/necking zone at $\Delta L/L_0 = 0.25$. The element size (about 0.04 mm for $n = 24$ and about 0.03 mm for $n = 32$) is almost 10 times smaller than the characteristic length, as it should be to ensure mesh convergence.

An essential difference between slip and kink bands is that the latter involve a lot of lattice rotation and lattice curvature in contrast to the former. The polar decomposition of the elastic part of deformation gradient $\underset{\sim}{\mathbf{F}}$ is $\underset{\sim}{\mathbf{F}} = \underset{\sim}{\mathbf{R}}^e \cdot \underset{\sim}{\mathbf{U}}^e$, with the rotation tensor $\underset{\sim}{\mathbf{R}}^e$ and the right stretch tensor $\underset{\sim}{\mathbf{U}}^e$. Neglecting the small elastic distortion $\underset{\sim}{\mathbf{U}}^e$, $\underset{\sim}{\mathbf{R}}^e$ can be interpreted as the lattice rotation. The corresponding rotation angle θ is given by

$$\theta = \arccos \frac{1}{2}(\text{trace}\, \underset{\sim}{\mathbf{R}}^e - 1). \tag{128}$$

The field of θ is shown in Fig. 10 for the simulation with the conventional model. The formation of the kink bands is accompanied with relatively high level of θ within the bands. In contrast, the formation of a slip band crossing the kink band at $\Delta L/L_0 = 0.025$ induces a lot of plastic slip but no further lattice rotation. The same observations can be made for the micromorphic simulations as shown in Fig. 11.

5.3. Discussion

The previous simulations show that the micromorphic model enables mesh–independent simulation of slip and kink banding in contrast to conventional crystal plasticity. The use of a Cosserat crystal plasticity model, or, equivalently, of a strain gradient plasticity model based on the dislocation density tensor, only regularize the formation of kink bands, see (Forest, 1998), because only lattice curvature triggers size effects in such models. The question arises of the physical meaning of such a regularization. It is well-known that the multiplication of so–called geometrically necessary dislocations (GND) corresponding to a gradient of slip γ along the slip direction, as it occurs during pile–up formation, is the origin of a size–dependent crystal plasticity behaviour, see, e.g., (Geers et al., 2013). In contrast, the gradient of slip in the direction normal to the slip plane does not correspond to GNDs. In strain gradient crystal plasticity based on the dislocation density tensor, no size effect is predicted for the development of such normal slip gradients. In the physical reality, intense slip bands are not one atomic plane thick. Dislocation entanglement and cross–slip lead to finite width slip lines that are not predicted by GND–based crystal plasticity models. The thicknesses of kink and slip bands are different, slip bands being expected to be thinner than kink bands although no detailed analysis of such characteristics is available in the literature.

The *microslip* gradient model predicts a size–dependent behaviour of both slip and kink bands. A limitation of this model is that the same characteristic length is responsible for both effects. More elaborate models are necessary to account for the actual anisotropic size–dependent behaviour. We retain from this analysis that a computational advantage of the proposed approach is that it regularizes all plastic strain localization modes in contrast to available GND–based models.

6. Application to ductile fracture of single crystals

Void growth and coalescence are known as the mechanisms controlling ductile fracture in metallic materials. In single crystals, lattice orientation has been shown to have an impact on void growth and coalescence (cf. Ling et al. (2016) and references

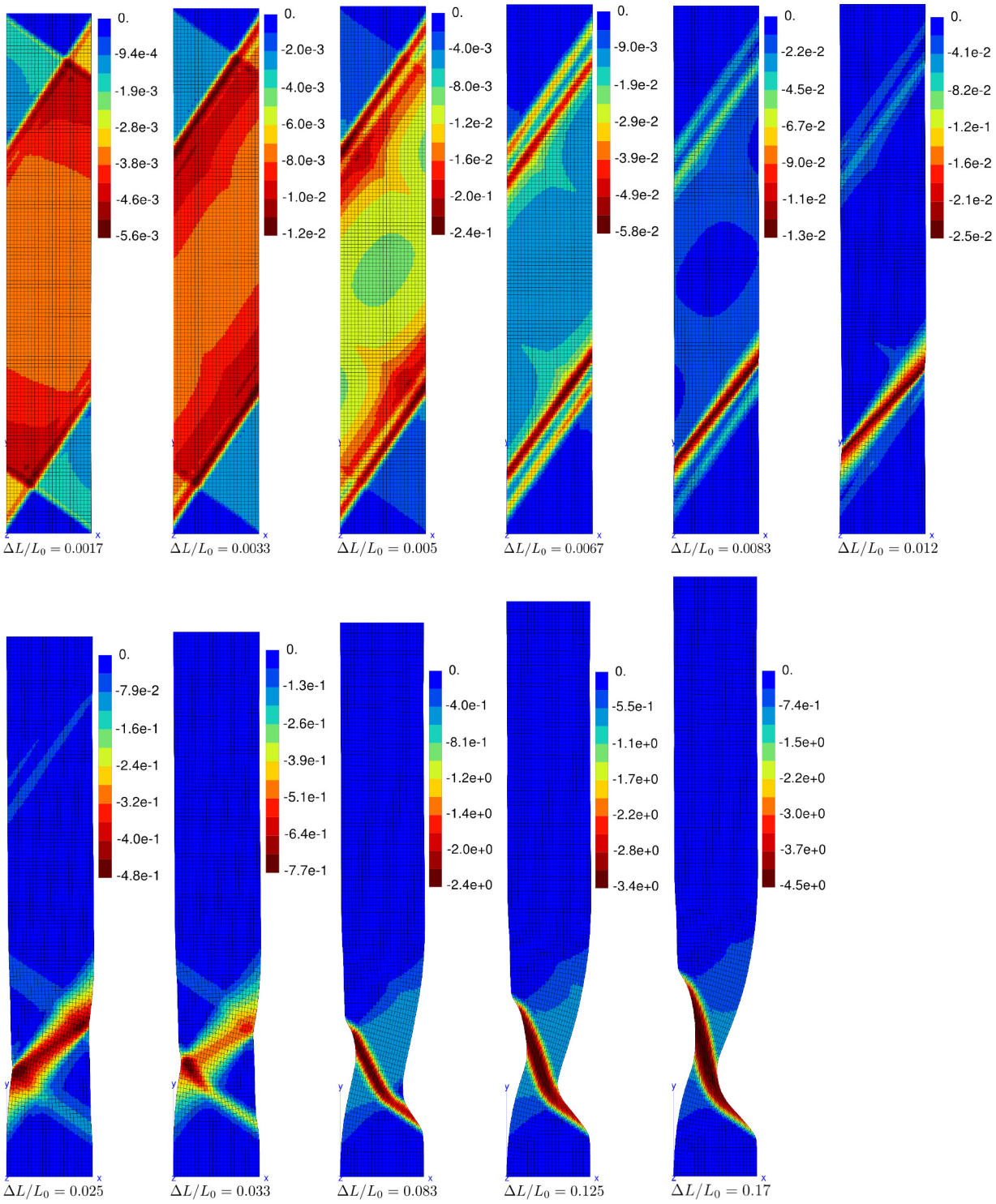

Fig. 8. Evolution of the plastic slip γ field with $\Delta L/L_0$ predicted by the conventional model with the FE mesh $n = 24$.

therein). As void size decreases to micro-scale, size effects are expected in single crystals, which have been predicted by different approaches (e.g., see Shu, 1998; Borg and Kysar, 2007 and Borg et al. (2008) for FE unit cell simulations with strain gradient plasticity, see Hussein et al. (2008) and Chang et al. (2015) for dislocation dynamics simulations, and see Zhao et al. (2009) for molecular dynamics simulations). In this section, unit cell simulations are carried out with the micromorphic model in order to predict size effects on void growth and coalescence in single crystals. Two cases are considered: a cylindrical void in a plate and a spherical void in a cube.

6.1. Unit cell simulations

A cylindrical void of radius R_0 in a square plate of side length L_0 is first considered. A typical FE mesh with one element in thickness w_0 is shown in Fig. 12a for an initial void volume fraction $f_0 = \pi R_0^2/L_0^2 = 0.1$. A biaxial tensile loading is imposed under plane strain conditions. The boundary conditions applied to the faces of

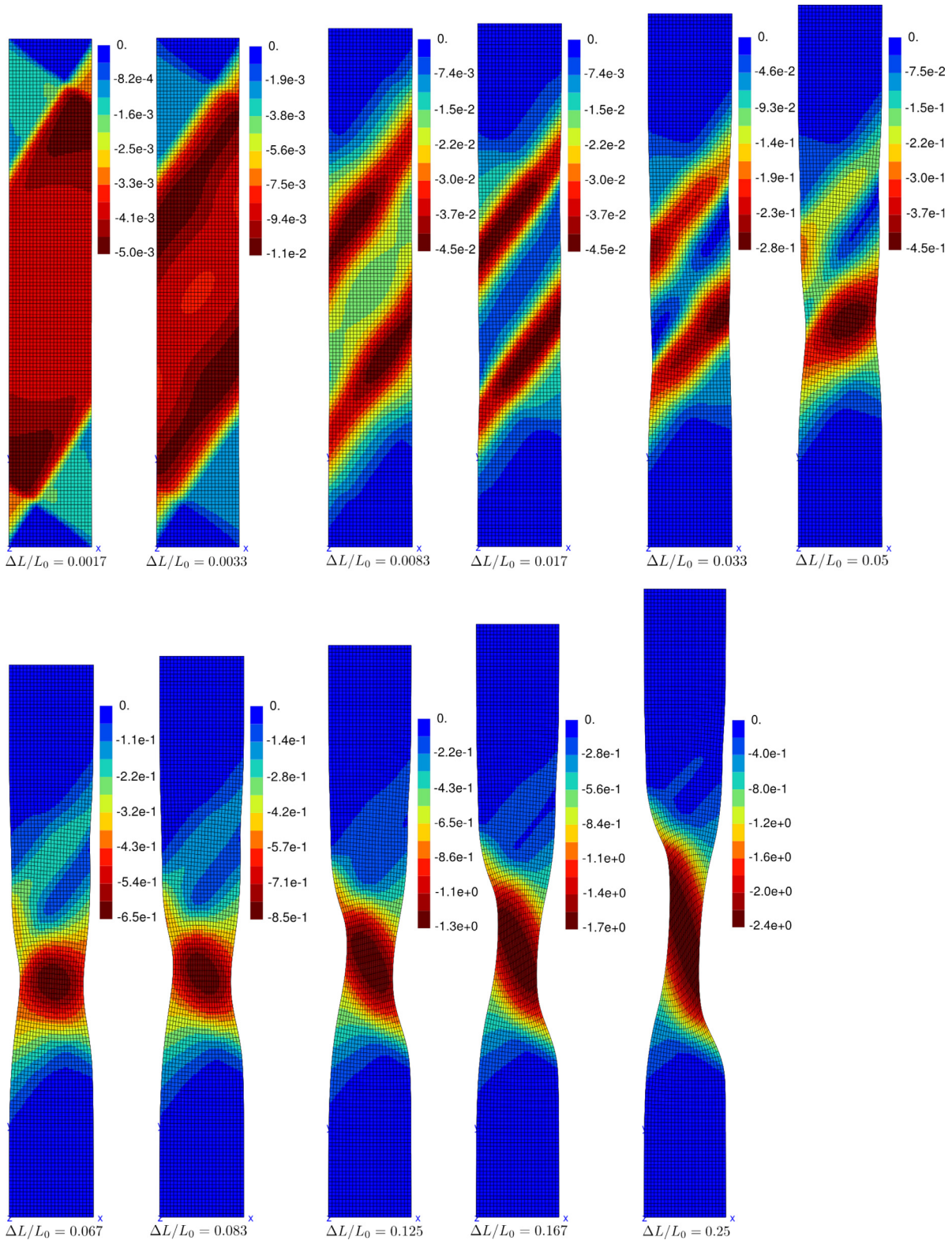

Fig. 9. Evolution of plastic slip γ field with $\Delta L/L_0$ predicted by the micromorphic model with the FE mesh $n = 24$.

the unit cell are

$$U_X(X=0)=0,\ U_X(X=L_0)=U_1(t), \tag{129}$$

$$U_Y(Y=0)=0,\ U_Y(Y=L_0)=U_2(t), \tag{130}$$

$$U_Z(Z=0)=0,\ U_Z(Z=w_0)=0. \tag{131}$$

Two external forces F_1 and F_2 are associated with $U_1(t)$ and $U_2(t)$. The prescribed U_2 is adjusted using a special additional finite element for keeping a constant biaxiality ratio $a=\overline{\sigma}_{22}/\overline{\sigma}_{11}=0.625$

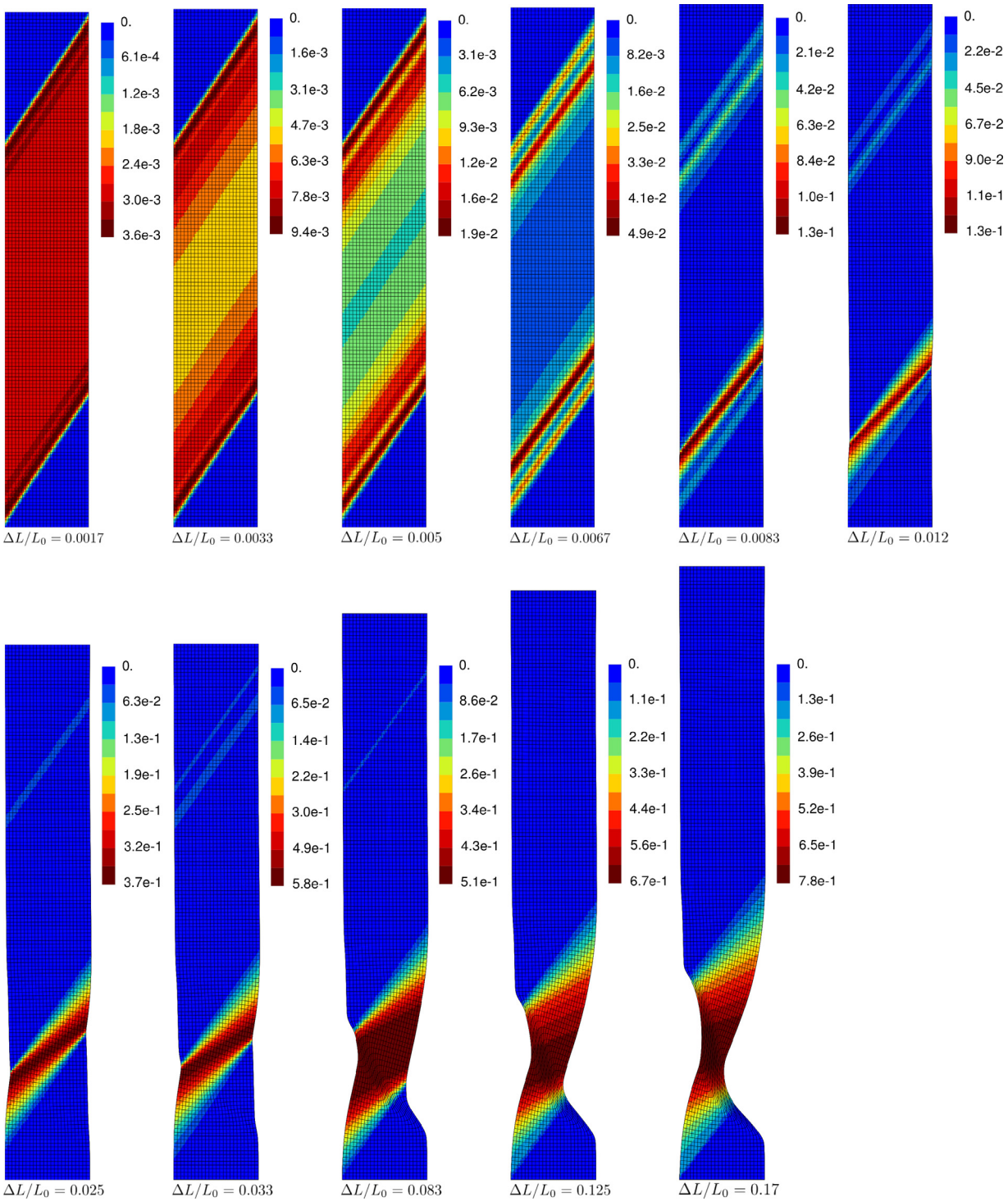

Fig. 10. The lattice rotation angle θ (rad.) field predicted by the conventional model for increading values $\Delta L/L_0$ with the FE mesh $n = 24$.

during the loading[1], where the overall (average) Cauchy stresses $\overline{\sigma}_{11}$ and $\overline{\sigma}_{22}$ are defined by

$$\overline{\sigma}_{11} = \frac{F_1}{w_0(L_0+U_2)}, \quad \overline{\sigma}_{22} = \frac{F_2}{w_0(L_0+U_1)}. \tag{132}$$

A spherical void in the center of a cube is then considered (see Fig. 12b), whose initial void volume fraction is $f_0 = \frac{4}{3}\pi\frac{R_0^3}{L_0^3}$. A triaxial axisymmetric loading is subscribed with the boundary conditions:

$$U_X(X=0) = 0, \; U_X(X=L_0) = U_1(t), \tag{133}$$

$$U_Y(Y=0) = 0, \; U_Y(Y=L_0) = U_2(t), \tag{134}$$

[1] Note that only one value of biaxiality (and of triaxiality in the next section) is considered. For the sake of brevity, the discussion of biaxiality (resp. triaxiality) effects on the growth and coalescence of cylindrical (resp. spherical) pores is postponed to another study. Such a discussion of triaxiality effects for spherical holes in single crystals can be found in (Ling et al., 2016) in the case of conventional crystal plasticity.

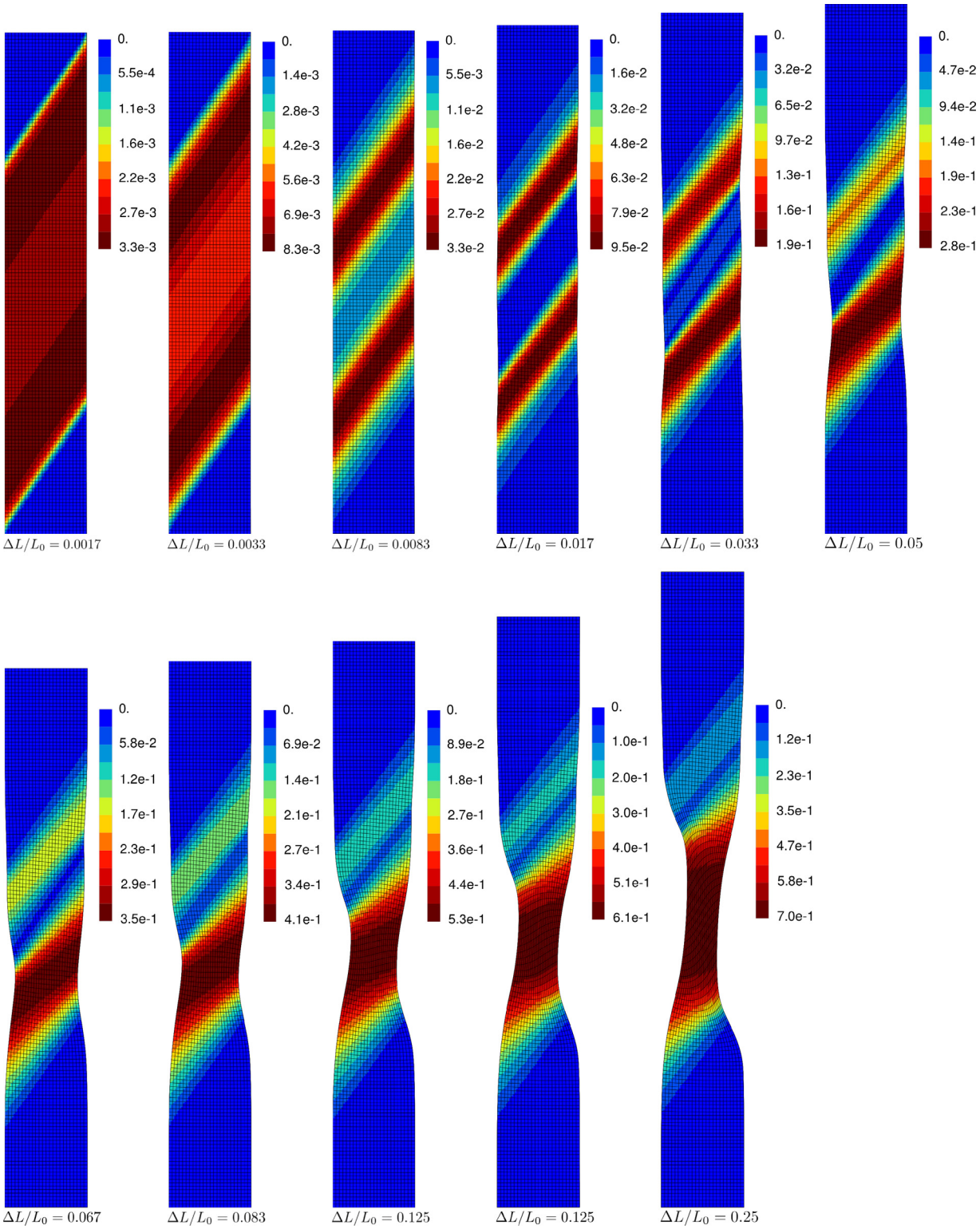

Fig. 11. The lattice rotation angle θ (rad.) field predicted by the micromorphic model for increasing values of $\Delta L/L_0$ with the FE mesh $n = 24$.

$$U_Z(Z=0)=0,\ U_Z(Z=L_0)=U_3(t)=U_2(t). \tag{135}$$

Three external forces F_1, F_2 and F_3 are respectively associated with $U_1(t)$, $U_2(t)$ and $U_3(t)$. The overall stresses $\overline{\sigma}_{11}$, $\overline{\sigma}_{22}$ and $\overline{\sigma}_{33}$ are defined by

$$\overline{\sigma}_{11}=\frac{F_1}{(L_0+U_2)(L_0+U_3)},\quad \overline{\sigma}_{22}=\frac{F_2}{(L_0+U_1)(L_0+U_3)},$$
$$\overline{\sigma}_{33}=\frac{F_3}{(L_0+U_1)(L_0+U_2)}. \tag{136}$$

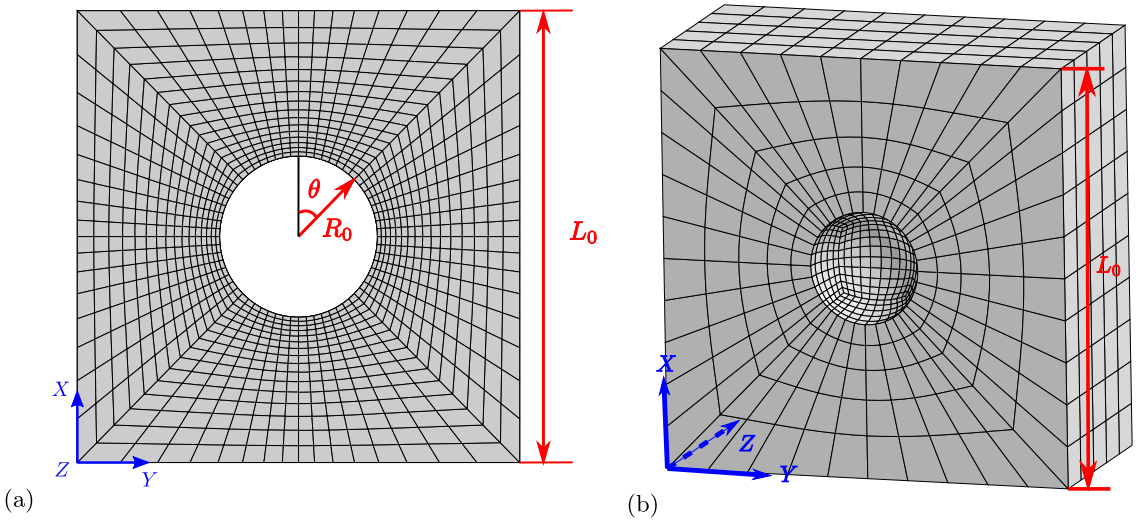

Fig. 12. Typical FE meshes for the unit cell simulations: (a) A cylindrical void in a plate ($f_0 = 0.1$) (b) a spherical void in a cube (half of the mesh is shown and $f_0 = 0.01$).

Table 2
Slip systems in FCC single crystals.

s	1	2	3	4	5	6	7	8	9	10	11	12
$\underline{\boldsymbol{n}}^r$		(111)			(1$\bar{1}$1)			($\bar{1}$11)			($\bar{1}\bar{1}$1)	
$\underline{\ell}^r$	[$\bar{1}$01]	[0$\bar{1}$1]	[$\bar{1}$10]	[$\bar{1}$01]	[011]	[110]	[0$\bar{1}$1]	[110]	[101]	[$\bar{1}$10]	[101]	[011]

Table 3
Material parameters for the unit cell simulations (see Han et al. (2013)).

C_{11}	C_{12}	C_{44}	τ_0	n	σ_0, $\dot{\gamma}_0$	μ	G_c	κ
199 GPa	136 GPa	105 GPa	88 MPa	15	1 MPa, 1 s^{-1}	65.6 GPa	10.4	42.8
a_1	a_2	a_3	a_4	a_5	a_6	b_1	b_i $(i \neq i)$	ϱ^r_{ini}
0.124	0.124	0.07	0.625	0.137	0.122	0	1	5.38×10^{-11}

The prescribed U_2 and U_3 are adjusted by one additional element for maintaining a constant stress triaxiality $T = 2$ defined as

$$T = \frac{\overline{\sigma}_m}{\overline{\sigma}_{eq}} = \frac{1 + \eta_2 + \eta_3}{3\sqrt{1 - \eta_2 - \eta_3 - \eta_2\eta_3 + \eta_2^2 + \eta_3^2}}, \tag{137}$$

where $\eta_2 = \overline{\sigma}_{22}/\overline{\sigma}_{11}$ and $\eta_3 = \overline{\sigma}_{33}/\overline{\sigma}_{11}$. For the applied axisymmetric loading considered in this section, the values $\eta_2 = \eta_3 = \eta = 0.625$ were chosen, corresponding to a triaxiality of 2.

A FCC single crystal with 12 slip systems is considered. The slip systems are specified by the slip direction $\underline{\ell}^r$ and the normal to the slip plane $\underline{\boldsymbol{n}}^r$ which are listed in Table 2, following Schmid and Boas convention. The crystal orientation is chosen with the lattice directions along the coordinate axes $X - Y - Z$. In the case of cylindrical voids, two crystal orientations are considered: [100]–[010]–[001] and [100]–[01$\bar{1}$]–[011]; in the case of spherical void, only the [100]–[010]–[001] orientation is considered. A cubic elasticity tensor $\underset{\approx}{\boldsymbol{\Lambda}}$ is considered and determined by three independent moduli C_{11}, C_{12} and C_{44}. The critical resolved shear stress τ_c^r of slip systems is given by Eqs. (47) and (48).

The material parameters used in the simulations are summarized in Table 3. They correspond to a solution annealed 304 austenitic stainless steel at 340 °C studied by Han et al. (2013); Ling et al. (2016). Note that a^{ru} and b^{ru} are 12×12 matrices and they can be specified by 6 independent parameters a_1, a_2, $\cdots$, a_6 and b_1, b_2, $\cdots$, b_6 (the structure of the matrices is presented in Appendix A). The values of a^{ru} are obtained by discrete dislocation dynamics (Kubin et al., 2008; Monnet, 2009), while no study is found in the literature for estimating the values of b_i $(i = 1, 2, \cdots, 6)$. It is assumed that $b_1 = 0$ and that $b_i = 1$ for $i \neq 1$ (Han et al., 2013). The initial values of adimensional dislocation densities ϱ^r_{ini} $(s = 1, 2, \cdots, 12)$ are the same. Recall that ϱ^r/b^2 is the dislocation density and b is the norm of Burgers' vector of the dislocations; $b = 2.54$ Å.

To study size effects, the side length L_0 of the unit cell is changed, while the moduli $H_\chi = 5 \times 10^4$ MPa and $A = 5$ N are fixed. It is the same value of H_χ as used in the study of localization phenomena in the previous section. Nevertheless, this value does not need to be the same. If the model is intended to represent a strain gradient plasticity model, the penalty term H_χ must be high enough for the microslip variable to be close enough to the cumulated slip. However, it should not be too large to avoid ill–conditioned matrices. The value is then a compromise and depends on the values of the critical resolved shear stress and hardening modulus of the material. The formula (127) provides an estimate of the material length scale. A value of H can be estimated from the curve giving the evolution of τ^r with respect to γ^r of one slip system at the beginning of its activation in tension. This is only a crude estimate since getting an analytical solution of the microslip field around the hole is almost out of reach for the complex considered hardening law. In this way, λ_c is calculated to be $\lambda_c = 0.06$ mm with the used parameters. In fact the following computation results only depend on the adimensional ratio L_0/λ_c, and not on the absolute values of L_0 and λ_c.

6.2. Void growth in 2D and 3D

Evolution of the void volume fraction, computed as

$$f = 1 - \frac{V_{\text{mesh}}}{V_{\text{tot}}}, \tag{138}$$

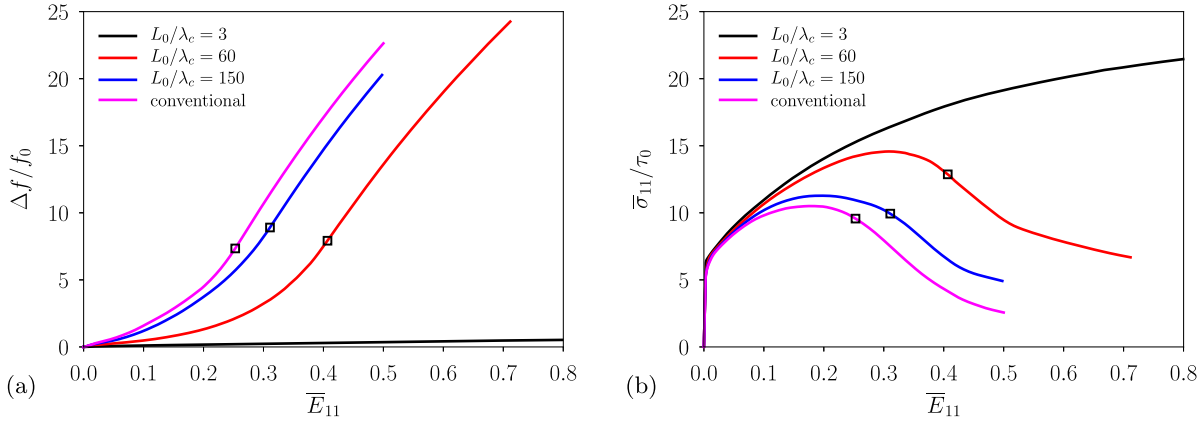

Fig. 13. Cylindrical void with $f_0 = 0.01$: (a) The variation of the normalized void volume fraction and (b) the overall stress–strain curves for different sizes of the unit cell. [100]–[010]–[001] orientation.

is first investigated. V_{mesh} is the current volume of the FE mesh which can be evaluated by post-processing the calculation and V_{tot} is the current total volume of the unit cell which obeys to $V_{\text{tot}} = (L_0 + U_1)(L_0 + U_2)w_0$ in the case of cylindrical void and $V_{\text{tot}} = (L_0 + U_1)(L_0 + U_2)(L_0 + U_3)$ for the cube. The increase in the void volume fraction is equal to $\Delta f = f - f_0$.

The variation of $\Delta f/f_0$ with respect to the overall strain $\overline{E}_{11} = U_1/L_0$ is shown in Fig. 13a for the cylindrical void with the [100]–[010]–[001] orientation and $f_0 = 0.01$. Note that the same computation has been performed with conventional single crystal plasticity. The void evolution predicted by the conventional theory does not depend on the size of unit cell. In general, two stages of void evolution are observed: in the first stage, the void grows relatively slowly; in the second stage, void growth rate is accelerated. The two stages are respectively called void growth and void coalescence in the literature. According to Koplik and Needleman (1988), the onset of void coalescence is characterized by the transition from biaxial to uniaxial straining associated with the localization of the plastic flow in the intervoid ligament. In contrast to the results of conventional crystal plasticity, the simulations with the micromorphic theory predict size–dependent void evolution. The void growth rate is found to decrease with decreasing normalized unit cell size L_0/λ_c. It is significantly reduced for very small unit cells and an absence of void growth is predicted for $L_0/\lambda_c = 3.0$. In addition, the void evolution tends to converge to the results obtained by the conventional theory when L_0/λ_c is large enough.

The overall stress $\overline{\sigma}_{11}$ is plotted in Fig. 13b as a function of the overall strain $\overline{E}_{11}$. For the simulation with the conventional theory, a hardening regime followed by softening is observed, which results from the competition between strain hardening of the matrix, softening due to void growth/coalescence. The micromorphic theory predicts a higher stress level as a result of the strain gradient hardening and the reduced void growth. The hardening regime is enhanced with the decreasing unit cell size L_0/λ_c. In particular, no softening regime is found for the unit cell with $L_0/\lambda_c = 3.0$, which is due to extremely low void growth rate. In this case, the voided unit cell behaves almost like a void-free unit cell.

Results for the [100]–[010]–[001] and [100]–[01$\bar{1}$]–[011] orientations with $f_0 = 0.1$ are shown in Fig. 14. For a given value of L_0/λ_c, the two orientations show similar void growth rates, but different stress–strain responses. This difference is related to different number of activated slip systems in the matrix. For a given value of L_0/λ_c, the [100]–[010]–[001] orientation shows higher stress level than [100]–[01$\bar{1}$]–[011]. Compared with the simulations for $f_0 = 0.01$, the evolution of $\Delta f/f_0$ does not display a clear transition to the accelerated void growth stage. However, the transition from the uniaxial to biaxial straining can be detected, i.e., the two stages (void growth and coalescence) can be determined also for this initial void volume fraction. The observed size effect on void growth is similar to that for $f_0 = 0.01$: void growth rate is decreased for small L_0/λ_c. However, the void growth for $L_0/\lambda_c = 3.0$ cannot be neglected here, unlike the case $f_0 = 0.01$.

In addition, similar size dependent overall stress–strain responses are observed for the two orientations as that observed for $f_0 = 0.01$. It is worth noting that the unit cell with $L_0/\lambda_c = 3.0$ does not show softening regime even after significant void growth.

Similar size dependent void growth and stress–strain responses are observed in the case of spherical void with the [100]–[010]–[001] orientation and $f_0 = 0.01$, as shown in Fig. 15. However, it is found that the softening part of the stress/strain curves starts at significantly higher strain values for spherical pores than for cylindical ones.

6.3. Void coalescence

The onset of void coalescence in the 2D case corresponds to a transition from biaxial to uniaxial straining, as noted by Koplik and Needleman (1988). The onset is determined in the following way. The ratio $a(t) = |U_2(t)|/|U_1(t)|$ is computed during straining. During void growth, this ratio is found to be almost constant, with the value a_0. It then suddenly decreases and tends toward zero corresponding to the transition to uniaxial straining along 1. A critical value $a_c = a_0/10$ is then chosen to detect the onset of coalescence. The corresponding critical value of the overall strain $\overline{E}_{11}$ is thus determined and denoted by $\overline{E}^c_{11}$.

The onset of coalescence is indicated by a hollow square in Figs. 13, 14 and 15. Compared with the result predicted by the conventional theory, the onset of coalescence is delayed for small unit cell sizes according to the micromorphic theory. $\overline{E}^c_{11}$ is plotted as a function of L_0/λ_c in Fig. 16 for cylindrical voids with the two orientations and $f_0 = 0.01$ and 0.1. The red symbols indicate $\overline{E}^c_{11}$ as predicted by the conventional theory. Since the coalescence is not predicted for $L_0/\lambda_c = 3.0$, $\overline{E}^c_{11}$ does not exist and is not plotted in the figure. Qualitatively similar results are shown for the two orientations and the two levels of f_0. A rapid decrease in $\overline{E}^c_{11}$ with L_0/λ_c is observed for $L_0/\lambda_c < 10$. It tends to stabilize with increasing L_0/λ_c and converge to the value predicted by the conventional theory.

After determining $\overline{E}^c_{11}$, the corresponding critical void volume fraction f_c for the coalescence can be readily found. f_c is plotted as a function of L_0/λ_c for the cylindrical void in Fig. 17. With the considered values of L_0/λ_c, the size effect on f_c can be neglected for $f_0 = 0.01$, while an increase in f_c with decreasing L_0/λ_c for

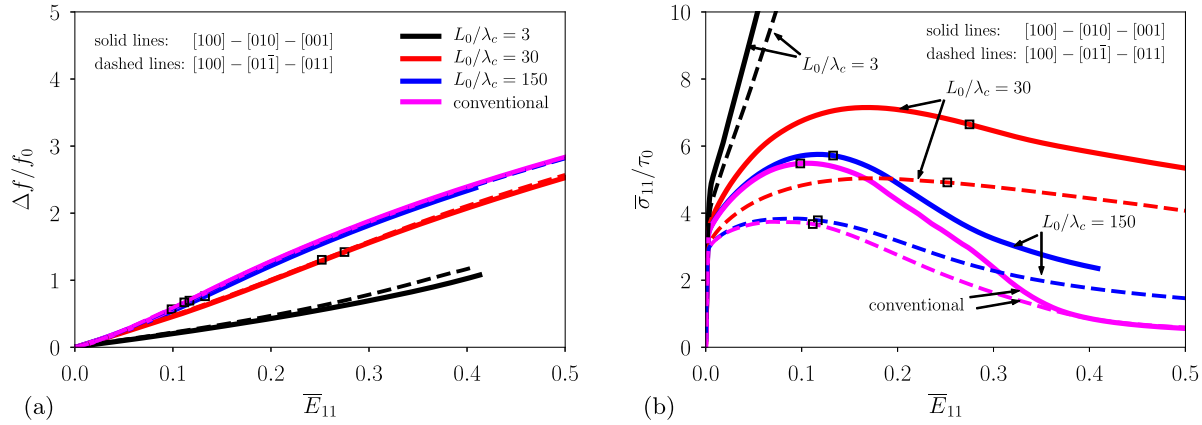

Fig. 14. Cylindrical void with $f_0 = 0.1$: (a) The variation of void volume fraction and (b) the overall stress–strain curves for various sizes of unit cell. Solid lines are for the [100] – [010] – [001] orientation and dashed lines for the [100] – [01$\bar{1}$] – [011] orientation.

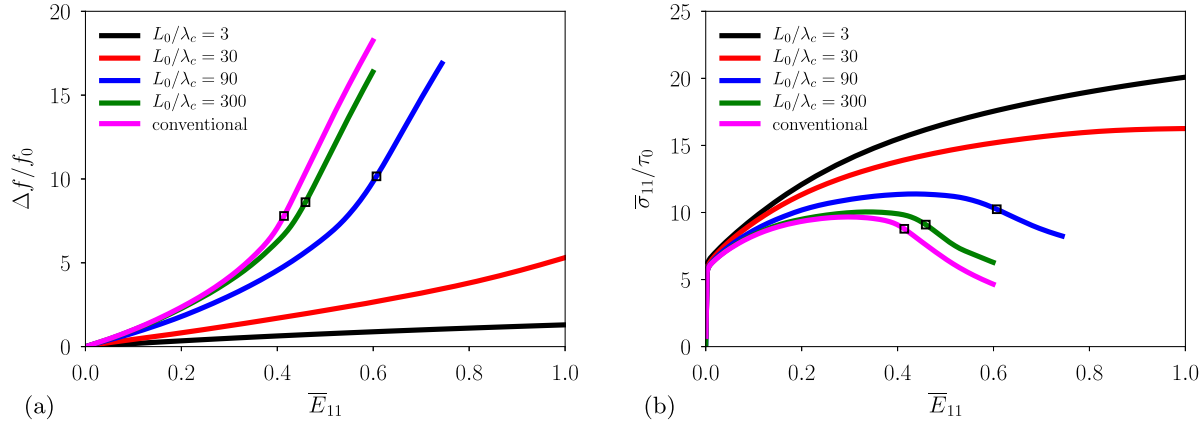

Fig. 15. Spherical void with $f_0 = 0.01$: (a) Variation of the normalized void volume and (b) overall stress–strain curves for different sizes of the unit cell. [100]–[010]–[001] orientation.

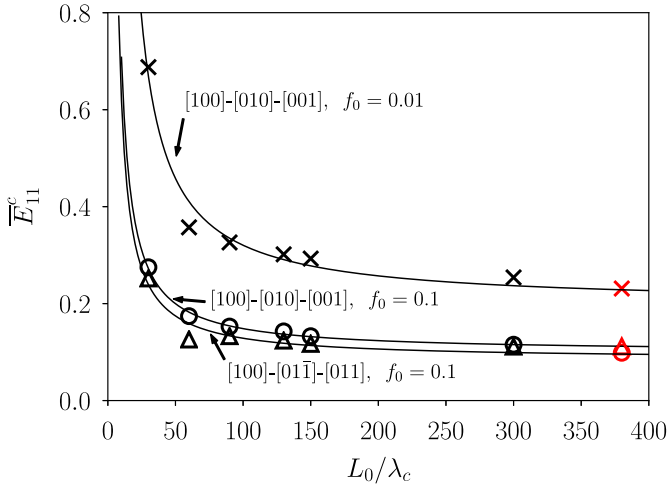

Fig. 16. Cylindrical void: Critical strain $\overline{E}^c_{11}$ for the onset of coalescence as a function of normalized size of unit cell.

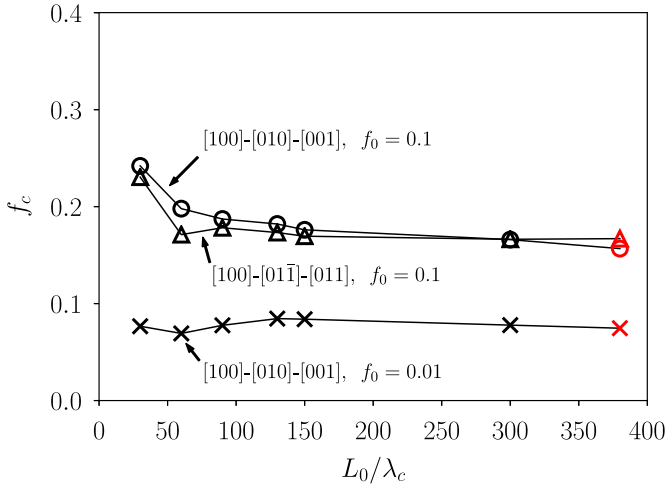

Fig. 17. Cylindrical void: Critical void volume fraction f_c for the onset of coalescence as a function of normalized size of unit cell.

$L_0/\lambda_c < 60$ is observed for the two orientations with $f_0 = 0.1$. Since the [100]–[010]–[001] and [100]–[01$\bar{1}$]–[011] orientations shows similar void growth rate, f_c is alike for the two orientations with a given value of $L_0/\lambda_c < 60$.

Size effects on the growth of spherical voids are qualitatively similar to that on cylindrical voids. They are quantitatively different since the critical strains at coalescence are found to be significantly larger for spherical than for cylindrical pores.

6.4. Discussion

Size–dependent overall behavior and void growth have been predicted by the micromorphic theory for voided single crystals.

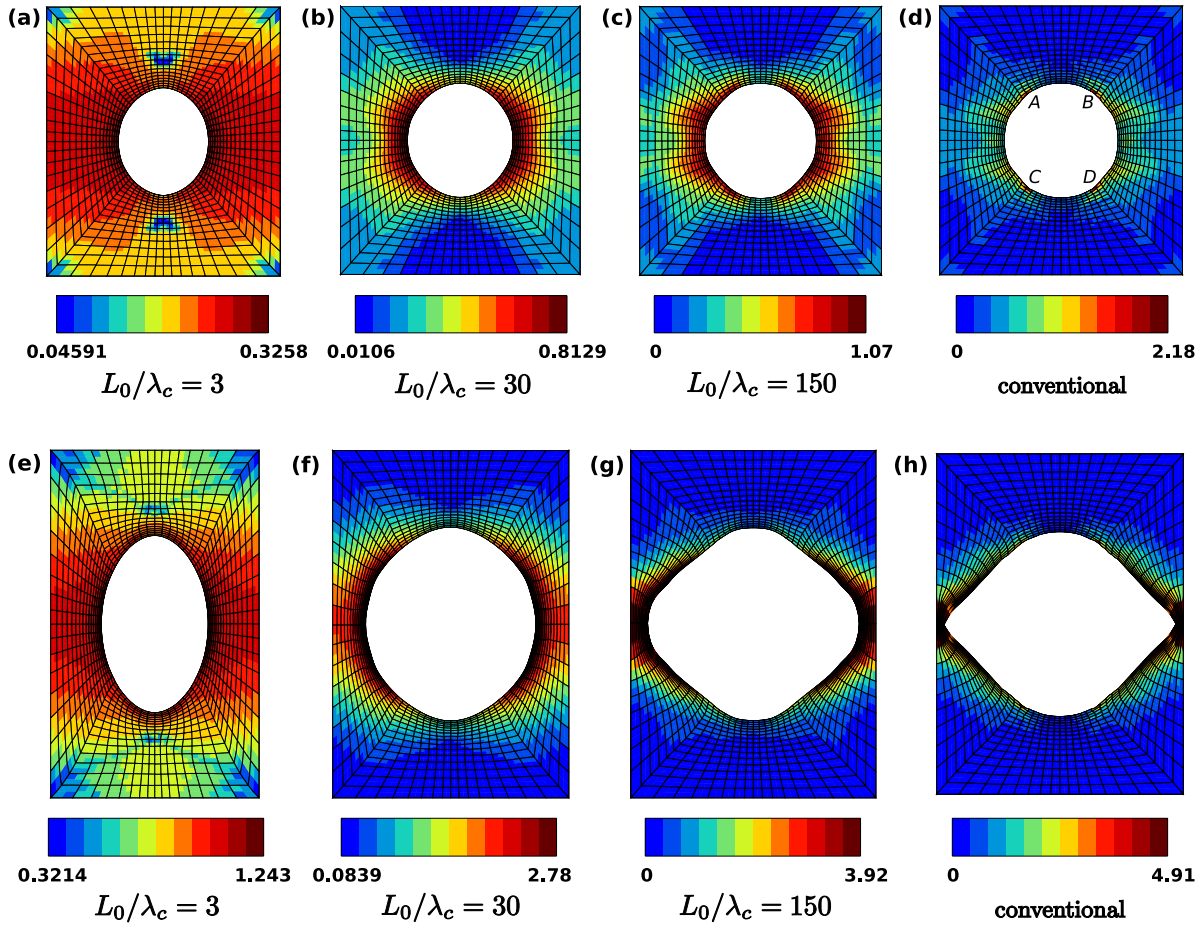

Fig. 18. Void shape for the [100] – [010] – [001] orientation at $\overline{E}_{11} = 0.1$ ((a)–(d)) and $\overline{E}_{11} = 0.4$ ((e)–(h)) for different unit cell sizes: (a,e) $L/\lambda_c = 3.0$, (b,f) $L/\lambda_c = 30$, (c,g) $L/\lambda_c = 150$ and (d,h) conventional model. $f_0 = 0.1$. The field of γ_{cum} is shown.

Qualitatively similar results have been obtained for the unit cell with various initial void volume fractions and crystal orientations: Unit cells of smaller size exhibit a lower void growth rate compared with larger ones. This results in a higher hardening rate at the beginning of plastic regime and delays the onset of void coalescence.

The impeded void growth in unit cells of small size is associated with the fact that the plastic deformation field becomes more diffuse in the micromorphic theory at these scales. For the cylindrical void with the [100]–[010]–[001] orientation and $f_0 = 0.1$, the cumulative slip γ_{cum} is shown in Fig. 18 ((a)–(d)) for the unit cells with different values of L_0/λ_c at the overall strain $\overline{E}_{11} = 0.1$. The conventional theory predicts significant localization of γ_{cum} at four zones around the void, called *A, B, C, D* in Fig. 18. It is worth noting that the maximum local γ_{cum} reaches the very large strain value 2.18 for the overall strain $\overline{E}_{11} = 0.1$. According to the micromorphic theory, the γ_{cum} field is more diffuse, especially at the four zones and becomes more and more diffuse as L_0/λ_c decreases from 150 to 3. As a result, void growth is slowed down and void coalescence is delayed. The diffuse field of γ_{cum} also influences the evolution of void shape, as shown in Fig. 18 ((e)–(h)) for the unit cells of different sizes at the overall strain $E_{11} = 0.4$. The void is shown to become an ellipsoid for the small unit cell size $L_0/\lambda_c = 3$. In this case, since the void coalescence does not occur, the void is elongated along the *X*–axis but the deformation of the void along the *Y*–axis is limited. The void is also ellipsoidal for $L_0/\lambda_c = 30$ at $E_{11} = 0.4$ (before the onset of void coalescence in this case). Compared with $L_0/\lambda_c = 3$, the void is more deformed along the *Y*–axis because of a less diffuse field of γ_{cum} in the region around the void. For the large unit cell with $L_0/\lambda_c = 150$, the lateral deformation of the void is large at $E_{11} = 0.4$ as a result of void coalescence. The conventional theory predicts a similar void shape as the micromorphic theory with $L_0/\lambda_c = 150$, except at the sharp corners.

The field of the cumulative slip γ_{cum} is shown in Fig. 19 for the [100]–[01$\bar{1}$]–[011] orientation with $f_0 = 0.1$. A different mode of plastic deformation is predicted compared with the [100]–[001]–[001] orientation, which results in slightly different void shapes as shown in Fig. 19 ((e)–(h)). Moreover, it is again found that the γ_{cum} field is more diffuse when decreasing value of L_0/λ_c.

The γ_{cum} field is shown in Fig. 20 for the unit cells with the [100]–[001]–[001] orientation, a spherical void and $f_0 = 0.01$. The location of the plastic slip localization zones is very different from the cylindrical case, with eight zones around the equator. These zones are predicted by the micromorphic model for large enough cell sizes. For smaller cell sizes, the plastic slip is more largely distributed around the equator and only four main localization zones remain.

In addition, the γ_{cum} values along a meridian line is plotted for the spherical void with $f_0 = 0.1$ in Fig. 21 as a function of the angle θ (cf. the definition of θ in Fig. 12a) at $E_{11} = 0.05$ (before significant void shape change) for the [100]–[001]–[001] orientation. The angular sectors of plastic activity are similar to those observed by Borg and Kysar (2007); Niordson and Kysar (2014) and some similarities can be observed for different unit cell sizes. The dis-

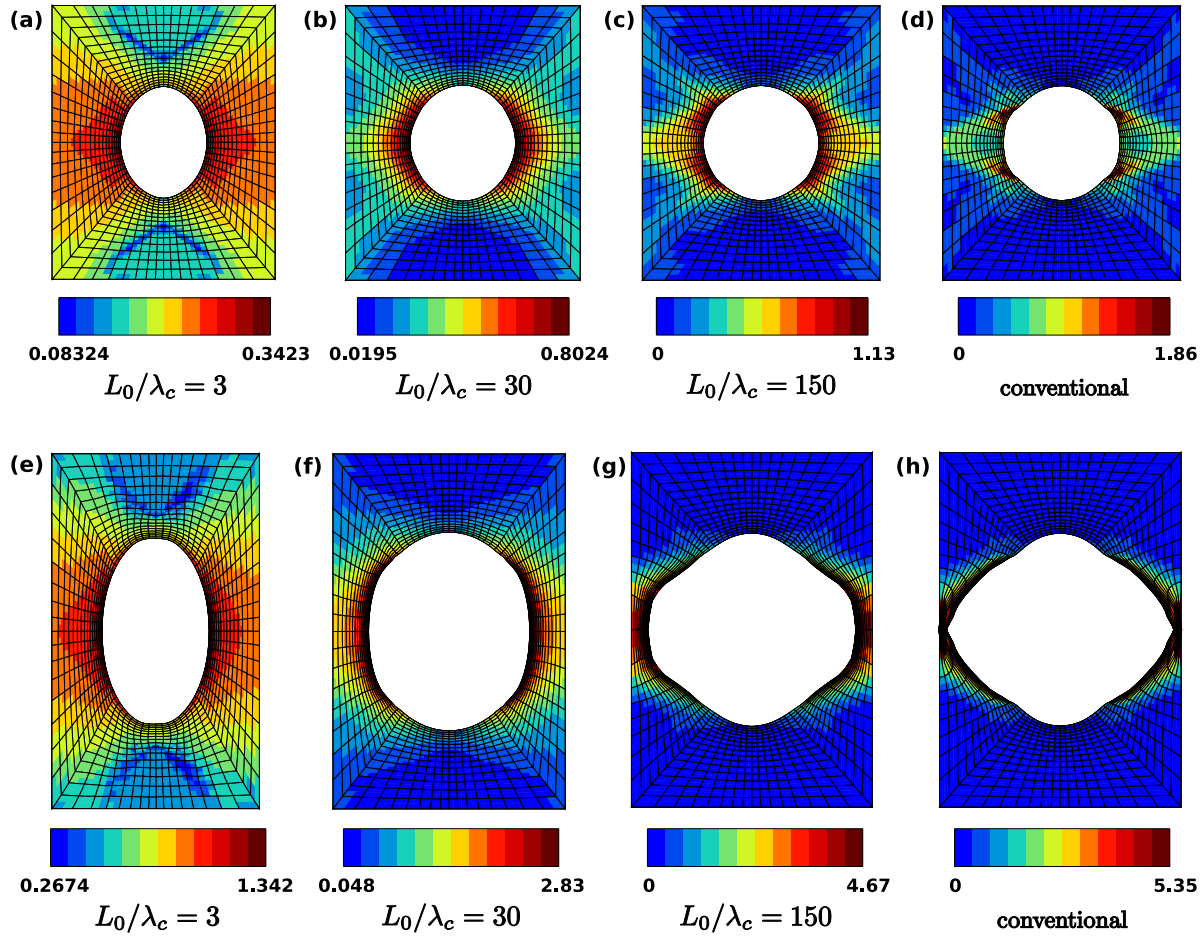

Fig. 19. Void shape for the [100] – [01$\bar{1}$] – [011] orientation at $\overline{E}_{11} = 0.1$ ((a)–(d)) and $\overline{E}_{11} = 0.4$ ((e)–(h)) for different unit cell sizes: (a,e) $L/\lambda_c = 3$, (b,f) $L/\lambda_c = 30$, (c,g) $L/\lambda_c = 150$ and (d,h) conventional model. $f_0 = 0.1$. The field of γ_{cum} is shown.

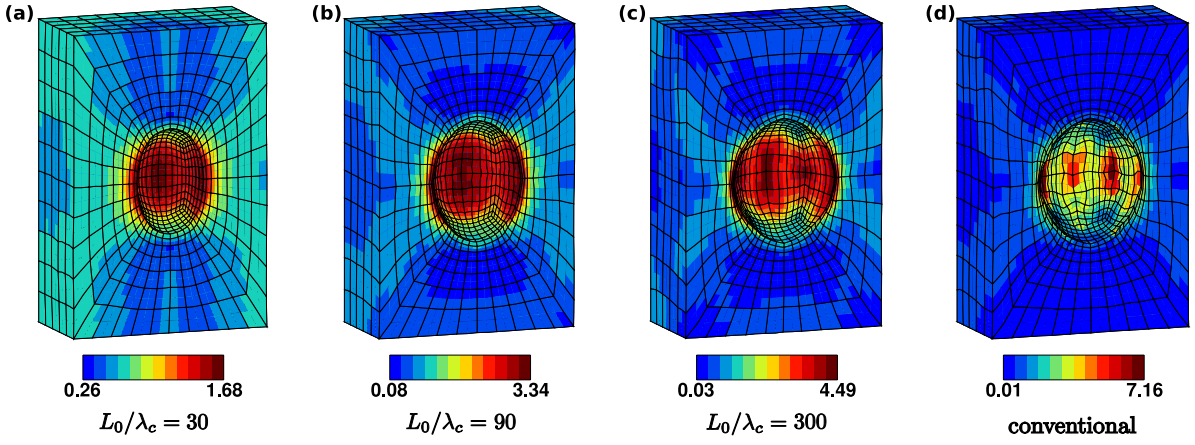

Fig. 20. Spherical void: Void shape for the [100] – [01$\bar{1}$] – [011] orientation at $\overline{E}_{11} = 0.3$ for different unit cell size: (a) $L/\lambda_c = 30$, (b) $L/\lambda_c = 90$, (c) $L/\lambda_c = 300$ and (d) conventional model. $f_0 = 0.01$. The field of γ_{cum} is shown.

tribution of γ_{cum} is shown to be smoother at the void surface for unit cells of smaller size than for larger ones. This is directly related to the reduced void growth for unit cells of small size. Also the number of points with maximum slip is reduced from 8 to 4 when decreasing the cell size.

7. Conclusions

The main original contributions of the present work are the following:

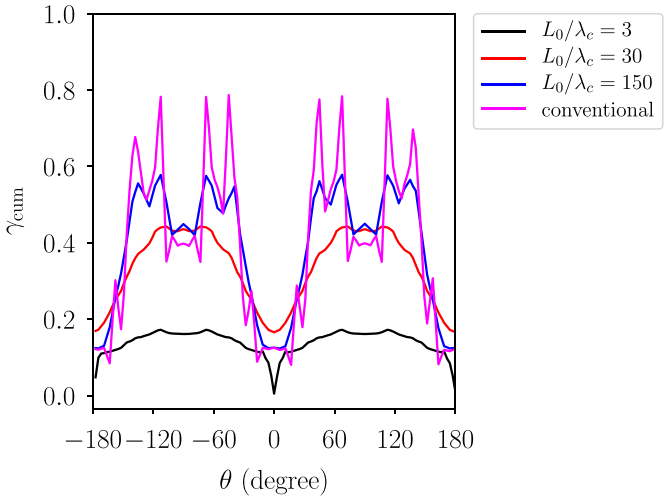

Fig. 21. Cumulative slip γ_{cum} profiles at the equator of spherical voids for $f_0 = 0.1$. $\overline{E}_{11} = 0.05$.

1. A micromorphic single crystal plasticity model has been proposed and implemented, accounting for both size–dependent hardening behaviour and strain localization phenomena at finite deformation. It represents an anisotropic and finite strain extension of existing regularisation models like in (Peerlings et al., 2012).
2. It is a reduced model compared to existing micromorphic and gradient crystal plasticity theories involving the full dislocation density tensor or GND densities, following Wulfinghoff and Böhlke (2012). Two advantages of this reduced model have been highlighted. First the computational cost is decreased since a single additional degree of freedom is introduced. Second, it was shown for the first time in the present work that both slip and kink bands are regularized leading to mesh–independent simulation of localization phenomena in crystals. This is in contrast to purely GND–based models. A drawback of the reduced model, however, is that the thickness of slip and kink bands are related to the same characteristic length, which is probably not the case in the physical reality.
3. The model is based essentially on enhanced isotropic hardening in the hardening law of each slip system. However, a variant of the constitutive formulation was shown to deliver a size–dependent kinematic hardening variable directly related to the microslip gradient and associated generalized stress vector defined on the intermediate isoclinic configuration. An analytical expression, derived in a simple case of single slip, shows that this back–stress component is a second order contribution which vanishes in the small deformation limit.
4. The competition between slip and kink banding in a single crystal plate leads to mesh–dependent spurious oscillations on the overall curves in the case of conventional crystal plasticity. The oscillations are smoothed out in the regularized simulations which were checked to be mesh–independent. This regularization effect is similar to that obtained by isotropic gradient plasticity models like (Aifantis, 1987; de Borst et al., 1993) including the Laplace of the cumulative plastic slip. The difference for the present theory is that the isotropic gradient effects rest on an anisotropic crystal plasticity framework.
5. The reduced model is able to reproduce the main qualitative features of void growth and coalescence of cylindrical voids embedded in a FCC single crystal matrix, predicted in the literature for more elaborate gradient crystal plasticity models (Borg et al., 2008). For the first time, finite element simulations of growth and coalescence of spherical voids were presented using a micromorphic crystal plasticity model. They show that the strain localization zones are different from the cylindrical case and coalescence is postponed compared to cylindrical voids. Small holes lead to delayed growth and coalescence and smoother plastic slip field around the hole, with a reduction of the number of localization zones. Results were provided for two initial void volume fractions and two crystal orientations.
6. A strong size effect is observed for the critical applied strain at coalescence, whereas the corresponding critical pore volume fraction is almost size–independent.
7. The numerical implementation within an implicit scheme involving consistent tangent matrices was shown to be efficient enough to allow for large local deformations larger than 2 without remeshing.

The limit of the proposed theory when the penalty parameter H_χ is sufficiently high is a gradient of cumulative slip model. A Lagrange multiplier could be used instead. In contrast to other approaches based on slip gradients on individual slip systems, the number of degrees of freedom in the present theory does not depend on the number of slip systems which makes it computationally more effective. The drawback is that the description of gradient effects is greatly simplified in that way and may not be sufficient to account for some specific anisotropic effects.

The proposed approach opens new prospects in the simulation of ductile fracture of crystalline solids. The model will be coupled with the porous single crystal model of Ling et al. (2016) in a future work, in order to simulate crack initiation and propagation in porous single crystals and polycrystals. This will correspond to anisotropic extensions of micromorphic homogenization schemes for porous materials, see Enakoutsa and Leblond (2009); Poh (2013); Biswas and Poh (2017); Hütter (2017b; 2017a).

A potential application of such enhanced theories is the simulation of strain localization and ductile fracture of irradiated single and polycrystals. In irradiated materials, deformation can localize in defect-free channels called “clear bands” (Robach et al., 2003) where defects are swept out by mobile dislocations. Ductile fracture due to void growth and coalescence remains one of the dominant fracture mechanisms in austenitic stainless steels (Margolin et al., 2016) especially at limited irradiation level (irradiation damage $<$ 10–20 displacements per atom). Two kinds of voids leading to ductile fracture exist in irradiated steels: voids directly induced by irradiation and voids nucleated on irradiation-induced precipitates. These voids are smaller than the size of a grain and embedded in grains, while they are usually of different sizes: smaller than 20–30 nm for the former (Margolin et al. (2016)) and smaller than 10μm for the latter (Little (1986)). Void growth and coalescence in triaxial stress fields in irradiated FCC single crystals were simulated recently using coupled evolution laws for dislocation densities and irradiation defects, and compared to experimental results, see (Hure et al., 2016; Ling et al., 2017). The next step will be to account for size effects based on the proposed micromorphic approach.

Appendix A. Form of the a^{ru} and b^{ru} matrices

In FCC single crystals, the matrices a^{ru} and b^{ru} $(s, u = 1, 2, \cdots, 12)$ have respectively $12 \times 12 = 144$ coefficients. a^{ru} is constructed as follows:

$$[a^{ru}] = \begin{array}{c} \begin{matrix} A2 & A3 & A6 & B2 & B4 & B5 & C1 & C3 & C5 & D1 & D4 & D6 \end{matrix} \\ \begin{bmatrix} a_1 & a_2 & a_2 & a_4 & a_5 & a_5 & a_3 & a_5 & a_6 & a_3 & a_6 & a_5 \\ & a_1 & a_2 & a_5 & a_3 & a_6 & a_5 & a_4 & a_5 & a_6 & a_3 & a_5 \\ & & a_1 & a_5 & a_6 & a_3 & a_6 & a_5 & a_3 & a_5 & a_5 & a_4 \\ & & & a_1 & a_2 & a_2 & a_3 & a_6 & a_5 & a_3 & a_5 & a_6 \\ & & & & a_1 & a_2 & a_6 & a_3 & a_5 & a_5 & a_4 & a_5 \\ & & & & & a_1 & a_5 & a_5 & a_4 & a_6 & a_5 & a_3 \\ & & & & & & a_1 & a_2 & a_2 & a_4 & a_5 & a_5 \\ & & & & & & & a_1 & a_2 & a_5 & a_3 & a_6 \\ & & & \text{Symmetric} & & & & & a_1 & a_5 & a_6 & a_3 \\ & & & & & & & & & a_1 & a_2 & a_2 \\ & & & & & & & & & & a_1 & a_2 \\ & & & & & & & & & & & a_1 \end{bmatrix} \end{array} \begin{matrix} A2 \\ A3 \\ A6 \\ B2 \\ B4 \\ B5 \\ C1 \\ C3 \\ C5 \\ D1 \\ D4 \\ D6 \end{matrix} \tag{A.1}$$

For symmetry reasons, the number of coefficients is reduced to six, i.e., a_i and b_i with $i = 1, 2, \cdots, 6$ (Franciosi (1985)). In the matrix, a_1 corresponds to self hardening, a_2 to coplanar interaction, a_3 to Hirth locks, a_4 to colinear interaction, a_5 to glissile junctions and a_6 to Lomer locks. The matrix b^{ru} has the same structure as a^{ru}.

Appendix B. Jacobian matrix for the integration of the constitutive equations

The Jacobian matrix is organized as follows

$$\begin{pmatrix} \frac{\partial R_{\underset{\sim}{E}}}{\partial \Delta_{\underset{\sim}{E}}} & \frac{\partial R_{\underset{\sim}{E}}}{\partial \Delta\gamma^p} & \frac{\partial R_{\underset{\sim}{E}}}{\partial \Delta\varrho^q} & \frac{\partial R_{\underset{\sim}{E}}}{\partial \Delta\gamma_{cum}} \\ \frac{\partial R_{\gamma^r}}{\partial \Delta_{\underset{\sim}{E}}} & \frac{\partial R_{\gamma^r}}{\partial \Delta\gamma^p} & \frac{\partial R_{\gamma^r}}{\partial \Delta\varrho^q} & \frac{\partial R_{\gamma^r}}{\partial \Delta\gamma_{cum}} \\ \frac{\partial R_{\varrho^r}}{\partial \Delta_{\underset{\sim}{E}}} & \frac{\partial R_{\varrho^r}}{\partial \Delta\gamma^p} & \frac{\partial R_{\varrho^r}}{\partial \Delta\varrho^q} & \frac{\partial R_{\varrho^r}}{\partial \Delta\gamma_{cum}} \\ \frac{\partial R_{\gamma_{cum}}}{\partial \Delta_{\underset{\sim}{E}}} & \frac{\partial R_{\gamma_{cum}}}{\partial \Delta\gamma^p} & \frac{\partial R_{\gamma_{cum}}}{\partial \Delta\varrho^q} & \frac{\partial R_{\gamma_{cum}}}{\partial \Delta\gamma_{cum}} \end{pmatrix}. \tag{B.1}$$

Each term of the matrix is calculated as follows.

- Derivatives of $R_{\underset{\sim}{E}}$

$$R_{\underset{\sim}{E}} = \Delta\underset{\sim}{E} - \Delta\underset{\sim}{F}.\underset{\sim}{F}^{-1} \cdot \underset{\sim}{E} + \underset{\sim}{E}.\left(\sum_{r=1}^{12} \Delta\gamma^r \underset{\sim}{N}^r\right) \tag{B.2}$$

$$\frac{\partial R_{\underset{\sim}{E}}}{\partial \Delta\underset{\sim}{E}} = \underset{\approx}{1} - (\Delta\underset{\sim}{F}.\underset{\sim}{F}^{-1}) \underline{\otimes}\underset{\approx}{1} + \underset{\approx}{1}\underline{\otimes}(\sum_{r=1}^{12} \Delta\gamma^r \underset{\sim}{N}^r)^T \tag{B.3}$$

$$\frac{\partial R_{\underset{\sim}{E}}}{\partial \Delta\gamma^p} = \underset{\sim}{E}.\underset{\sim}{N}^p, \quad \frac{\partial R_{\underset{\sim}{E}}}{\partial \Delta\varrho^q} = 0, \quad \frac{\partial R_{\underset{\sim}{E}}}{\partial \Delta\gamma_{cum}} = 0 \tag{B.4}$$

- Derivatives of R_{γ^r}

$$R_{\gamma^r} = \Delta\gamma^r - \Phi(|\tau^r| - (\tau_c^r - S))\text{sign}(\tau^r)\Delta t \tag{B.5}$$

$$\frac{\partial R_{\gamma^r}}{\partial \Delta\underset{\sim}{E}} = -\frac{\partial \Phi}{\partial \tau^r}\frac{\partial \tau^r}{\partial \underset{\sim}{M}} : \frac{\partial \underset{\sim}{M}}{\partial \underset{\sim}{C}^e} : \frac{\partial \underset{\sim}{C}^e}{\partial \underset{\sim}{E}} : \frac{\partial \underset{\sim}{E}}{\partial \Delta\underset{\sim}{E}} \text{sign}(\tau^r)\Delta t \tag{B.6}$$

with

$$\frac{\partial \Phi}{\partial \tau^r} = \frac{\partial \Phi}{\partial |\tau^r|}\frac{\partial |\tau^r|}{\partial \tau^r} = \frac{n\dot{\gamma}_0}{\sigma_0}\left\langle \frac{|\tau^r| - (\tau_c^r - S)}{\sigma_0} \right\rangle^{n-1}$$

$$\text{sign}(\tau^r) = \Phi' \text{sign}(\tau^r) \tag{B.7}$$

$$\frac{\partial \tau^r}{\partial \underset{\sim}{M}} = \underset{\sim}{N}^r \tag{B.8}$$

$$\frac{\partial \underset{\sim}{M}}{\partial \underset{\sim}{C}^e} = \frac{\partial \left[\underset{\sim}{C}^e.\left(\underset{\approx}{\Lambda} : \frac{1}{2}(\underset{\sim}{C}^e - 1)\right)\right]}{\partial \underset{\sim}{C}^e} = (\underset{\sim}{1}\underline{\otimes}\underset{\sim}{\Pi}^{eT}) + \frac{1}{2}(\underset{\sim}{C}^e\underline{\otimes}\underset{\sim}{1}) : \underset{\approx}{\Lambda} \tag{B.9}$$

$$\frac{\partial \underset{\sim}{C}^e}{\partial \underset{\sim}{E}} = \underset{\sim}{1}\overline{\otimes}\underset{\sim}{E}^T + \underset{\sim}{E}^T\underline{\otimes}\underset{\sim}{1}, \quad \frac{\partial \underset{\sim}{E}}{\partial \Delta\underset{\sim}{E}} = \underset{\approx}{1} \tag{B.10}$$

Finally,

$$\frac{\partial R_{\gamma^r}}{\partial \Delta\underset{\sim}{E}} = -\Delta t \Phi' \underset{\sim}{N}^r : \left[(\underset{\sim}{1}\underline{\otimes}\underset{\sim}{\Pi}^e) + \frac{1}{2}(\underset{\sim}{C}^e\underline{\otimes}\underset{\sim}{1}) : \underset{\approx}{\Lambda}\right] : (\underset{\sim}{1}\overline{\otimes}\underset{\sim}{E}^T + \underset{\sim}{E}^T\underline{\otimes}\underset{\sim}{1}) \tag{B.11}$$

with

$$\Phi' = \frac{n\dot{\gamma}_0}{\sigma_0}\left\langle \frac{|\tau^r| - (\tau_c^r - S)}{\sigma_0} \right\rangle^{n-1} \tag{B.12}$$

$$\frac{\partial R_{\gamma^r}}{\partial \Delta\gamma^p} = \delta_{sp}, \quad \frac{\partial R_{\gamma^r}}{\partial \Delta\varrho^q} = -\frac{\partial \Phi}{\partial \tau_c^r}\frac{\partial \tau_c^r}{\partial \varrho^q}\frac{\partial \varrho^q}{\partial \Delta\varrho^q}\text{sign}(\tau^r)\Delta t \tag{B.13}$$

with

$$\frac{\partial \Phi}{\partial \tau_c^r} = = -\Phi' = -\frac{n\dot{\gamma}_0}{\sigma_0}\left\langle \frac{|\tau^r| - (\tau_c^r - S)}{\sigma_0} \right\rangle^{n-1} \tag{B.14}$$

$$\frac{\partial \tau_c^r}{\partial \varrho^q} = \frac{1}{2}\mu\left(\sum_{u=1}^{12} a^{ru}\varrho^u\right)^{-\frac{1}{2}} a^{sq}, \quad \frac{\partial \varrho^q}{\partial \Delta\varrho^q} = 1 \tag{B.15}$$

Finally

$$\frac{\partial R_{\gamma^r}}{\partial \Delta\varrho^q} = \frac{1}{2}\text{sign}(\tau^r)\Delta t\Phi'\mu a^{sq}\left(\sum_{u=1}^{12} a^{ru}\varrho^u\right)^{-\frac{1}{2}} \tag{B.16}$$

$$\frac{\partial R_{\gamma^r}}{\partial \Delta\gamma_{cum}} = -\frac{\partial \Phi}{\partial S}\frac{\partial S}{\partial \gamma_{cum}}\frac{\partial \gamma_{cum}}{\partial \Delta\gamma_{cum}}\text{sign}(\tau^r)\Delta t \tag{B.17}$$

with

$$\frac{\partial \Phi}{\partial S} = \Phi' = \frac{n\dot{\gamma}_0}{\sigma_0}\left\langle \frac{|\tau^r| - (\tau_c^r - S)}{\sigma_0} \right\rangle^{n-1} \tag{B.18}$$

$$\frac{\partial S}{\partial \gamma_{cum}} = -H_\chi, \quad \frac{\partial \gamma_{cum}}{\partial \Delta\gamma_{cum}} = 1 \tag{B.19}$$

Finally

$$\frac{\partial R_{\gamma^r}}{\partial \Delta\gamma_{cum}} = \text{sign}(\tau^r)\Delta t H_\chi \Phi' \tag{B.20}$$

- Derivatives of R_{ϱ^r}

$$R_{\varrho^r} = \Delta\varrho^r - |\Delta\gamma^r|\left(\frac{\sqrt{\sum_{u=1}^N b^{ru}\varrho^u}}{\kappa} - G_c\varrho^r\right) \tag{B.21}$$

$$\frac{\partial R_{\varrho^r}}{\partial \Delta\underset{\sim}{E}} = 0, \quad \frac{\partial R_{\varrho^r}}{\partial \Delta\gamma^p} = -\text{sign}(\Delta\gamma^r)\delta_{sp}\left(\frac{\sqrt{\sum_{u=1}^N b^{ru}\varrho^u}}{\kappa} - G_c\varrho^r\right) \tag{B.22}$$

$$\frac{\partial R_{\varrho^r}}{\partial \Delta\varrho^q} = \delta_{sq} - |\Delta\gamma^r|\left(\frac{1}{2}\frac{\left(\sqrt{\sum_{u=1}^N b^{ru}\varrho^u}\right)^{-\frac{1}{2}} b^{sq}}{\kappa} - G_c\delta_{sq}\right),$$

$$\frac{\partial R_{\varrho^r}}{\partial \Delta\gamma_{cum}} = 0 \tag{B.23}$$

- Derivatives of $R_{\gamma_{cum}}$

$$R_{\gamma_{cum}} = \Delta\gamma_{cum} - \sum_{r=1}^{12} |\Delta\gamma^r| \tag{B.24}$$

$$\frac{\partial R_{\gamma_{cum}}}{\partial \Delta \underline{\underline{\mathbf{E}}}} = 0, \quad \frac{\partial R_{\gamma_{cum}}}{\partial \Delta\gamma^p} = -\text{sign}(\Delta\gamma^p) \tag{B.25}$$

$$\frac{\partial R_{\gamma_{cum}}}{\partial \Delta\varrho^q} = 0, \quad \frac{\partial R_{\gamma_{cum}}}{\partial \Delta\gamma_{cum}} = 1 \tag{B.26}$$

Appendix C. Details of the numerical implementation in the FE code

In order to facilitate the numerical implementation in FE code, the equations are written in vector and matrix form. The rates of nodal degrees of freedom $\dot{\tilde{u}}^a$ and $\dot{\tilde{\gamma}}^b_\chi$ are arranged in vector form as

$$\{\dot{\tilde{u}}^a_i\} = \{\dot{\tilde{\mathbf{u}}}^e\} = \begin{Bmatrix} \dot{\tilde{u}}^1_1 \\ \dot{\tilde{u}}^1_2 \\ \dot{\tilde{u}}^1_3 \\ \vdots \\ \dot{\tilde{u}}^p_1 \\ \dot{\tilde{u}}^p_2 \\ \dot{\tilde{u}}^p_3 \end{Bmatrix} \quad \text{and} \quad \{\dot{\tilde{\gamma}}^b_\chi\} = \{\dot{\tilde{\boldsymbol{\gamma}}}^e_\chi\} = \begin{Bmatrix} \dot{\tilde{\gamma}}^1_\chi \\ \dot{\tilde{\gamma}}^2_\chi \\ \vdots \\ \dot{\tilde{\gamma}}^q_\chi \end{Bmatrix}. \tag{C.1}$$

The superscripts a and b used for summation over the nodes of one element are dropped. A superscript label e is added in order to indicate that the vector is for one individual element and to distinguish it from vectors for the entire FE mesh. Recall that p is the number of nodes possessing displacement degrees of freedom and q is that for microslip γ_χ. Voigt's notation is used for writing tensors in the form of vectors and matrices. Especially, the second-order non-symmetric tensor $\underline{\underline{\mathbf{F}}}$ and the vector $\underline{\boldsymbol{K}}$ are arranged in the form:

$$\{\underline{\underline{\mathbf{F}}}\} = \begin{Bmatrix} F_{11} \\ F_{22} \\ F_{33} \\ F_{12} \\ F_{23} \\ F_{31} \\ F_{21} \\ F_{32} \\ F_{13} \end{Bmatrix} \quad \text{and} \quad \{\underline{\boldsymbol{K}}\} = \begin{Bmatrix} K_1 \\ K_2 \\ K_3 \end{Bmatrix}. \tag{C.2}$$

Thus, shape functions ${}^uN^a_i$ and ${}^\chi N^b$ can thus be written as

$$[{}^{\mathbf{u}}\mathbf{N}] = \begin{bmatrix} {}^uN^1 & 0 & 0 & \cdots & {}^uN^p & 0 & 0 \\ 0 & {}^uN^1 & 0 & \cdots & 0 & {}^uN^p & 0 \\ 0 & 0 & {}^uN^1 & \cdots & 0 & 0 & {}^uN^p \end{bmatrix} \tag{C.3}$$

and

$$[{}^\chi\mathbf{N}] = \begin{bmatrix} {}^\chi N^1 & {}^\chi N^2 & {}^\chi N^3 & \cdots & {}^\chi N^q \end{bmatrix}. \tag{C.4}$$

Accordingly, ${}^uB^a_{ij}$ and ${}^\chi B^a_i$ can also be written in matrix form denoted by $[{}^{\mathbf{u}}\mathbf{B}]$ and $[{}^\chi\mathbf{B}]$:

$$[{}^{\mathbf{u}}\mathbf{B}] = \begin{bmatrix} \frac{\partial {}^uN^1}{\partial X_1} & 0 & 0 & \cdots & \frac{\partial {}^uN^p}{\partial X_1} & 0 & 0 \\ 0 & \frac{\partial {}^uN^1}{\partial X_2} & 0 & \cdots & 0 & \frac{\partial {}^uN^p}{\partial X_2} & 0 \\ 0 & 0 & \frac{\partial {}^uN^1}{\partial X_3} & \cdots & 0 & 0 & \frac{\partial {}^uN^p}{\partial X_3} \\ \frac{\partial {}^uN^1}{\partial X_2} & 0 & 0 & \cdots & \frac{\partial {}^uN^p}{\partial X_2} & 0 & 0 \\ 0 & \frac{\partial {}^uN^1}{\partial X_3} & 0 & \cdots & 0 & \frac{\partial {}^uN^p}{\partial X_3} & 0 \\ 0 & 0 & \frac{\partial {}^uN^1}{\partial X_1} & \cdots & 0 & 0 & \frac{\partial {}^uN^p}{\partial X_1} \\ 0 & \frac{\partial {}^uN^1}{\partial X_1} & 0 & \cdots & 0 & \frac{\partial {}^uN^p}{\partial X_1} & 0 \\ 0 & 0 & \frac{\partial {}^uN^1}{\partial X_2} & \cdots & 0 & 0 & \frac{\partial {}^uN^p}{\partial X_2} \\ \frac{\partial {}^uN^1}{\partial X_3} & 0 & 0 & \cdots & \frac{\partial {}^uN^p}{\partial X_3} & 0 & 0 \end{bmatrix} \tag{C.5}$$

and

$$[{}^\chi\mathbf{B}] = \begin{bmatrix} \frac{\partial {}^\chi N^1}{\partial X_1} & \frac{\partial {}^\chi N^2}{\partial X_1} & \frac{\partial {}^\chi N^3}{\partial X_1} & \cdots & \frac{\partial {}^\chi N^q}{\partial X_1} \\ \frac{\partial {}^\chi N^1}{\partial X_2} & \frac{\partial {}^\chi N^2}{\partial X_2} & \frac{\partial {}^\chi N^3}{\partial X_2} & \cdots & \frac{\partial {}^\chi N^q}{\partial X_2} \\ \frac{\partial {}^\chi N^1}{\partial X_3} & \frac{\partial {}^\chi N^2}{\partial X_3} & \frac{\partial {}^\chi N^3}{\partial X_3} & \cdots & \frac{\partial {}^\chi N^q}{\partial X_3} \end{bmatrix} \tag{C.6}$$

The interpolation of the increment of displacement $\dot{u}_i$ and that of the microslip $\dot{\gamma}_\chi$ in one element thus write

$$\{\dot{\underline{\boldsymbol{u}}}\} = [{}^{\mathbf{u}}\mathbf{N}].\{\dot{\tilde{\mathbf{u}}}^e\}, \quad \{\dot{\boldsymbol{\gamma}}_\chi\} = [{}^\chi\mathbf{N}].\{\dot{\tilde{\boldsymbol{\gamma}}}^e_\chi\} \tag{C.7}$$

and their Lagrangian gradients follow

$$\{\dot{\underline{\underline{\mathbf{F}}}}\} = [{}^{\mathbf{u}}\mathbf{B}].\{\dot{\tilde{\mathbf{u}}}^e\}, \quad \{\dot{\underline{\boldsymbol{K}}}\} = [{}^\chi\mathbf{B}].\{\dot{\tilde{\boldsymbol{\gamma}}}^e_\chi\}. \tag{C.8}$$

With stress and strain variables expressed with Voigt's notation, Eqs. (100) and (101) follow

$$\begin{aligned} \{\mathbf{R}^e_{\text{int}(u)}\} &= \int_{D^e_0} [{}^{\mathbf{u}}\mathbf{B}]^T.\{\underline{\mathbf{S}}\}\, dV_0, \quad \{\mathbf{R}^e_{\text{int}(\gamma_\chi)}\} \\ &= \int_{D^e_0} [{}^\chi\mathbf{N}]^T.\{S\} + [{}^\chi\mathbf{B}]^T.\{\underline{\boldsymbol{M}}\}\, dV_0, \end{aligned} \tag{C.9}$$

$$\begin{aligned} \{\mathbf{R}^e_{\text{ext}(u)}\} &= \int_{\partial D^e_0} [{}^{\mathbf{u}}\mathbf{N}]^T.\{\underline{\boldsymbol{T}}\}\, dS_0, \quad \{\mathbf{R}^e_{\text{ext}(\gamma_\chi)}\} \\ &= \int_{\partial D^e_0} [{}^\chi\mathbf{N}]^T.\{M\}\, dS_0, \end{aligned} \tag{C.10}$$

where $[{}^{\mathbf{u}}\mathbf{B}]^T$ is the transpose of the matrix $[{}^{\mathbf{u}}\mathbf{B}]$ and the same notation is used for other matrices. The global FE equation is obtained by applying assembly operator $\mathcal{A}$ on internal reactions and external reactions:

$$\{\mathbf{R}_{\text{int}(u)}\} = \mathcal{A}(\{\mathbf{R}^e_{\text{int}(u)}\}), \quad \{\mathbf{R}_{\text{int}(\gamma_\chi)}\} = \mathcal{A}(\{\mathbf{R}^e_{\text{int}(\gamma_\chi)}\}), \tag{C.11}$$

$$\{\mathbf{R}_{\text{ext}(u)}\} = \mathcal{A}(\{\mathbf{R}^e_{\text{ext}(u)}\}), \quad \{\mathbf{R}_{\text{ext}(\gamma_\chi)}\} = \mathcal{A}(\{\mathbf{R}^e_{\text{ext}(\gamma_\chi)}\}). \tag{C.12}$$

The reader is referred to Besson et al. (2009) for the description of the assembly procedure. Thus, the global FE equation (Eq. 102) to be solved can be written as

$$\begin{Bmatrix} \{\mathbf{R}_{\text{int}(u)}\} \\ \{\mathbf{R}_{\text{int}(\gamma_\chi)}\} \end{Bmatrix}.\begin{Bmatrix} \{\dot{\tilde{\mathbf{u}}}\} \\ \{\dot{\tilde{\boldsymbol{\gamma}}}_\chi\} \end{Bmatrix} = \begin{Bmatrix} \{\mathbf{R}_{\text{ext}(u)}\} \\ \{\mathbf{R}_{\text{ext}(\gamma_\chi)}\} \end{Bmatrix}.\begin{Bmatrix} \{\dot{\tilde{\mathbf{u}}}\} \\ \{\dot{\tilde{\boldsymbol{\gamma}}}_\chi\} \end{Bmatrix}. \tag{C.13}$$

The system is solved using Newton's method which requires the calculation of the Jacobian matrix with respect to the internal reactions (Besson et al., 2009). The Jacobian matrix of an individual element, split into four blocks, writes

$$\begin{bmatrix} [\mathbf{K}^e_{(uu)}] & [\mathbf{K}^e_{(ug)}] \\ [\mathbf{K}^e_{(gu)}] & [\mathbf{K}^e_{(gg)}] \end{bmatrix} = \begin{bmatrix} \left[\frac{\partial\{\mathbf{R}^e_{\mathrm{int}(u)}\}}{\partial\{\tilde{\mathbf{u}}^e\}}\right] & \left[\frac{\partial\{\mathbf{R}^e_{\mathrm{int}(u)}\}}{\partial\{\tilde{\boldsymbol{\gamma}}^e_\chi\}}\right] \\ \left[\frac{\partial\{\mathbf{R}^e_{\mathrm{int}(\gamma_\chi)}\}}{\partial\{\tilde{\mathbf{u}}^e\}}\right] & \left[\frac{\partial\{\mathbf{R}^e_{\mathrm{int}(\gamma_\chi)}\}}{\partial\{\tilde{\boldsymbol{\gamma}}^e_\chi\}}\right] \end{bmatrix}. \tag{C.14}$$

Using the assembly operation $\mathcal{A}$, one can calculate the global Jacobian matrix $[\mathbf{K}]$

$$[\mathbf{K}] = \mathcal{A}\begin{bmatrix} [\mathbf{K}^e_{(uu)}] & [\mathbf{K}^e_{(ug)}] \\ [\mathbf{K}^e_{(gu)}] & [\mathbf{K}^e_{(gg)}] \end{bmatrix} \tag{C.15}$$

One calculates the blocks for an individual element and obtains the so-called element stiffness matrix:

$$[\mathbf{K}^e_{(uu)}] = \frac{\partial\{\mathbf{R}^e_{\mathrm{int}(u)}\}}{\partial\{\tilde{\mathbf{u}}^e\}} = \int_{D_0} [{}^{u}\mathbf{B}]^T \cdot \frac{\partial\{\underset{\sim}{\mathbf{S}}\}}{\partial\{\underset{\sim}{\mathbf{F}}\}} \cdot \frac{\partial\{\underset{\sim}{\mathbf{F}}\}}{\partial\{\tilde{\mathbf{u}}^e\}}\, dV_0 = \int_{D_0} [{}^{u}\mathbf{B}]^T \cdot \frac{\partial\{\underset{\sim}{\mathbf{S}}\}}{\partial\{\underset{\sim}{\mathbf{F}}\}} \cdot [{}^{u}\mathbf{B}]\, dV_0 \tag{C.16}$$

$$[\mathbf{K}^e_{(ug)}] = \frac{\partial\{\mathbf{R}^e_{\mathrm{int}(u)}\}}{\partial\{\tilde{\boldsymbol{\gamma}}^e_\chi\}} = \int_{D_0} \left([{}^{u}\mathbf{B}]^T \cdot \frac{\partial\{\underset{\sim}{\mathbf{S}}\}}{\partial\{\boldsymbol{\gamma}_\chi\}} \cdot \frac{\partial\{\boldsymbol{\gamma}_\chi\}}{\partial\{\tilde{\boldsymbol{\gamma}}^e_\chi\}} + [{}^{u}\mathbf{B}]^T \cdot \frac{\partial\{\underset{\sim}{\mathbf{S}}\}}{\partial\{\underline{\underline{\boldsymbol{K}}}\}} \cdot \frac{\partial\{\underline{\underline{\boldsymbol{K}}}\}}{\partial\{\tilde{\boldsymbol{\gamma}}^e_\chi\}} \right) dV_0 = \int_{D_0} \left([{}^{u}\mathbf{B}]^T \cdot \frac{\partial\{\underset{\sim}{\mathbf{S}}\}}{\partial\{\boldsymbol{\gamma}_\chi\}} \cdot [{}^{\chi}\mathbf{N}] + [{}^{u}\mathbf{B}]^T \cdot \frac{\partial\{\underset{\sim}{\mathbf{S}}\}}{\partial\{\underline{\underline{\boldsymbol{K}}}\}} \cdot [{}^{\chi}\mathbf{B}] \right) dV_0 \tag{C.17}$$

$$[\mathbf{K}^e_{(gu)}] = \frac{\partial\{\mathbf{R}^e_{\mathrm{int}(\gamma_\chi)}\}}{\partial\{\tilde{\mathbf{u}}^e\}} = \int_{D_0} \left([{}^{\chi}\mathbf{N}]^T \cdot \frac{\partial\{S\}}{\partial\{\underset{\sim}{\mathbf{F}}\}} \cdot \frac{\partial\{\underset{\sim}{\mathbf{F}}\}}{\partial\{\tilde{\mathbf{u}}^e\}} + [{}^{\chi}\mathbf{B}]^T \cdot \frac{\partial\{\underline{\underline{\boldsymbol{M}}}\}}{\partial\{\underset{\sim}{\mathbf{F}}\}} \cdot \frac{\partial\{\underset{\sim}{\mathbf{F}}\}}{\partial\{\tilde{\mathbf{u}}^e\}} \right) dV_0 = \int_{D_0} \left([{}^{\chi}\mathbf{N}]^T \cdot \frac{\partial\{S\}}{\partial\{\underset{\sim}{\mathbf{F}}\}} \cdot [{}^{u}\mathbf{B}] + [{}^{\chi}\mathbf{B}]^T \cdot \frac{\partial\{\underline{\underline{\boldsymbol{M}}}\}}{\partial\{\underset{\sim}{\mathbf{F}}\}} \cdot [{}^{u}\mathbf{B}] \right) dV_0 \tag{C.18}$$

$$\begin{aligned}[\mathbf{K}^e_{(gg)}] = \frac{\partial\{\mathbf{R}^e_{\mathrm{int}(\gamma_\chi)}\}}{\partial\{\tilde{\boldsymbol{\gamma}}^e_\chi\}} &= \int_{D_0} \left([{}^{\chi}\mathbf{N}]^T \cdot \frac{\partial\{S\}}{\partial\{\boldsymbol{\gamma}_\chi\}} \cdot \frac{\partial\{\boldsymbol{\gamma}_\chi\}}{\partial\{\tilde{\boldsymbol{\gamma}}^e_\chi\}} + [{}^{\chi}\mathbf{B}]^T \cdot \frac{\partial\{\underline{\underline{\boldsymbol{M}}}\}}{\partial\{\boldsymbol{\gamma}_\chi\}} \cdot \frac{\partial\{\boldsymbol{\gamma}_\chi\}}{\partial\{\tilde{\boldsymbol{\gamma}}^e_\chi\}} \right. \\ &\quad \left. + [{}^{\chi}\mathbf{N}]^T \cdot \frac{\partial\{S\}}{\partial\{\underline{\underline{\boldsymbol{K}}}\}} \cdot \frac{\partial\{\underline{\underline{\boldsymbol{K}}}\}}{\partial\{\tilde{\boldsymbol{\gamma}}^e_\chi\}} + [{}^{\chi}\mathbf{B}]^T \cdot \frac{\partial\{\underline{\underline{\boldsymbol{M}}}\}}{\partial\{\underline{\underline{\boldsymbol{K}}}\}} \cdot \frac{\partial\{\underline{\underline{\boldsymbol{K}}}\}}{\partial\{\tilde{\boldsymbol{\gamma}}^e_\chi\}} \right) dV_0 \\ &= \int_{D_0} \left([{}^{\chi}\mathbf{N}]^T \cdot \frac{\partial\{S\}}{\partial\{\boldsymbol{\gamma}_\chi\}} \cdot [{}^{\chi}\mathbf{N}] + [{}^{\chi}\mathbf{B}]^T \cdot \frac{\partial\{\underline{\underline{\boldsymbol{M}}}\}}{\partial\{\boldsymbol{\gamma}_\chi\}} \cdot [{}^{\chi}\mathbf{N}] \right. \\ &\quad \left. + [{}^{\chi}\mathbf{N}]^T \cdot \frac{\partial\{S\}}{\partial\{\underline{\underline{\boldsymbol{K}}}\}} \cdot [{}^{\chi}\mathbf{B}] + [{}^{\chi}\mathbf{B}]^T \cdot \frac{\partial\{\underline{\underline{\boldsymbol{M}}}\}}{\partial\{\underline{\underline{\boldsymbol{K}}}\}} \cdot [{}^{\chi}\mathbf{B}] \right) dV_0. \end{aligned} \tag{C.19}$$

In the element stiffness matrix, one can find nine derivatives which will be evaluated using the consistent tangent matrix $\{\mathbf{J}^*\}$ in the next section. The consistent tangent matrix $\{\mathbf{J}^*\}$ is defined as:

$$\begin{bmatrix} \frac{\partial\{\Delta\underset{\sim}{\mathbf{S}}\}}{\partial\{\Delta\underset{\sim}{\mathbf{F}}\}} & \frac{\partial\{\Delta\underset{\sim}{\mathbf{S}}\}}{\partial\{\Delta\boldsymbol{\gamma}_\chi\}} & \frac{\partial\{\Delta\underset{\sim}{\mathbf{S}}\}}{\partial\{\Delta\underline{\underline{\boldsymbol{K}}}\}} \\ \frac{\partial\{\Delta S\}}{\partial\{\Delta\underset{\sim}{\mathbf{F}}\}} & \frac{\partial\{\Delta S\}}{\partial\{\Delta\boldsymbol{\gamma}_\chi\}} & \frac{\partial\{\Delta S\}}{\partial\{\Delta\underline{\underline{\boldsymbol{K}}}\}} \\ \frac{\partial\{\Delta\underline{\underline{\boldsymbol{M}}}\}}{\partial\{\Delta\underset{\sim}{\mathbf{F}}\}} & \frac{\partial\{\Delta\underline{\underline{\boldsymbol{M}}}\}}{\partial\{\Delta\boldsymbol{\gamma}_\chi\}} & \frac{\partial\{\Delta\underline{\underline{\boldsymbol{M}}}\}}{\partial\{\Delta\underline{\underline{\boldsymbol{K}}}\}} \end{bmatrix}. \tag{C.20}$$

In addition, it can be shown that $\frac{\partial\{\Delta S\}}{\partial\{\Delta\underline{\underline{\boldsymbol{K}}}\}}$ and $\frac{\partial\{\Delta\underline{\underline{\boldsymbol{M}}}\}}{\partial\{\Delta\boldsymbol{\gamma}_\chi\}}$ vanish for the constitutive model implemented in this work.

Appendix D. Consistent tangent matrix

As presented in Section 4.2 and Appendix C, the tangent operators are necessary for evaluating the element stiffness matrix. In the present work, they are estimated from the incremental form of constitutive equations (Besson et al., 2009). In fig. 4.1, it has been shown that the integration of the constitutive equations concerns solving the residual equations (eqs. (88) to (91)). For that purpose, input and output variables were defined in Fig. 1. The residual equations are expressed in terms of increments of the integration variables Δv_{int} and increments of the input variables Δv_{IN}. The calculation of the consistent tangent matrix is performed after the integration of the constitutive equations, and one has to solve the residual equations

$$\{R(\Delta v_{\mathrm{int}}, \Delta v_{\mathrm{IN}})\} = \{0\} \tag{D.1}$$

with imposed Δv_{IN} and obtained Δv_{int}. By applying an infinitesimal variation to the increments Δv_{IN}, one can obtain a new Δv_{int} according to the requirement of vanishing residual equations. The variation of Δv_{int} resulting from the variation of Δv_{IN} should make the variation of $\{R\}$ vanish, which implies

$$\{\delta R\} = \frac{\{\partial R\}}{\{\partial \Delta v_{\mathrm{int}}\}}\{\delta \Delta v_{\mathrm{int}}\} + \frac{\{\partial R\}}{\{\partial \Delta v_{\mathrm{IN}}\}}\{\delta \Delta v_{\mathrm{IN}}\} = \{0\}. \tag{D.2}$$

It follows that

$$\{\delta \Delta v_{\mathrm{int}}\} = \left[-\left(\frac{\{\partial R\}}{\{\partial \Delta v_{\mathrm{int}}\}} \right)^{-1} \frac{\{\partial R\}}{\{\partial \Delta v_{\mathrm{IN}}\}} \right] \{\delta \Delta v_{\mathrm{IN}}\}, \tag{D.3}$$

Moreover, noticing the constitutive equations Eqs. (51), (50) and (82), one can find that v_{OUT} depends on not only v_{int}, but also v_{IN}, i.e.,

$$v_{\mathrm{OUT}} = v_{\mathrm{OUT}}(v_{\mathrm{int}}, v_{\mathrm{IN}}), \quad \text{and} \quad \Delta v_{\mathrm{OUT}} = \Delta v_{\mathrm{OUT}}(\Delta v_{\mathrm{int}}, \Delta v_{\mathrm{IN}}). \tag{D.4}$$

The variation of Δv_{OUT} should follow

$$\delta \Delta v_{\mathrm{OUT}} = \frac{\partial \Delta v_{\mathrm{OUT}}}{\partial \Delta v_{\mathrm{int}}} \delta \Delta v_{\mathrm{int}} + \frac{\partial \Delta v_{\mathrm{OUT}}}{\partial \Delta v_{\mathrm{IN}}} \delta \Delta v_{\mathrm{IN}}. \tag{D.5}$$

Substituting Eq. (D.3) into the previous equation leads to

$$\delta \Delta v_{\mathrm{OUT}} = \left\{ \frac{\partial \Delta v_{\mathrm{OUT}}}{\partial \Delta v_{\mathrm{int}}} \left[-\left(\frac{\partial R}{\partial \Delta v_{\mathrm{int}}} \right)^{-1} \frac{\partial R}{\partial \Delta v_{\mathrm{IN}}} \right] + \frac{\partial \Delta v_{\mathrm{OUT}}}{\partial \Delta v_{\mathrm{IN}}} \right\} \delta \Delta v_I, \tag{D.6}$$

where $\left\{ \frac{\partial \Delta v_{\mathrm{OUT}}}{\partial \Delta v_{\mathrm{int}}} \left[-\left(\frac{\partial R}{\partial \Delta v_{\mathrm{int}}} \right)^{-1} \frac{\partial R}{\partial \Delta v_{\mathrm{IN}}} \right] + \frac{\partial \Delta v_{\mathrm{OUT}}}{\partial \Delta v_{\mathrm{IN}}} \right\}$ is the consistent tangent matrix. As can be seen, the calculation of the consistent tangent matrix requires the calculation of the following four matrices: $\frac{\partial \Delta v_{\mathrm{OUT}}}{\partial \Delta v_{\mathrm{int}}}$, $\frac{\partial R}{\partial \Delta v_{\mathrm{int}}}$, $\frac{\partial R}{\partial \Delta v_{\mathrm{IN}}}$ and $\frac{\partial \Delta v_{\mathrm{OUT}}}{\partial \Delta v_{\mathrm{IN}}}$. The reader is referred to (Ling, 2017) for the detailed expressions of these matrices.

References

Aifantis, E.C., 1987. The physics of plastic deformation. Int. J. Plast. 3, 211–247. doi:10.1016/0749-6419(87)90021-0.

Asaro, R.J., Rice, J.R., 1977. Strain localization in ductile single crystals. J. Mech. Phys. Solids 25, 309–338. doi:10.1016/0022-5096(77)90001-1.

Ashby, M., 1971. The Deformation of Plastically Non-homogeneous Alloys. In: Kelly, A., Nicholson, R. (Eds.), Strengthening Methods in Crystals. Applied Science Publishers, London, pp. 137–192.

Aslan, O., Cordero, N.M., Gaubert, A., Forest, S., 2011. Micromorphic approach to single crystal plasticity and damage. Int. J. Eng. Sci. 49, 1311–1325. doi:10.1016/j.ijengsci.2011.03.008.

Aslan, O., Forest, S., 2009. Crack growth modelling in single crystals based on higher order continua. Comput. Mater. Sci 45, 756–761.

Bardella, L., 2007. Some remarks on the strain gradient crystal plasticity modelling, with particular reference to the material length scales involved. Int. J. Plast. 23, 296–322.

Bardella, L., Segurado, J., Panteghini, A., Llorca, J., 2013. Latent hardening size effects in small-scale plasticity. Modell. Simul. Mater. Sci. Eng. 21, 055009.

Bayley, C.J., Brekelmans, W.A.M., Geers, M.G.D., 2006. A comparison of dislocation induced back stress formulations in strain gradient crystal plasticity. Int. J. Solids Struct. 43, 7268–7286. doi:10.1016/j.ijsolstr.2006.05.011. Size-dependent Mechanics of Materials

Besson, J., Cailletaud, G., Chaboche, J.L., Forest, S., 2009. Non-linear mechanics of materials, vol. 167. Springer Science & Business Media.

Besson, J., Foerch, R., 1997. Large scale object–oriented finite element code design. Comput. Meth. Appl. Mech. Eng. 142, 165–187.
Biswas, R., Poh, L., 2017. A micromorphic computational homogenization framework for heterogeneous materials. J. Mech. Phys. Solids 102, 187–208. doi:10.1016/j.jmps.2017.02.012.
Borg, U., Kysar, J.W., 2007. Strain gradient crystal plasticity analysis of a single crystal containing a cylindrical void. Int. J. Solids Struct. 44, 6382–6397. doi:10.1016/j.ijsolstr.2007.02.032.
Borg, U., Niordson, C.F., Kysar, J.W., 2008. Size effects on void growth in single crystals with distributed voids. Int. J. Plast. 24, 688–701. doi:10.1016/j.ijplas.2007.07.015.
de Borst, R., Sluys, L., Mühlhaus, H., Pamin, J., 1993. Fundamental issues in finite element analyses of localization of deformation. Eng. Comput. (Swansea) 10, 99–121.
Chang, H.J., Segurado, J., LLorca, J., 2015. Three-dimensional dislocation dynamics analysis of size effects on void growth. Scr Mater 95, 11–14. doi:10.1016/j.scriptamat.2014.09.018.
Chang, Y.W., Asaro, R.J., 1981. An experimental study of shear localization in aluminum-copper single crystals. Acta Metall. 29, 241–257. doi:10.1016/0001-6160(81)90103-6.
Cordero, N.M., Forest, S., Busso, E.P., 2012. Generalised continuum modelling of grain size effects in polycrystals. Comptes Rendus Mécanique 340, 261–274.
Cordero, N.M., Gaubert, A., Forest, S., Busso, E.P., Gallerneau, F., Kruch, S., 2010. Size effects in generalised continuum crystal plasticity for two-phase laminates. J. Mech. Phys. Solids 58, 1963–1994. doi:10.1016/j.jmps.2010.06.012.
Ekh, M., Grymer, M., Runesson, K., Svedberg, T., 2007. Gradient crystal plasticity as part of the computational modelling of polycrystals. Int. J. Numer. Methods Eng. 72, 197–220. doi:10.1002/nme.2015.
Enakoutsa, K., Leblond, J., 2009. Numerical implementation and assessment of the GLPD micromorphic model of ductile rupture. Eur. J. Mech. A/solids 28, 445–460.
Eringen, A., 1999. Microcontinuum Field Theories. Springer, New York.
Ertürk, I., van Dommelen, J.A.W., Geers, M.G.D., 2009. Energetic dislocation interactions and thermodynamical aspects of strain gradient crystal plasticity theories. J. Mech. Phys. Solids 57, 1801–1814. doi:10.1016/j.jmps.2009.08.003.
Evers, L.P., Brekelmans, W.A.M., Geers, M.G.D., 2004. Non-local crystal plasticity model with intrinsic SSD and GND effects. J. Mech. Phys. Solids 52, 2379–2401. doi:10.1016/j.jmps.2004.03.007.
Fleck, N.A., Hutchinson, J.W., 1997. Strain gradient plasticity. Advances in applied mechanics 33, 296–361.
Flouriot, S., Forest, S., Cailletaud, G., Köster, A., Rémy, L., Burgardt, B., Gros, V., Mosset, S., Delautre, J., 2003. Strain localization at the crack tip in single crystal ct specimens under monotonous loading: 3d finite element analyses and application to nickel-base superalloys. Int. J. Fract. 124, 43–77. doi:10.1023/B:FRAC.0000009300.70477.ba.
Forest, S., 1998. Modeling slip, kink and shear banding in classical and generalized single crystal plasticity. Acta Mater. 46, 3265–3281. doi:10.1016/S1359-6454(98)00012-3.
Forest, S., 2009. Micromorphic approach for gradient elasticity, viscoplasticity, and damage. J. Eng. Mech. 135, 117–131. doi:10.1061/(ASCE)0733-9399(2009)135:3(117).
Forest, S., 2016. Nonlinear regularisation operators as derived from the micromorphic approach to gradient elasticity, viscoplasticity and damage. Proc. R. Soc. A 472, 20150755. doi:10.1098/rspa.2015.0755.
Forest, S., Barbe, F., Cailletaud, G., 2000. Cosserat modelling of size effects in the mechanical behaviour of polycrystals and multiphase materials. Int. J. Solids Struct. 37, 7105–7126.
Forest, S., Blazy, J.S., Chastel, Y., Moussy, F., 2005. Continuum modeling of strain localization phenomena in metallic foams. J. Mater. Sci. 40, 5903–5910. doi:10.1007/s10853-005-5041-6.
Forest, S., Cailletaud, G., 1995. Strain localization in single crystals: bifurcation analysis, effects of boundaries and interfaces. Eur. J. Mech. A Solids 14, 747–771.
Forest, S., Cailletaud, G., Sievert, R., 1997. A Cosserat theory for elastoviscoplastic single crystals at finite deformation. Arch. Mech 49, 705–736.
Franciosi, P., 1985. The concepts of latent hardening and strain hardening in metallic single crystals. Acta Metall. 33, 1601–1612. doi:10.1016/0001-6160(85)90154-3.
Geers, M., Peerlings, R., Peletier, M., Scardia, L., 2013. Asymptotic behaviour of a pile–up of infinite walls of edge dislocations. Archives of Rational Mechanics and Analysis 209, 495–539.
Germain, P., 1973. The method of virtual power in continuum mechanics. part 2: microstructure. SIAM J. Appl. Math. 25, 556–575. doi:10.1137/0125053.
Gurtin, M.E., 2000. On the plasticity of single crystals: free energy, microforces, plastic-strain gradients. J. Mech. Phys. Solids 48, 989–1036. doi:10.1016/S0022-5096(99)00059-9.
Gurtin, M.E., 2002. A gradient theory of single-crystal viscoplasticity that accounts for geometrically necessary dislocations. J. Mech. Phys. Solids 50, 5–32. doi:10.1016/S0022-5096(01)00104-1.
Gurtin, M.E., 2008. A finite-deformation, gradient theory of single-crystal plasticity with free energy dependent on densities of geometrically necessary dislocations. Int. J. Plast. 24, 702–725. doi:10.1016/j.ijplas.2007.07.014.
Gurtin, M.E., 2010. A finite-deformation, gradient theory of single-crystal plasticity with free energy dependent on the accumulation of geometrically necessary dislocations. Int. J. Plast. 26, 1073–1096. doi:10.1016/j.ijplas.2010.02.002.
Gurtin, M.E., Anand, L., Lele, S.P., 2007. Gradient single-crystal plasticity with free energy dependent on dislocation densities. J. Mech. Phys. Solids 55, 1853–1878. doi:10.1016/j.jmps.2007.02.006.
Han, X., Besson, J., Forest, S., Tanguy, B., Bugat, S., 2013. A yield function for single crystals containing voids. Int. J. Solids Struct. 50, 2115–2131.
Hure, J., Shawish, S.E., Cizelj, L., Tanguy, B., 2016. Intergranular stress distributions in polycrystalline aggregates of irradiated stainless steel. J. Nucl. Mater. 476, 231–242. doi:10.1016/j.jnucmat.2016.04.017.
Hussein, M.I., Borg, U., Niordson, C.F., Deshpande, V.S., 2008. Plasticity size effects in voided crystals. J. Mech. Phys. Solids 56, 114–131. doi:10.1016/j.jmps.2007.05.004.
Hütter, G., 2017a. Homogenization of a cauchy continuum towards a micromorphic continuum. J. Mech. Phys. Solids 99, 394–408. doi:10.1016/j.jmps.2016.09.010.
Hütter, G., 2017b. A micromechanical gradient extension of Gurson's model of ductile damage within the theory of microdilatational media. Int. J. Solids Struct. doi:10.1016/j.ijsolstr.2017.02.007. –
Koplik, J., Needleman, A., 1988. Void growth and coalescence in porous plastic solids. Int. J. Solids Struct. 24, 835–853. doi:10.1016/0020-7683(88)90051-0.
Kröner, E., 1969. Initial Studies of a Plasticity Theory Based upon Statistical Mechanics. In: Kanninen, M., Adler, W., Rosenfield, A., Jaffee, R. (Eds.), Inelastic Behaviour of Solids. McGraw-Hill, pp. 137–147.
Kubin, L., Devincre, B., Hoc, T., 2008. Modeling dislocation storage rates and mean free paths in face-centered cubic crystals. Acta Mater 56, 6040–6049. doi:10.1016/j.actamat.2008.08.012.
Kysar, J.W., Briant, C.L., 2002. Crack tip deformation fields in ductile single crystals. Acta Mater 50, 2367–2380. doi:10.1016/S1359-6454(02)00070-8. Computational Thermodynamics and Materials Design
Ling, C., 2017. Modeling the intragranular ductile fracture of irradiated steels. Effects of crystal anisotropy and strain gradient. PhD, January 24th 2017, Mines ParisTech.
Ling, C., Besson, J., Forest, S., Tanguy, B., Latourte, F., Bosso, E., 2016. An elastoviscoplastic model for porous single crystals at finite strains and its assessment based on unit cell simulations. Int. J. Plast. 84, 58–87. doi:10.1016/j.ijplas.2016.05.001.
Ling, C., Tanguy, B., Besson, J., Forest, S., Latourte, F., 2017. Void growth and coalescence in triaxial stress fields in irradiated FCC single crystals. J. Nucl. Mater. doi:10.1016/j.jnucmat.2017.04.013.
Little, E.A., 1986. Fracture mechanics evaluations of neutron irradiated type 321 austenitic steel. J. Nucl. Mater. 139, 261–276. doi:10.1016/0022-3115(86)90179-0.
Mandel, J., 1973. Equations constitutives et directeurs dans les milieux plastiques et viscoplastiques. Int. J. Solids Struct. 9, 725–740. doi:10.1016/0020-7683(73)90120-0.
Margolin, B., Sorokin, A., Shvetsova, V., Minkin, A., Potapova, V., Smirnov, V., 2016. The radiation swelling effect on fracture properties and fracture mechanisms of irradiated austenitic steels. part i. ductility and fracture toughness. J. Nucl. Mater. 480, 52–68. doi:10.1016/j.jnucmat.2016.07.051.
Mayeur, J., McDowell, D., Bammann, D., 2011. Dislocation–based micropolar single crystal plasticity: comparison of multi– and single criterion theories. J. Mech. Phys. Solids 59, 398–422.
Mayeur, J.R., McDowell, D.L., 2011. Bending of single crystal thin films modeled with micropolar crystal plasticity. Int. J. Eng. Sci. 49, 1357–1366.
Mayeur, J.R., McDowell, D.L., 2015. Micropolar crystal plasticity simulation of particle strengthening. Modell. Simul. Mater. Sci. Eng. 23, 065007.
Mesarovic, S., Baskaran, R., Panchenko, A., 2010. Thermodynamic coarsening of dislocation mechanics and the size-dependent continuum crystal plasticity. J. Mech. Phys. Solids 58, 311–329.
Miehe, C., 2014. Variational gradient plasticity at finite strains. part i: mixed potentials for the evolution and update problems of gradient-extended dissipative solids. Comput. Methods Appl. Mech. Eng. 268, 677–703. doi:10.1016/j.cma.2013.03.014.
Monnet, G., 2009. A crystalline plasticity law for austenitic stainless steel. EDF R&D internal report, PERFORM Project, H-B60-2008-04690-EN.
Niordson, C.F., 2008. Void growth to coalescence in a non-local material. Eur. J. Mech. A. Solids 27, 222–233. doi:10.1016/j.euromechsol.2007.07.001.
Niordson, C.F., Kysar, J.W., 2014. Computational strain gradient crystal plasticity. J. Mech. Phys. Solids 62, 31–47. doi:10.1016/j.jmps.2013.08.014. Sixtieth anniversary issue in honor of Professor Rodney Hill
Peerlings, R., Brekelmans, W., Borst, R.d., Vree, J.H.P.d., 1996. Gradient–enhanced damage for quasi–brittle materials. Int. J. for Numer. Methods Eng. 39, 3391–3403.
Peerlings, R., Poh, L., Geers, M., 2012. An implicit gradient plasticity-damage theory for predicting size effects in hardening and softening. Eng. Fract. Mech. 95, 2–12. doi:10.1016/j.engfracmech.2011.12.016.
Peirce, D., Asaro, R.J., Needleman, A., 1982a. An analysis of nonuniform and localized deformation in ductile single crystals. Acta Metall. 30, 1087–1119. doi:10.1016/0001-6160(82)90005-0.
Peirce, D., Asaro, R.J., Needleman, A., 1982b. An analysis of nonuniform and localized deformation in ductile single crystals. Acta Metall. 30, 1087–1119. doi:10.1016/0001-6160(82)90005-0.
Poh, L., 2013. Scale transition of a higher order plasticity model –a consistent homogenization theory from meso to macro. J. Mech. Phys. Solids 61, 2692–2710. doi:10.1016/j.jmps.2013.09.004.
Robach, J.S., Robertson, I.M., Wirth, B.D., Arsenlis, A., 2003. In-situ transmission electron microscopy observations and molecular dynamics simulations of dislocation-defect interactions in ion-irradiated copper. Philos. Mag. 83, 955–967. doi:10.1080/0141861031000065329.
Sabnis, P.A., Mazière, M., Forest, S., Arakere, N.K., Ebrahimi, F., 2012. Effect of secondary orientation on notch-tip plasticity in superalloy single crystals. Int. J. Plast. 28, 102–123. doi:10.1016/j.ijplas.2011.06.003.

Shu, J.Y., 1998. Scale-dependent deformation of porous single crystals. Int. J. Plast. 14, 1085–1107. doi:10.1016/S0749-6419(98)00048-5.
Simoto, S., H., J.W.F., Backofen, W.A., 1965. Ductile fracture in copper single crystals. Philos. Mag. 12, 319–333. doi:10.1080/14786436508218874.
Wulfinghoff, S., Bayerschen, E., Böhlke, T., 2013. A gradient plasticity grain boundary yield theory. Int. J. Plast. 51, 33–46.
Wulfinghoff, S., Böhlke, T., 2012. Equivalent plastic strain gradient enhancement of single crystal plasticity: theory and numerics. Proc. R. Soc. London A: Math., Phys. Eng. Sci. 468, 2682–2703. doi:10.1098/rspa.2012.0073.
Wulfinghoff, S., Böhlke, T., 2013. Equivalent plastic strain gradient crystal plasticity – enhanced power law subroutine. GAMM-Mitteilungen 36, 134–148. doi:10.1002/gamm.201310008.
Wulfinghoff, S., Forest, S., Böhlke, T., 2015. Strain gradient plasticity modeling of the cyclic behavior of laminate microstructures. J. Mech. Phys. Solids 79, 1–20. doi:10.1016/j.jmps.2015.02.008.
Zhao, K.J., Chen, C.Q., Shen, Y.P., Lu, T.J., 2009. Molecular dynamics study on the nano-void growth in face-centered cubic single crystal copper. Comput. Mater. Sci 46, 749–754. doi:10.1016/j.commatsci.2009.04.034. Proceedings of the 18th International Workshop on Computational Mechanics of Materials IWCMM-18
Z-set package, 2013. Non-linear material & structure analysis suite, www.zset-software.com.